ANALYSIS OF BRAIN IMAGES FOR DETECTION AND CLASSIFICATION OF DISORDERS USING DEEP LEARNING MODELS

Thesis submitted in fulfillment for the requirement of the Degree of

DOCTOR OF PHILOSOPHY

By

SUDHANSHU SAURABH

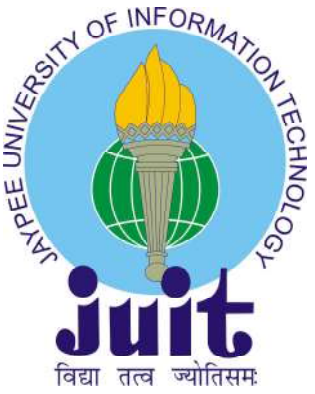

Department of Computer Science & Engineering and IT

JAYPEE UNIVERSITY OF INFORMATION TECHNOLOGY
Waknaghat, Solan-173234, Himachal Pradesh, INDIA

May, 2024

Table of contents

DECLARATION

I hereby declare that the work reported in the Ph.D. thesis entitled "**Analysis of Brain Images for Detection and Classification of Disorders Using Deep Learning Models** " submitted at "**Jaypee University of Information Technology, Waknaghat, Solan (H.P), India**", is an authentic record of my work carried out under the supervision of "**Dr. Pradeep Kumar Gupta**". I have not submitted this work elsewhere for any other degree or diploma. I am fully responsible for the contents of my Ph.D. thesis.

(Signature of the Scholar)

Sudhanshu Saurabh

Department of Computer Science & Engineering

Jaypee University of Information Technology, Waknaghat, Solan (H.P.),

India

Date:

SUPERVISOR'S CERTIFICATE

This is to certify the work reported in the Ph.D. thesis entitled "**Analysis of Brain Images for Detection and Classification of Disorders Using Deep Learning Models**" submitted by **Mr. Sudhanshu Saurabh**, Enrollment no. 186203 at **Jaypee University of Information Technology, Waknaghat, Solan (HP), India**, is a bonafide record of his original work carried out under my supervision. This work has not been submitted elsewhere for any other degree or diploma.

(Signature of Supervisor)

Dr. Pradeep Kumar Gupta

Professor

Department of Computer Science & Engineering

Jaypee University of Information Technology, Waknaghat, Solan (H.P.),

India

Date:

ACKNOWLEDGMENT

I would like to express my absolute reverence and gratitude to my supervisor, **Prof. Pradeep Kumar Gupta**, for his unconditional support and supervision and for providing his guidance throughout the proposed study. I will always be indebted to him for bearing my shortcomings with his immense sense of awareness, compassion, maturity, deep knowledge of the specific field, and consistency. I also would like to express my gratitude to the DPMC members, Dr. Ravindra Bhatt, Dr. Ekta Gandotra, and Dr. Rajiv Kumar, for their interactive assessments, questions, and opinions that provoked their thought. I also would like to thank all faculty and staff of the Department of Computer Science & Engineering, JUIT, Waknaghat, and Solan for their scholarly support and guidance. My aim of achieving merit in higher education at JUIT Waknaghat, Solan, would not have been completed without the unflinching support of my family and my dear ones. This milestone would not have been completed without the unwavering love, constant guidance, and support of my parents and the Almighty.

.

(Sudhanshu Saurabh)

Date:

ABSTRACT

Significant advances have been made in the field of deep learning and neuroimaging for the detection of neurological disorders and diseases. Non-invasive imaging modalities, such as functional magnetic resonance imaging ($fMRI$) and magnetic resonance imaging (MRI), make it easier to determine the composition and operations of the brain. Analytical evaluation of neuroimaging data can be beneficial not only in boosting the efficacy of diagnosing neuronal disorders but also in revealing the complexities of the brain when using deep learning techniques. This thesis aims to provide a theoretical and experimental foundation for the classification of brain disorders and brain activity of the datasets $fMRI$ and MRI, including deep learning models, deep learning visualization approaches, data encoding $fMRI$, and feature extraction.

In the first work, we developed a method that examines changes in $BOLD$ connectivity over time. fMRI is based on the signal $BOLD$, which measures neural activity indirectly. Before using functional connectivity metrics to evaluate the $BOLD$ signal, it is necessary to preprocess the fMRI data. A frequent periodic oscillation pulse generates various stimuli, and the $BOLD$ signal was produced by applying propagation loops. Functional connectivity highlights key aspects of cognitive development. In this work, we introduce a method that examines changes in the $BOLD$ signal. However, our method places more emphasis on spatiotemporal features, and coactivation events that occur consecutively

could cause a $BOLD$ signal. To characterize FC, our results demonstrate the metrics for evaluating functional connectivity FC using Pearson's correlation.

In the second work, we concentrate on MRI image intensities and implement clustering, which also shows the gradient information of the MRI image, which includes both contrast and intensity. The primary goal of edge detection is to differentiate tissues. The signal intensities at the edges of WM, GM, and CSF fluctuate significantly. The method used to determine intensity and edge detection tasks has been discussed here along with its effectiveness.

In this study, the $rs-fMRI$ data and FC of the 40 subjects are examined by the $BOLD$ signal in voxel size. The corresponding RSN are functionally applicable to these $BOLD$ signals. The data in $rs-fMRI$ time series from 40 subjects containing 176 time stamps and the active regions 28 of RSN have been visualized. To classify a neural disorder such as $ADHD$, we have proposed the Bidirectional $LSTM$ ($BLSTM$) model. To train $BLSTM$ with high-dimensional $fMRIdata$, we proposed a data reshaping algorithm. Subsequently, our modified $BLSTM$ was trained with the characteristic vector $(40 \times 261 \times 28)$ for each subject. Our findings show that the proposed model performs better than other state-of-the-art models by achieving a classification accuracy of 87.50%.

In this work, We focus on the 2D-CNN method for the classification of brain activity using task-based methods $fMRI$. This event-related $fMRI$ demonstrates how a particular task activates the neural response, which is based on the $BOLD$ signal. In $fMRI$ voxels, Our proposed 2D-CNN model uses $fMRI$ data to extract feature maps and successfully classify neural activity, which is based on task-evoked data $fMRI$.

A saliency map is a helpful method for interpreting and illustrating the non-linearity of the $2D-CNN$ model. We extended our work to analyze the behavior of the $2D-CNN$

model and visualize the saliency map of the MRI image, which is used to determine the product of components to eliminate noise. Using gradient-based visualizations and applying visual input, multiple-mode convolutional networks function. The $ReLU$ activation function is guided backward to produce the saliency map.

This work aims to develop a CNN-based model with a pre-trained $MobileNet$ model to detect and classify multiple sclerosis using the MRI image dataset. We have used magnetic resonance images to train the MobileNet-2D-CNN model for the identification of the Multiple Sclerosis (MS) feature map that predicts MS. We also created a class activation map to interpret the predictions provided by the proposed model, which represents the behavior of neurons in their early stages.

LIST OF ABBREVIATIONS

ABIDE	Autism Brain Imaging Data Exchange
AD	Alzheimer's disease
ADAM	Adaptive Moment Estimation
ADHD	Attention-deficit hyperactivity Disorder
AE	Autoencoder
ASD	Autism Spectrum Disorder
AUC	Area under the ROC Curve
B	Bias
BLSTM	Bidirectional Long- and Short-Term Memory
BOLD	Blood-Oxygen-Level-Dependent
CAM	Class Activation Map
CBF	Cerebral Blood Flow
CCA	Canonical Correlation Analysis
CNN	Convolutional Neural Network
CNV	Choroidal Neovascularization
CNV	Copy Number Variations (MLP-CNV)
CSF	Cerebrospinal Fluid

CT	Computed Tomography
DBN	Deep Belief Network
dMRI	Diffusion Magnetic Resonance Imaging
DNN	Deep Neural Network
DTI	Diffusion Tensor Imaging
DVars	Root Mean Square (RMS) of the Temporal Difference
EEG	Electroencephalogram.
EPI	Echo-Planar Imaging
EVI	Echo Volumar Imaging
FC	Functional Connectivity
FD	Framewise Displacement
fMRI	Functional Magnetic Resonance Imaging
FN	False Negative
FP	False Positive
FWHM	Full Width Half Maximum
GAN	Generative Adversarial Network
GAP	Global Average Pooling
GIG	Guided Integrated Gradient
GLM	General Linear Model
GM	Grey Matter
GPU	Graphics Processing Unit
GS	Global Signal
HCP	Human Connectome Project

HDMF	Hemodynamic Modulating Function
HOG	Histogram of Oriented Gradients
HRF	Hemodynamic Response Function
ICA	Independent Component Analysis
IG	Integrated Gradient
LSGAN	Least Squares Generative Adversarial Network
LSTM	Long and Short Term Memory
LTI	Linear Time Invariant
MCC	Matthews Correlation Coefficient
MI-EEG	Motor Imagery Electroencephalography
MLP	Multilayer Perceptron
MNI	Montreal Neurological Institute
MRI	Magnetic Resonance Imaging
MS	Multiple Sclerosis
MVPA	Multi Voxel Pattern Analysis
P	Prevalence
PARAFAC	Parallel Factor Analysis
PCA	Principal Component Analysis
PCC	Pearson Correlation Coefficient
PET	Positron Emission Tomography
RBM	Restricted Boltzmann Machine
ReLU	Rectified Linear Unit
RMSProp	Root Mean Squared Propagation

RNN	Recurrent Neural Network
ROI	Region of Interest
rs-fMRI	Resting-state Functional Magnetic Resonance Imaging
RSN	Resting State Network
SC	Structural Connectivity
SCA	Seed-based Correlation Analysis
SDVars	Standard Deviation of Response Error
TD	Tardive Dyskinesia
TE	Echo Time and Repetition Time
TN	True Negative
TP	True Positive
TR	Repetition Time
VGAN	Vanilla Generative Adversarial Network
VGG	Visual Geometry Group
WM	White Matter
XRAI	eXplanation with Ranked Area Integrals

LIST OF NOTATIONS

ϕ	Activation Function
$\overleftarrow{A}_t$	Backward state
$\psi(.)$	Basis Function
$Y(.)$	BOLD Signal
ψ	Brain Activity
$C_l^{<t>}$	Cell State
$v_i(t)$	Cognitive Stimulation
$Cov(X_{i,j})$	Covariance Matrix for i^{th} and j^{th} component of FC
D	Design Matrix
$\breve{C}_l^{<t>}$	Estimated current cell state
$g_{(i)}(s,t)$	Estimation of Hemodynamic response noise
$g(s,t)$	Estimation of Hemodynamic response
$F(w)$	Fisher's linear discriminant
$f_l^{<t>}$	Forget Gate
$(b_{\overrightarrow{A}}, b_{\overleftarrow{A}})$	Forward and Backward Bias condition in BLSTM
$\overrightarrow{A}_t$	Forward State
δ	Function between inter-stimulus-interval

$\Gamma(.)$	Gamma function of (HRF)
G	Generator Network
o	Hadamard Product
$a_i(t)$	Hemodynamic modulating function $(HDMF)$
$H(.)$	Hemodynamic response function (HRF)
$h^{<t>}$	Hidden State
$h_i(t)$	HRF at time t
θ_i	Stimulation level in the i^{th} voxel
$x^{<t>}$	Input feature vector
Δ	Inter-stimulus-interval
P	Joint distribution
$\prod$	Joint distribution product
$\sum$	Summation
Z	Latent space vector
LL	Logarithm of Likelihood
l	Layer
$\mathcal{L}$	Layer Component
$\mathcal{F}$	Layer Feature
f	Layer feature vector
$x_i(t)$ and $y_i(t)$	Mean Time Course
μ	Mean of voxel
$X(\tau)$	Mono Exponential Reduction
∇^2	Second order Laplacian operator

$r(x_i, x_j)$	Pearson correlation coefficient
I	Pixel intensity at position (x, y)
σ	Sigmoid function
T	Temporal basis function
$X(.)$	Time Series Signal
$s2$	Variance in voxel
$p_{i,j}$	Voxel at position (i, j)
σ^2	Noise in brain activity
w	Weight for neuron

LIST OF FIGURES

LIST OF TABLES

CHAPTER 1

INTRODUCTION

Neuroimaging is a discipline that facilitates information gathering in terms of human brain physiology, which involves evaluating functional and anatomical data using a variety of non-invasive methods. Some of these methods consist of: Functional Magnetic resonance imaging ($fMRI$),electroencephalography (EEG), positron emission tomography (PET). This could lead to more effective cooperation of medical treatments and early identification of brain diseases. The Advancements in the field of magnetic technology enabled the acquisition of higher-quality brain images. Ogawa et al. [1] found the idea that is currently extensively utilized for brain imaging, both physiologically and functionally. He improved upon (MRI) technique by generating brain images based on the variation in blood oxygenation levels which depends on blood flow towards neurons. The advancement of these kinds of technologies has also become feasible with the improvements in mathematical analysis through developing ever-more complicated neural networks that make it possible to extract functional and structural features of neuroimage. Using deep learning model for mental disorder and neurological diseases has growing significantly Greenspan et al. [2]. The most recent developments in deep learning methodologies illustrate the use of neuroimaging analysis for evaluations and detection of distinct region of the brain and

classify the certain disorders.

1.1 Motivation and Objective

Neuroimaging is an effective tool that is now being used to reveal important information about healthy and impaired human brains. Magnetic resonance imaging of the brain MRI and functional magnetic resonance imaging ($fMRI$) are non-invasive imaging modalities. Damadian et al. [3] obtained the first MRI image in 1976.However, the procedure received authorization for clinical use more than ten years later Fritsch et al. [4]. Among the various medical imaging techniques, MRI is one of the most efficient and suitable neuroimaging methods and is an effective tool for neuroimaging experiments that include the assessment of subjects with psychiatric disorders Castiglione et al. [5] Castiglione et al. [6]. The automatic detection and classification of various brain disorders has become a serious concern in modern healthcare. It may be difficult to diagnose certain mental disorders with neuroimaging alone. The methods used for data analysis are mainly based on the quantitative or statistical features extracted Pizzolante et al. [7]. In deep learning, the Convolutional Neural Network (CNN) aggregates spatial data, correlation between attributes, extraction, and identification of features using some machine learning algorithms, in addition to its exceptional ability to classify neuroimages. Through experimental studies, deep learning networks such as LiviaNet, IIyperDenseNet, and the convolutional neural network (CNN) Akkus et al. [8] Ding et al. [9] are widely used for the detection and classification of various neural syndromes.

1.1.1 Exploring Deep Learning Application in fMRI

The importance of exploring cognitive disorders in the area of neuroimaging, the advancement of deep learning techniques used to analyze fMRI data to identify and classify cognitive disorders, and challenges Jain and Huth [10]. A cognitive disorder that encompasses a wide range of diseases, including $ADHD$, multiple sclerosis, and associated abnormalities in the brain regions, using data from $fMRI$ the CNN model, was successfully classified Horikawa and Kamitani [11] Meszlényi et al. [12]. Spatial-temporal fluctuations in the brain region rs-fMRI are modeled using long-term memory based on the long-recurrent neural network (RNN) and short-term memory ($LSTM$) that have significant advances in sequential modeling Lipton [13] Dvornek et al. [14]. The correctness of the classification approach within this study is influenced by the extraction of typical time series. In a more recent investigation, a $3D-CNN$ was implemented to identify the implicit structure to incorporate an even larger cohort to decode task conditions featuring four-dimensional $fMRI$ (4D-fMRI) time series data taken from the Human Connectome Project compared to only one volume of fMRI, applied as input to the structure $3D-CNN$ Wang et al. [15]. Classify those who have $ADHD$ from healthy controls using a $multi-LSTM$ approach in the $ADHD-200$ data set Liu et al. [16]. In addition, there have been some recent developments in developing a state-of-the-art model $3D-CNN$ to study brain networks Wachinger et al. [17] Kawahara et al. [18]. The conditions under which we trained the Deep Neural Network (DNN) will be discussed in a further section.

1.1.2 Deep learning Model for brain disorder classification

Calculating FC measures using neuroimaging data $fMRI$ is a growing approach to the classification and prediction of neurological disorders. The findings of recent research Du

et al. [19] over three decades have focused on the classification of neurological disorders using FC measurement from fMRI data. According to these studies, $ADHD$, multiple sclerosis (MS), Alzheimer's disease (AD), mild cognitive disorder, schizophrenia, and bipolar disorder were the neurological disorders explored most frequently. Taking into account the kind of classifier, most studies used end-to-end deep learning techniques such as CNN. Kawahara et al. [18] presented one of the fundamentals of research on the applications of $CNNs$ to $fMRI$ data in 2017. The prediction of neurodevelopmental results was carried out using a deep learning framework.

1.1.3 LSTM Models for the Classification of ADHD

Recurrently combined memory cells along with three multiplicative input, output, and forget gates that keep the internal state ${C_l}^{<t>}$ and $h^{<t>}$ consistent make up the $LSTM$ layer Yu et al. [20]. The forget gate selects the relevant data from the preceding state. The following equations represent the elements $LSTM$ used in the calculation:

$$f_l^{<t>} = \sigma(W_l[h^{<t-1>}, x^{<t>}] + \phi_l) \tag{1.1}$$

$$i_l^{<t>} = \sigma(W_u[h^{<t-1>}, x^{<t>}] + \phi_u) \tag{1.2}$$

$$\breve{C}_l{}^{<t>} = \tanh(W_c[h^{<t-1>}, x^{<t>}] + \phi_c) \tag{1.3}$$

$${C_l}^{<t>} = {f_l}^{<t>} o {C_l}^{<t-1>} + {t_l}^{<t>} o {C_l}^{<t>} \tag{1.4}$$

$$f_o^{<t>} = \sigma(W_o[h^{<t-1>}, x^{<t>}] + \phi_o) \tag{1.5}$$

$$h^{<t>} = f_o^{<t>} o \tanh {C_l}^{<t>} \tag{1.6}$$

Where, $f_l^{<t>}$, $i_l^{<t>}$, $\breve{C}_l{}^{<t>}$, ${C_l}^{<t>}$, $h^{<t>}$, and $x^{<t>}$ represent the forget gate, input gate,

estimated current cell state, cell state, hidden state, and input feature vector, respectively. The parameters for the weights are W_l, W_u, W_c, and W_o. For every layer (l) at the moment (t), the bias vectors include ϕ_l, ϕ_u, ϕ_c, and ϕ_o, while the sigmoid function is $\sigma = \frac{1}{1+e^{-x}}$ and o represent the Hadamard product. Two distinct models $LSTM$ were applied to classify ADHD according to the following:

(I) **Stacked LSTM:** is a specific kind of recurrent neural network that includes an arrangement of recurring memory cells, since all memory cells are connected to the last cell. It takes in the input and then keeps each block's state unchanged. The $LSTM$ sequence is composed of a stack of multiple $LSTM$ layers. We applied three $LSTM$ layers, as shown in Figure. 1.1. In this setup $LSTM$, every layer cell receives input at different times. It combines the data from the stacking $LSTM$ and produces the result on various time stamps.

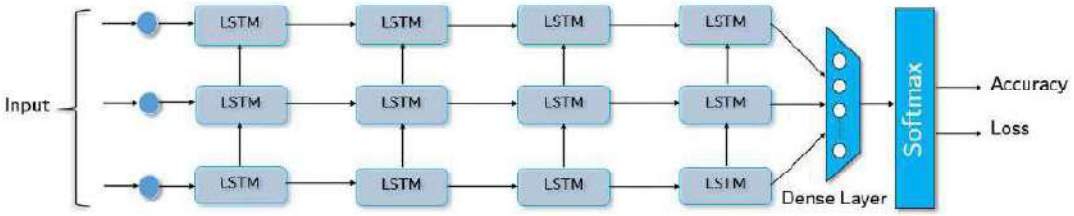

Figure 1.1: The stacked LSTM schematic block diagram

(II) **Bidirectional LSTM:** Two $LSTMs$ are used in the $BLSTM$ network according to Graves and Schmidhuber [21] both the $LSTM$ work in forward and backward directions and give the combined outcome in the following manner:

$$Forward\ LSTM : \overrightarrow{A_t} = \phi\Big(w_{x\overrightarrow{A}}X_t + w_{\overrightarrow{A}\overrightarrow{A}\overrightarrow{A_{t-1}}} + b_{\overrightarrow{A}}\Big)$$

$$Backward\ LSTM : \overleftarrow{A_t} = \phi\Big(w_{x\overleftarrow{A}}X_t + w_{\overleftarrow{A}\overleftarrow{A}\overleftarrow{A_{t-1}}} + b_{\overleftarrow{A}}\Big)$$

$$Combined\ Output : Y_t = \phi\Big[w_Y(\overrightarrow{A_t}, \overleftarrow{A_t}) + b_Y\Big]$$

Where, w_Y represents the weight of the recurrent neuron, b_Y signifies bias, $(\overrightarrow{A_t}, \overleftarrow{A_t})$ stands for forward and backward states, and activation at time t. In addition, $(b_{\overrightarrow{A}}, b_{\overleftarrow{A}})$ refers to the bias conditions for the two $LSTM$ layers.

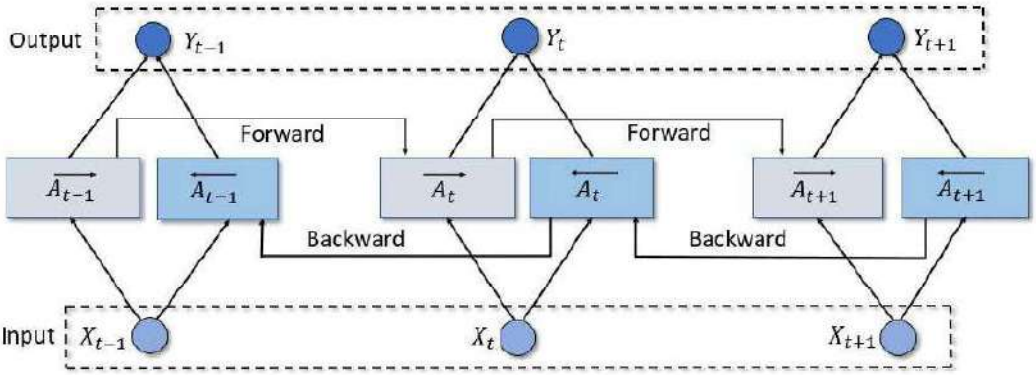

Figure 1.2: Bidirectional long short-term memory ($BLSTM$) architecture

Figure 1.2 represents a schematic framework of $BLSTM$, where each time period, i.e. $t-1, t$ and $t+1$, are specified the series of inputs are X_{t-1}, X_t, X_{t+1}, after processing $LSTM$ layers generates the output parameters are Y_{t-1}, Y_t, Y_{t+1} subsequently with the activation function ϕ showing the hidden states of both directions, that is, $\overrightarrow{A_t}$ and $\overleftarrow{A_t}$.

1.2 Brain Imaging and Magnetic Resonance Imaging

In the past 20 years, MRI have been used to identify neurological diseases such as MS, malignant tumors, or Alzheimer's disease, and neurological disorders such as Attention Deficit Hyperactivity Disorder ($ADHD$), as well as psychiatric disorders Vieira et al. [22] Brant-Zawadzki et al. [23]. $ADHD$ is a neurological disorder that is a prevalent neurodevelopmental condition. A higher degree of emotional liability/negativity has been associated with $ADHD$ symptoms. The complicated structure of the human nervous system, which contains neurons Olaf [24]. MRI is non-intrusive and is capable of providing useful information. Different magnetic resonance MRI modalities generate numerous contrasted images. The two fundamental forms of MRI imaging, that is, $T1$ and $T2$-weighted brain imaging. $T1$ weighted MRI images can be generated with shorter times of echo time (TE) and repetition time (TR). In the MRI image, which consists of brightness and contrast that is determined primarily by the properties of $T1$ tissue. $T2$ weighted imaging is produced using longer TE and TR durations. The intensities of the images are frequently controlled by the properties $T2$ of the tissue Boaventura et al. [25] Glasser et al. [26].

MRI imaging technology advances, specifically $fMRI$ and Diffusion Magnetic Resonance Imaging ($dMRI$), make it a possible noninvasive, in vivo observation of the human brain network (sometimes called a connectome) and have a comparatively significant sensitivity and resolution Bandettini and Bullmore [27]. $fMRI$ has progressively grown to be a more significant tool to examine how the brain processes information neurologically. fMRI is a useful technique for studying the human brain, as it is noninvasive. A sequence of three-dimensional brain scans is used in $fMRI$ experiments to observe the neural

activity of participants Wang and Guo [28]. Numerous studies on neuroimaging have documented the occurrence of spontaneous activation of the brain while at rest Biswal et al. [29] Arieli et al. [30] Leopold and Maier [31].

Additionally, it provides excellent integration of both temporal and spatial resolutions. To describe the hemodynamic response, $fMRI$ uses temporal resolution. Since the development of anatomical maps and atlases, the area of neuroimaging has advanced significantly toward data-driven feature learning techniques. A few methods are, for example, independent component analysis (ICA), seed-based correlation analysis (SCA), canonical correlation analysis (CCA), and some features that differentiate both controls and subjects. Based on the connectivity that exists in the resting state functional magnetic resonance imaging data ($rs - fMRI$) using parcellation, which is determined by the data and anatomic assumptions, however, it constantly becomes challenging to distinguish slight variations in cognitive states for certain insights $fMRI$ due to different temporal lengths. Shen et al. [32] Perform an experiment on real $fMRI$ data and analyze the demarcation between $rs - fMRI$ and task-based $fMRI$ data; retrieve a pair of ROI such as visual cortex and intraparietal sulcus.

The feature selection is performed using Deep Learning (DL) models by integrating simple data with increasingly complex and functional composite representations. Deep-learning models can boost their computational capability to find prediction functions that have the best efficiency. Initial studies on neural imaging using Deep Learning models were published in 2014 Plis et al. [33], and the amount of research carried out has grown substantially since then.

- We make an effort to demonstrate the significant benefits of an efficient deep learning framework for neuroimaging.

- The deep learning model in the context of fMRI data outperforms shallow machine learning classifiers Yang et al. [34].
- Develop an effective and novel LSTM model for time series-based neuroimage analysis to identify neurological disorders by analyzing various brain signals,
- Application of Transfer learning algorithms to efficiently learn and interpret specific regional brain activation.
- Neurological Diseases: Detection and Classification Using a Deep Learning Framework

1.2.1 Echo Planar Imaging

It is necessary to consider the significant variations in each individual's brain while analyzing fMRI data. As a result, several researchers sought a variety of explanations concerning the multisubject evaluations. The most popular technique is the spatial transformation of the neuroimage into the standard coordinate space Friston et al. [35]. When applied to the subject of human brain imaging examination, brain format images MNI are still probably the most widely used and are used by a number of fMRI analysis software, such as statistical parametric mapping (SPM) https://www.fil.ion.ucl.ac.uk/spm/. Echo planar imaging (EPI) is the technique most frequently used in clinical brain imaging Mansfield [36]. It is a method for real-time MRI imaging, a single image using a video rate, for use in medical and clinical investigations, such as detecting cerebral blood flow. The echo technique EPI is often used for most $fMRI$ procedures. It can acquire data related to a two-dimensional image in approximately sixty milliseconds at appropriate resolutions of voxel size, as shown in Figure 1.3. It is necessary to identify the source of the energy

release. Magnetic field gradients can be applied across three orthogonal orientations. The most common usage of EPI is as a sequence of $2D$, and additionally, $3D-EPI$ has been created (echo volume (EVI)) Mansfield et al. [37]. The pulse pattern EPI combines the temporal (m) and spatial (n) configurations of the gradient with more image slices.

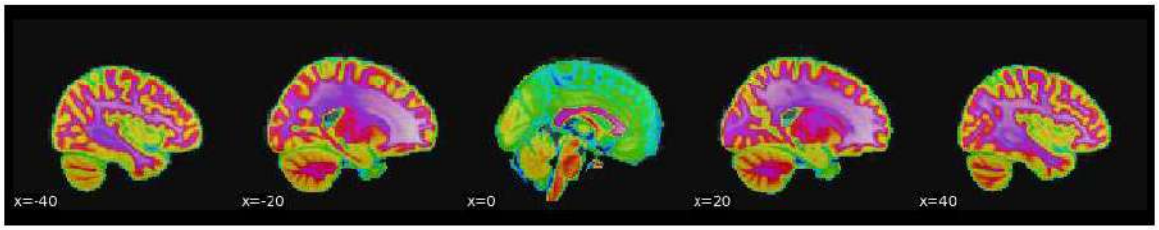

Figure 1.3: The MNI coordinates indicate the location where the slicing is performed, slices from an EPI image

1.2.2 Structural Brain Mapping and Parcellation

Early research has shown a complex relationship between structural and functional connection patterns Greicius et al. [38] Hagmann et al. [39] Vincent et al. [40]. Structural connectivity (SC) represents the spatial connection across the entire brain. It is among the most widely recognized and effective neuroscience studies that have included distinguishing features and representations of spatially different subregions of the cerebral cortex Zilles et al. [41]. An essential characteristic of the clusters of neurons that make up the neurons of the cerebral cortex that associate with each other based on similar microstructural characteristics that generate coherent regions Toga et al. [42] Knösche and Tittgemeyer [43].

The most significant marker has grown into the anatomical microstructure. It is used to determine the cortical environment of humans Amunts et al. [45] Geyer et al. [46] Tootell and Nasr [47] Amunts and Zilles [48]. The remarkable cytoarchitectonics-based parcellation of the cerebral cortex, the distinction of the cortical region, is based

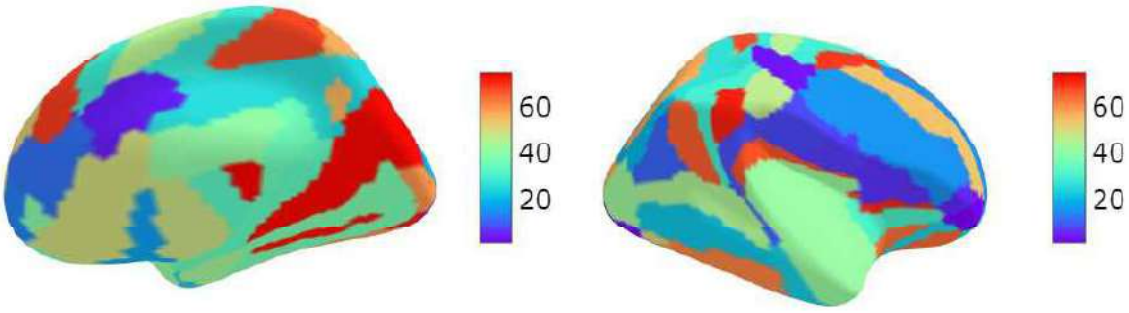

(a) (b)

Figure 1.4: Segmentation of a brain into smaller part is a parcel: Sulcogyral parcellation (a) left hemisphere and (b) right hemisphere is observed by Destrieux et al. [44]

on variations in cellular lamination patterns and, furthermore, due to more prevalent macroscopic characteristics, including connection patterns Guillery [49]Amunts and Zilles [48] Passingham et al. [50] Eickhoff et al. [51]. The dimension of the regions is one of the most significant determinants in the examination of brain connections. In a parcellation that authentically describes the cortical regions of the brain, each parcel must appear homogeneous. It must have a consistent functional connection pattern throughout the parcel Craddock et al. [52] Shen et al. [53]. According to Power JD and SE. [54] Yeo et al. [55] a substantial network structure is necessary for a parcellation to adequately demonstrate cortical regions. Using the multigraph clustering algorithm, a whole brain parcellation was produced Shen et al. [56].

Parcels that appropriately represent cortical regions in the group average data must be utilized to generate sufficient a priori ROIs for each subject. The basic principle of neuroscience is the parcellation of the outer layer of the human brain, which is gray matter (GM) and millions of densely packed axons white matter (WM) into functional units Arslan and Rueckert [57] Destrieux et al. [44], as demonstrated in Figure 1.4. In association with high-resolution parcellation methods that separate the brain into voxels. We present

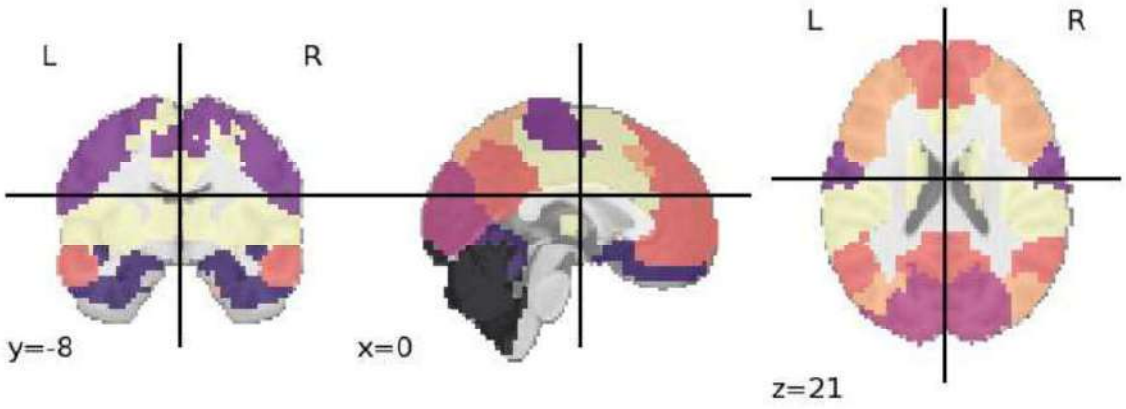

Figure 1.5: The bootstrap analysis of stable clusters (BASC) (Bellec et al., 2010) technique was used to create the brain parcellations, and a data-driven approach was used to choose the scales.

a data-driven method for whole-brain parcellation. Structure-based parcellation, such as cytoarchitecture and tractography, provides standardized atlases that have been widely used for several experiments. Although brain anatomy and function are intrinsically linked, it is envisaged that the anatomically defined brain atlas might be used to construct functional connectivity networks of the brain. The aggregated voxels describe the fundamental concept of connectivity-based parcellation with homogeneous connectivity patterns within the clusters, which is depicted in Figure 1.5. Thus, particular clustering processes often serve as the basis of brain parcellations, which we use in brain imaging.

1.2.3 Resting State fMRI (rs-fMRI)

Stimulus or task-based fMRI frameworks have been essential to our understanding of how the brain works at any given moment. $rs-fMRI$ is a technique to analyze intrinsic brain networks while the brain functions at rest (when subjects are at rest). It represents activations during the state of the task to measure the correlation between different areas of the brain Biswal et al. [29] Lin et al. [58] Esteban et al. [59]. Task-based $fMRI$

sometimes cannot or does not pick the same patterns throughout the brain, while $rs - fMRI$ is achieved. Neuronal activity evaluation is performed while a task demonstrates a combination of spontaneous and task-evoked activity. The rs-fMRI technique continues to advance, improving our understanding of the manner in which the brain develops with age and with the brain develops with age and with disease Lin et al. [58] di Qin et al. [60]. The primary goal of $rs - fMRI$ is to measure spontaneous activity in oxygen-level-dependent signals in blood ($BOLD$) Biswal et al. [29].

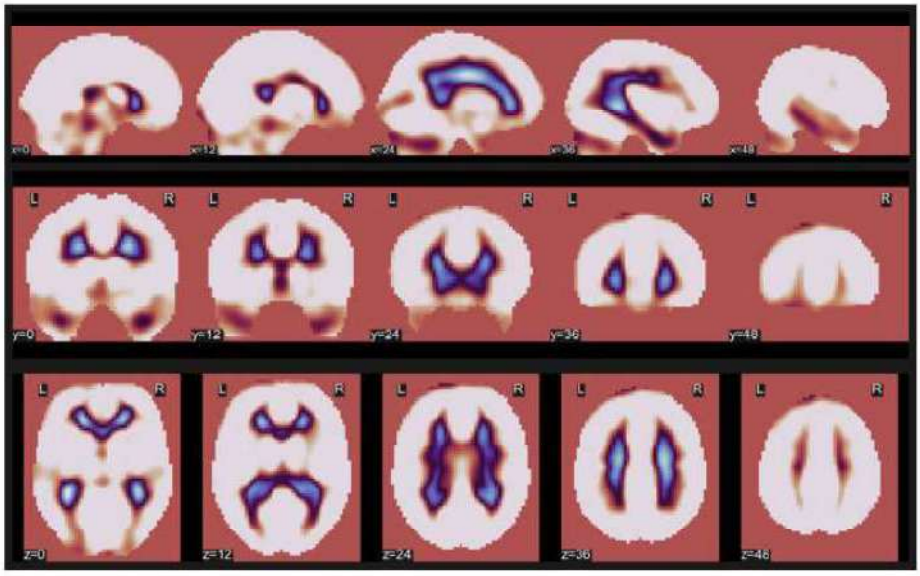

Figure 1.6: Spatial mapping of the specified RSNs.Spatial normalization of the data has been performed in the standard MNI space. Coordinates their peak activations.

There are extremely few amplitude variations within these $rs - fMRI$ signals, especially at low rest frequencies between 0.01 and $0.1Hz$. In this study, we present an analysis of $rs - fMRI$ studies and give examples of possible medical applications found in the literature. $rs - fMRI$ is examined for synchronized activation that occurs when no task or stimulus is present between spatially distinct brain regions to identify resting state networks ($RSNs$). The default mode network (DMN) is potentially and most significantly fundamental RSN. RSN essentially refers to this spatial correlation between

more than two areas of the brain. In this study, we used $rs-fMRI$ data from two different types of subjects, such as those suffering from attention deficit hyperactivity disorder ($ADHD$) and healthy controls, to further the research. According to a trend, ADHD predictions were becoming worse when training models with matrices that did not include the default mode network Rosenberg et al. [61]. Previous studies have focused on the correlation between the functional network according to the similarities that exist between their BOLD time course and the use of correlation functions such as Pearson's correlation. In such instances, an array of selected voxels is used when examining the data $rs-fMRI$.

1.3 Resting State Network (RSN)

Some regions in the brain demonstrate correlated activity between the motor cortex and other portions of the brain area associated with brain activity, and this correlated activity has been finally identified as contained in several brain systems Biswal et al. [29] Seitzman et al. [62] Vieira et al. [63].

- **Functional Network:** That correlated activity, known as functional systems and distinctive connectivity networks, is called a resting state network (RSN). Several characteristics of RSN such as motor, sensory systems, cognitive control, frontoparietal, basal ganglia, memory, and default mode network (DMN) are extracted and have been linked to the cause of the disorder of $ADHD$, according to various approaches Zhou et al. [64] Damoiseaux et al. [65] De La Fuente et al. [66]. According to Pruim et al. [67] Choi et al. [68] dos Santos Siqueira et al. [69] were specifically developed to analyze the modifications RSN in $ADHD$. $RSNs$ are distinguished

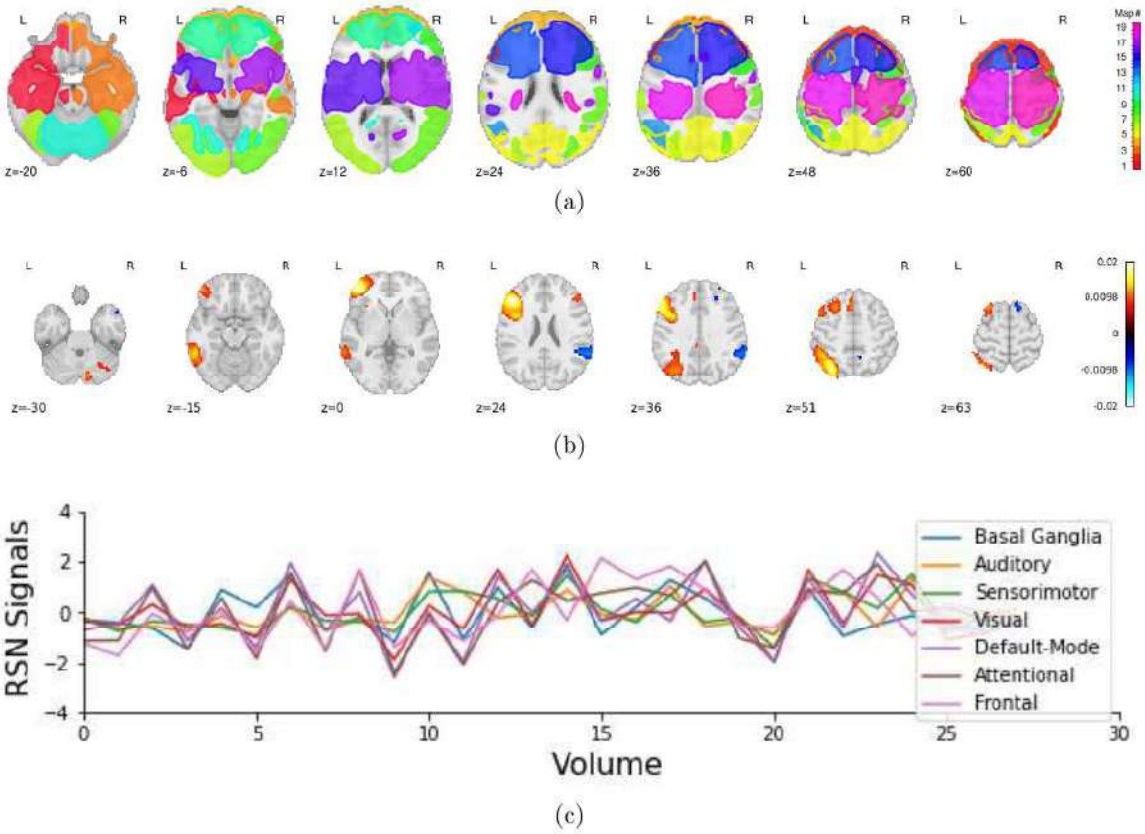

Figure 1.7: Visualization of RSN,ICA and RSN time-series (a) Visualization of the extracted region of Functional networks in RSN (b) Independent components in various types of spatial maps representing $RSNs$ (c) The time series that ICA extracted from specific $RSNs$.

by standard correlations using the BOLD stimulus in specific areas of the brain. The topography of RSNs is almost identical to the responses extracted for various cognitive, sensory, and motor functions, as represented in Figure. 1.7(a). RSN can be accurately determined by the fluctuation observed in the BOLD signals of the resting brain in subjects Seitzman et al. [62] Zhou et al. [64], fluctuations occur at very low frequencies (< 0.1 Hz).

- **RSN Timeseries:** Time series features must be explored for RSN, for several time series signals that originate in various regions of the brain Figure 1.7(c). The intensity (amplitude) associated with RSN was represented by the RSN time series.

To study various regions of the brain, the levels of time series signals coming from various ROIs of the brain were converted to ROI signals using dimension reduction methods. The rs-fMRI depends on spontaneous low-frequency fluctuations that occur in the $BOLD$ response. The spatial and instantaneous characteristics of the BOLD responses have been associated with respect to the corresponding configuration of WM and gray matter GM within a particular voxel Provencher et al. [70].

- **RSN-ICA:** RSN are anatomically distinct but functionally connected regions that demonstrate substantial correlations in $BOLD$ signal activity. An efficient signal analysis technique called independent component analysis (ICA) has been used and can be seen in Figure. 1.7(b) to determine and examine accurate functional connectivity patterns (FC) of signal fluctuations $BOLD$ in $rs-fMRI$ Beckmann et al. [71]. Attempts to provide the correlation that exists between spatial ROI by using linear spatio-temporal correlation. The term "spatiotemporal interdependence" refers to the functional connectivity of the region of the brain among various widely distributed neurophysiological events Oliveri et al. [72].

1.4 The Event Specific fMRI

$fMRI$ has been used by most studies in recent years to find out more about brain cognitive autonomy along with connectivity of multiple brain regions Thibault et al. [73] Yu et al. [74]. The activity level of the cerebral cortex can be observed instantaneously using $fMRI$ by fluctuating the $BOLD$ signal that is triggered by neuronal activity in the cerebral cortex, additionally acquiring information and evaluating the $BOLD$ signals

Cox et al. [75] Logothetis [76]. $fMRI$ provides superior spatial resolution with less interference. This means that the identification of neurological activity has become more important using the data from $fMRI$.

1.4.1 BOLD Response

$BOLD$ imaging is a technique used in $fMRI$ studies to generate images Ogawa et al. [1]. It is interpreted as a substitute indicator of the spontaneous hemodynamic response to neural activity. An implicit measure of neural activity is provided by the impulse response function or the hemodynamic response function (HRF) which is characterized by the $BOLD$ signal that appears in $fMRI$ during rest Friston et al. [77]. It is typically recognized as the nonlinear nature of neural activity. The activity of neural tissue allows for an increase in voxel size and leads to the regulation of affected cerebral blood flow (CBF) which results in the hemodynamic response.

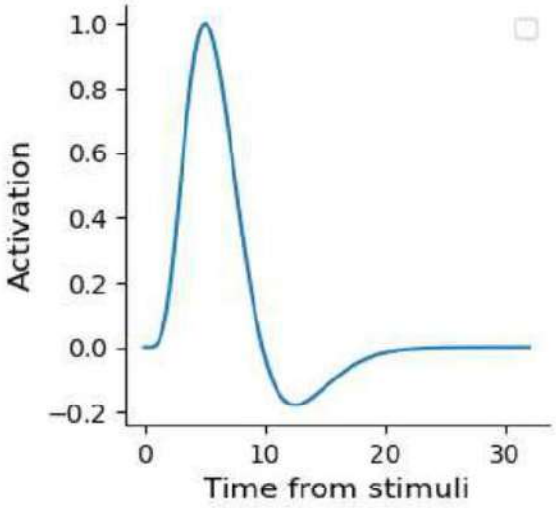

Figure 1.8: The Canonical Hemodynamic Response Function, which displays the fMRI signal's temporal evolution shortly after an initial activation activity. The expected response of neurons during particular stimuli.

One of the most standard approaches is to model the HRF determined by the balloon

model Friston et al. [77] Buxton et al. [78] Buxton et al. [79]. During the evaluation of the $BOLD$ signal, there are three attributes that are frequently used to describe the appearance of the BOLD signal: (i) Full Width at Half Maximum ($FWHM$). (ii) Peak Height and (iii) Time of Peak. Fluctuations in the firing rate are responsible for the fluctuation of its maximum height, peak time, onset delays, and duration of neuronal activity. To determine the more accurate neuronal events that may be used for the HRF measure.

Consequently, as neural activity increases, this results in higher MRI intensity. The convolution is used to depict the response $BOLD$ during the stimuli $S(\cdot)$, as well as the hemodynamic response function. $H(\cdot)$ therefore, the $BOLD$ signal is represented as:

$$Y(t) = H \otimes X(t) = \int H(t-v)X(v)dv \tag{1.7}$$

The function HRF $H(t) = 0$ for $t < 0$ is considered to be of short duration. The focus of this work was on the homogenization of the data-driven fMRI dataset WM and the cerebrospinal fluid signals (CSF). The purpose of the research is to determine a correlation between the FC measure, which is calculated using the $BOLD$ signals.

1.4.2 fMRI Voxel Analysis

The $BOLD$ signal has been determined using a $fMRI$ scanner. The $BOLD$ signal corresponding to each voxel is exactly specified by the fMRI calculation Stanley et al. [80]. $fMRI$ images are $3D$ brain regions measured over time and are generally multidimensional. The data consist of a series of $MRIs$, each with a number of equally distributed volume components, or voxels, that separate the brain into equal-sized cells. The voxel-

specific image intensity demonstrates the spatial distribution with respect to the nuclear spin density of a specific region. A standard fMRI data collection consists of a time series of several thousand voxels. To identify the activation model during a particular task, a general linear model (GLM) has been extensively used as a modelFriston et al. [77]. The objective of $fMRI$ statistical data analysis is to determine the appropriate level at every voxel level. For $rs - fMRI$ It includes two distinct categories of analytical approaches (i) Functional Integration, which evaluates functional connectivity between different regions of the brain; and (ii) Functional Segregation, which estimates local activity in any particular voxel time series. In a significant number of previous studies, at the regional level, FC maps have been generated Salvador et al. [81] Achard et al. [82]Supekar et al. [83] Supekar et al. [84]. The combination of fMRI time series with the respective voxels is required for region-level connectivity.

1.4.3 Functional Connectivity

Functional Connectivity (FC) is described by comparing similarities and distinctions in various brain signals that occur in two regions. Numerous FC analyses based on $fMRI$ signals demonstrate the number of pathological factors that influence the brain FC Hull et al. [85] Hua et al. [86]. The signals are generated by two different anatomical regions $\{i\}$ and $\{j\}$ of the human brain; this could appear to be correlated. This would signify that these regions are functionally connected in the brain Damoiseaux et al. [65] Greicius et al. [87] Shirer et al. [88] Salvador et al. [81]. While there are several methods to calculate functional connectivity, for linear correlation, a typical Pearson correlation coefficient approach (PCC) is used to analyze FC. Functional connectivity was evaluated between the two sets of temporal data between the regions by calculating PCC. The mean time

course for every subject can be represented as $\{x_i(t)\}$ and the Pearson correlation is defined as:

$$r(x_i, x_j) = \frac{\sum_{i=1}^{n}[x_i(t) - \bar{x_i}][y_i(t) - \bar{y_i}]}{\sqrt{\sum_{i=1}^{n}[x_i(t) - \bar{x_i}]^2}\sqrt{\sum_{i=1}^{n}[y_i(t) - \bar{y_i}]^2}}$$

in which $\bar{x_i}$ is the average of x_i. It has to be expressed that a significant correlation exists between the two regions that cannot ensure a functional connection between the base neurons. For example, there could be an appropriate correlation between brain activity from two different regions. The partial correlation is represented as:

$$r(x_i, x_j) = \frac{\mathrm{Cov}(X_{i,j})^{-1}}{\sqrt{\mathrm{Cov}(X_{i,i})^{-1}\mathrm{Cov}(X_{j,j})^{-1}}}$$

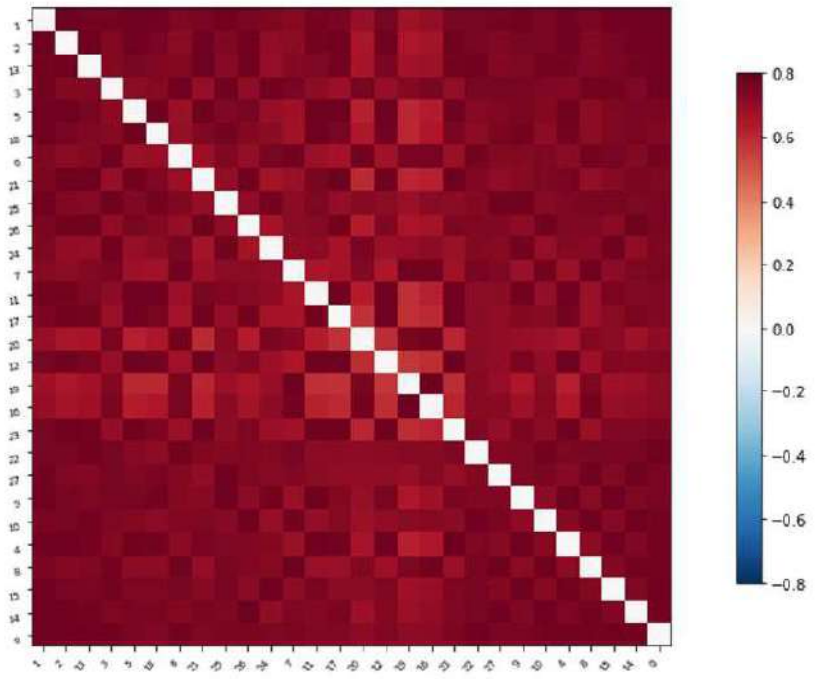

Figure 1.9: Correlation matrix depicts the connectivity measure of various regions of the ADHD 200 $fMRI$ dataset used for the classification.

Where $Cov(X_{i,j})$ describes the $\{i^{th}\}$ and $\{j^{th}\}$ a component of the inverse covariance matrix obtained from matrix $\mathbf{X}$. FC the resting state demonstrates replicable brain net-

works, which are likely to be significant in our understanding of brain behavior-associated factors in disorders such as $ADHD$ Castellanos and Proal [89]. Various connectivity states indicate different networks between correlated regions. Clustering has been used by researchers Allen et al. [90] Du et al. [91]. For the analysis of functional connectivity, the analysis of principal components (PCA) is applied for the reduction of dimensions between distinct brain regions Leonardi et al. [92]. For the extraction and identification of functional connectivity conditions, Fisher's discrimination analysis technique and Independent Component Analysis (ICA) have been applied by Li et al. [93] Miller et al. [94]. As a result, modifications to correlated regions give distinct measures of disorders.

1.5 Objectives

The fundamental objective of deep learning in MRI classification has been categorized into two distinct goals. Initially, there has been scientific significance, such as (i) Whenever an algorithm using deep learning can accurately classify MRI data due to a specific neurological disorder or mental disease, the analysis of this deep learning framework will offer a higher-quality interpretation of neurological disorders. (ii) Prospective applications in healthcare care are another reason for consideration.The purpose of the study carried out for this thesis consists of the following:

- To interpret the connection between neural activities using $BOLD$ signal-based correlation and gradient comparison in an MRI image
- To design a deep learning model for the classification of brain disorders with as much accuracy as is feasible using $fMRI$ data

- To detect, visualize, and classify the neural activity in response to a given task by CNN model for the stimuli in the identified voxel

1.6 Dataset description

There are two fundamental types of neuroimaging technologies: (i) Functional brain imaging and (ii) Structural brain imaging. Functional brain imaging are used to determine metabolism, blood flow and activity of the brain. The results of these procedures are frequently combined with structural imaging. Among the methods for functional brain imaging include $(fMRI)$, magnetoencephalography (MEG).The two most popular brain imaging methods are $fMRI$ and MRI, $fMRI$ is performed on MRI. systems. The prospective application of $fMRI$ is to determine which brain regions are involved in sensory function, motor function and language. The purpose of fMRI is to investigate how the brain functions by examining the temporal fluctuations of each region's activity. For this thesis, the publicly available $fMRI$ data obtained from the $OpenfMRI$ database https://openfmri.org/dataset/ds000228/, accession number $ds000228$, provides behavioral and fMRI data. There are 155 participants in the fMRI data, of which 71 are male and 84 are female comprising 33 adults followed by 122 children. Collected 4D-fMRI images represent large-scale, high-dimensional data sized at $(50 \times 59 \times 50 \times 168)$ including 50 slices. We have also taken into account the different statistical factors that are displayed in Table. 1.1. For classification of brain activity as well as behavioral activity, each voxel size is 3 mm isotropic and $TR = 2$ second.The confounds consist of merely six motion metrics, which include a mean framewise displacement (FD), a signal from (WM), a (CSF), and six anatomical parameters shown in Table. 1.2. In this study, we

Table 1.1: Summary of the age-related statistical measures employed in the research

Age Group	Age Count	Mean	Std.Dev.	Min. Age	25%	50%	75%	Max. Age
3yo	17	3.75	0.17	3.51	3.60	3.78	3.93	3.98
4yo	14	4.43	0.28	4.05	4.17	4.36	4.71	4.85
5yo	34	5.50	0.28	5.01	5.31	5.46	5.73	5.99
7yo	23	7.53	0.36	7	7.14	7.66	7.91	7.96
8-12yo	34	9.76	1.18	8.02	8.63	9.69	10.53	12.3
Adults	33	24.77	5.30	18	21	23	28	39

used the mean of the WM and CSF time-series signals to classify the neural activity.

1.7 Challenges and Contributions

The main challenge is applying deep learning methods to neuroimaging data that describe brain disorders and fluctuations in brain activity that exist under various conditions for experiments. It is challenging to detect brain activity in $fMRI$ data, which provides an arbitrary and noisy method of measuring. It does not analyze cortical regions but instead records the standard impacts of numerous spikes. To detect and classify neurodevelopmental disorders and neural activity, the deep neural network generated attention to make the decision-making method more comprehensible and interpretable. The following are the most significant issues affecting the performance of the network:

- Determining the correlation with high-dimensional brain activity is one of the most important problems in neuroimaging, which challenges establishing the validity and accuracy of DL model outcomes.

- When employing various Deep Neural Network (DNN) architectures, such as CNN and RNN, to execute deep learning, the basic challenge has proven challenging

Table 1.2: The first 30 Participants confounds consist of five motion metrics

Age	Age Group	Gender	CSF	WM	Global Signal	Std Dvars	Dvars
3.51	3	M	850.07	932.23	1082.9	1.3943	42.98
3.98	3	F	1016.04	1118.12	1496.04	1.3006	33.4
3.78	3	F	872.34	922.67	1219.86	1.3868	48.61
3.84	3	M	1024.23	1152.33	1335.54	1.2398	22.11
3.63	3	M	791.72	815.73	1148.06	1.1774	25.54
3.62	3	M	745.34	847.24	1129.01	1.4488	44.29
3.93	3	F	751.44	765.85	971.47	1.3609	41.95
3.93	3	F	768.21	733.65	943.5	1.3019	33.96
3.98	3	F	798.59	829.09	1003.06	1.5954	63.28
3.53	3	M	701.67	789.12	971.63	1.5854	85.13
4.77	4	M	805.11	863.3	1242.84	1.4783	41.7
4.35	4	M	903.62	1018.56	1222.31	1.4259	28.61
4.76	4	F	775.03	833.83	1055.75	1.3481	36.71
4.05	4	M	857.92	863.61	1118.08	1.3112	31
4.08	4	F	773.94	754.47	1016.96	1.3711	44.98
5.99	5	M	552.13	537.17	697.71	1.5717	60.54
5.99	5	M	529.71	516.97	661.27	1.1368	44.52
5.39	5	F	487.27	489.31	586.32	1.4625	52.57
5.55	5	F	572.84	542.66	637.11	1.3163	36.31
5.54	5	M	546.17	572.95	693.62	1.3321	43.26
5.76	5	M	548.83	525.06	652.08	1.2649	38.2
5.31	5	F	548.11	519.57	656.23	1.4751	36.61
5.38	5	M	545.81	522.46	643.43	1.3992	31.53
5.46	5	F	550.82	525.16	669.06	1.5119	42.67
5.46	5	M	531.11	519.89	630.37	1.2884	30.77
5.99	5	M	560.7	532.07	647.88	1.2736	25.87
5.33	5	M	505.04	570.83	663.01	1.3358	42.07
5.02	5	F	526.09	475.02	620.96	1.2617	29.32
7.92	7	F	550.47	505.6	627.57	1.2735	29.74
7.92	7	F	533.04	482.48	599.2	1.2776	37.55
7.96	7	M	527.13	476.33	579.48	1.4243	29.64
7.15	7	F	518.72	526.29	689.12	1.2579	24.92

to classify $fMRI$ data. Conducting feature selection with high-dimensional neuroimaging data is challenging considering the numerous types of DL architectures.

- Significant numbers of $fMRI$ dataset samples are necessary for deep learning architectures to be able to both outperform in a particular dataset and generalize to different datasets.

- The presence of noise may make a system less efficient, both in terms of training effectiveness and classification accuracy. The difficulty of learning in noisy environments has been emphasized in the architecture of deep neural networks.

- The challenge of using the RNN-based $LSTM$ model for the classification of neurological disorders is its computational complexity. There are many parameters and operations in the $LSTM$ model, and training and optimization are challenging, especially for high-dimensional data. The disappearance as well as the growing gradient issues also affect $LSTM$, which prevents the acquisition of long-term dependence, which creates instability and leads to divergence.

Most of our work has focused on addressing these problems and presenting an effective method to overcome them. The following are the main findings of our study.

- **$fMRI$ data and DNN model for better classification of neurological disorder:** Processing 4D-fMRI data might be difficult because of its high dimension.Voxels demonstrate the characteristics and correlations between them in 4D fMRI data. Here, each voxel's dimension is taken into consideration as $(x \times y \times z \times t)$ spatial resolution. It is necessary to reduce the dimension. For this specific purpose, tensors are used to develop an algorithm to reshape the data $rs-fMRI$, helping to achieve the vector of characteristics. Furthermore, these feature vectors are used as

a pre-trained value for deep neural network (DNN) models that classify neurodevelopmental disorders, that is, neural activity, and generate the saliency map for the active region of the brain. Specifically, while using time series $fMRI$ data within time series feature extraction, such as models based on RNN and $LSTM$, to save time and resources, this is necessary for training a DNN. Accurate regularization and fine-tuning of the two different variants, such as stack $LSTM$ and $BLSTM$ results in models that have become substantially more resilient to a considerable amount of training data for the classification of ADHD.

Despite the increasing popularity of $CNNs$ in order to analyze the data $fMRI$, it is essential to interpret the activations of the features of the CNN model as saliency maps, which can provide a better understanding of the model training process. In order to achieve efficient visualization, the CNN-based pre-trained model is MobileNet, which is combined with $2D-CNN$ to identify complex features from $fMRI$ data. The most vital aspect of the MobileNet $2D-CNN$ model is the class activation map (CAM) for Multiple Sclerosis in MRI images, which is obtained through the weighted feature map governed by the softmax weight that classifies the heat map corresponding to a specific class. The most important aspect of the CNN model is the pixel-level interpretation of the MRI image. The feature attribution method is useful to interpret the classification during the implementation of the CNN model, which emphasizes the significance of each feature of the MRI image data that has an effect on the model evaluation. For better classification and extraction of characteristic features of brain disorders and brain activity, we propose an algorithm to reshape the mechanism of $4D-fMRI$ data and various DNN models.

- Algorithm for reshaping $4D - fMRI$ time series data into a data array $2D$.
- An improved $BLSTM$ framework to perform classification of brain disorders $ADHD$
- MobileNet: $2D - CNN$ model for identification of MS features map that predicts the MS
- Analyzing and demonstrating the non-linearity of a CNN model while applying the gradient-based visualization for MRI images.

- **Gradient analysis of an MRI image and determination of the functional connectivity measure using the $BOLD$ signal**: During the diagnosis of speech arrest, image-edge detection MRI is a difficult task. To overcome this situation, we provide a set of computation methods that allow a more accurate visualization of the edges of the MRI image. In this procedure, there are two distinct essential components: the intensity of pixels and the region of interest (ROI), which require the generation of an edge map. Some $ROIs$ follow certain statistical analyzes using the region, and in the case of fMRI resolution, the statistically significant nature of the voxel is taken into account. The ROI approach uses the arbitrary gradient histogram to obtain edge detection. For the approximation of the histogram, the normal distribution of the intensity demonstrates a rapid fluctuation in intensities that is associated with the probability of pixels. We implement the three methods for the localization of intensities:
  - The scalar operator or the Laplacian operator.
  - Sobel operator for edge detection
  - Prewitt operator for the extraction of the edge of the MRI image

1.8 Structure of the Thesis

There are six chapters in the thesis.

Chapter 1: This thesis's work emphasizes the application of deep learning to classify the whole brain $fMRIs$ according to features. This chapter provides a brief introduction to $fMRI$ and its application. Following a concise technical description of EPI, $rs-fMRI$, and RSN. We discuss how these concepts could possibly be applied in order to understand brain disorders and neural activity. We provide more details regarding the statistical study of brain images. Regarding the introduction and objectives of the research work, we demonstrate the deep learning models and how $fMRI$ can be used to more effectively understand neurological disorders and activity.

Chapter 2: We present the existing theoretical and experimental Deep Learning framework used in brain image analysis. The preceding research categorization focuses on the findings of $fMRI$ and provides an in-depth analysis of how deep learning techniques and models are currently used in $fMRI$ data from tasks and resting states $fMRI$ for classification, identification, and clustering of cognitive disorders.

Chapter 3: This chapter demonstrates an experimental approach to functional connectivity analysis. We propose an approach for obtaining features that chooses the most significant voxels. Demonstration of different algorithms for connectome analysis, neural activity identification, and blood oxygen level-dependent signal analysis ($BOLD$). A CNN and $LSTM$ framework has been developed for the classification of brain disorders such as $ADHD$ and Multiple Sclerosis, the generation and detection of Saliency Maps,

and the classification of neural activity based on data from $rs-fMRI$.

Chapter 4: We propose an algorithm for $BOLD$ signal analysis. We presented Functional Connectivity FC which serves as the basis for the correlation representation of high-dimensional $fMRI$ data. We provide the gradient information of the MRI images, which includes distributed voxel intensities and contrast.

Chapter 5: In this chapter, we demonstrate our findings from experiments, which were presented and discussed. Compared to some previous studies, classifiers are based on time series data $fMRI$. Describe the findings of $rs-fMRI$ preprocessing, including the formulation of functional brain networks. We introduced the bidirectional $LSTM$ model with a slight modification and the $2D-CNN$ model that classifies neurological disorders such as $ADHD$ and Multiple Sclerosis (MS). We presented an algorithm to generate the saliency map of $fMRI$ images and classify neural activity using the deep learning-based model.

Chapter 6: This chapter is summarized in the conclusion. Discussion of the more comprehensive and careful analysis of the findings recognizes the limitations of this study and illustrates the potential relevant gaps in the research and future directions.

1.9 Conclusion

In this chapter, we provide a discussion of the neuroimaging modality and the use of deep learning for the analysis of neuroimaging data. The prediction provides one of the primary

features of $DL's$. This technique has been applied to neuroimaging data with remarkable success. On the basis of end-to-end learning, this is an important aspect that has recently been established. The possibilities of deep learning in neurological disorders are very intriguing when high-dimensional neuroimaging data is employed, such as $fMRI$. The functional MRI has the ability to quantify brain activity, and these quantitative data, which are derived from fMRI, are used to measure the $BOLD$ signal with activation. Task-based fMRI experiments have been essential for our present understanding of how the brain functions. $rs-fMRI$ is concerned with spontaneous low-frequency fluctuations ($< 0.1Hz$) in the $BOLD$ signal. The $BOLD$ response function ($fMRI$ time series) and the RSN characteristics are extracted by CNN with distinct layers. Another kind of $DNNs$ known as RNN, is possibly very useful for application in fMRI time-series data to make useful predictions.

CHAPTER 2

REVIEW OF LITERATURE

2.1 Introduction

The framework of this review could be properly categorized into two distinct sections. This chapter covers existing research first, then moves on to the methods that are associated with the issue being addressed. More specifically, in this chapter, we give a brief review of various well-known deep learning models and discuss deep learning models for $fMRI$ images, neural activity, and brain disorders, including $ADHD$ and Multiple Sclerosis. Subsequently, we discuss the limitations of deep learning models in neuroimage analysis. The previously proposed algorithmic methods for brain disorder and brain activity in images $fMRI$ were explored and considerably reviewed. In addition, we go through the deep learning models that are used to analyze the entire process to validate the findings of brain disorders and neural activity in images $fMRI$.

2.2 Deep Learning Techniques and Neuroimaging

The application of deep learning models is increasingly prevalent in order to identify task-adaptive features in image applications. The standard image automation workflow analysis has become more challenging as a result of a state-of-the-art deep learning framework, most significantly convolutional neural networks (CNN) Vieira et al. [22]. Several studies have successfully incorporated neuroimaging methods to quickly identify, evaluate and treat brain disorders, such as mental illnesses, neurodevelopmental disorders, and neurological disorders Dvornek et al. [95] Hinton et al. [96].

2.2.1 Deep Learning Models

Deep learning's potential is to provide automation in the identification of hidden and more complex data that has been abstracted and is based on high-dimensional neurological imaging data. This might be an essential part of understanding complicated neurological disorders Yan et al. [97] Zeng et al. [98] Dvornek et al. [99] Durstewitz et al. [100] Davatzikos et al. [101]. Here, we discuss the main principle for basic deep learning models, which are widely used in neuroimage analysis. These models comprise deep generative models along with feedforward neural networks such as Deep Belief Network (DBN), Generative Adversarial Networks (GAN), Convolutional Neural Networks (CNN) and Recurrent Neural Networks (RNN).

(I) **Deep Belief Network**

An easy-to-use and effective layer-wise training approach is proposed by Hinton et al. [96] to create a deep belief network that is stacked with several restricted Boltzmann machines ($RBMs$). There are generally two stages of training DBN:

(i) training with successive layers; and (ii) fine tuning. Training with successive layers includes unsupervised training across each RBM and backpropagation errors are used to fine-tune the topics discussed in Hecht-Nielsen [102] and the parameters after unsupervised training of DBN were defined in Dalto et al. [103]. A simplified analysis of the RBM model was performed by [Hinton [104]. The RBM is distributed among the first two layers, in which the observable units are (x) and (K) hidden layers are (L), therefore, the joint distribution of DBN is represented as:

$$P = (x, l_1 l_2 \dots l_K) = P(x|l_1) \left(\prod_{k=1}^{K-2} P\left(l_k | l_{k+1}\right) \right) P(l_{k-1}, l_k)$$

The Where k^{th} hidden layer has been trained with RBM using the data gathered from observation. From the $k - 1^{th}$ layer, the characteristics were learned.

- **Deep Belief Network on fMRI** However, DBN is widely utilized in speech processing as well as the detection of images. Only a certain number of studies have used it on complex neuroimaging data such as $fMRI$. Plis et al. [105] presented many examples of how deep learning frameworks have been used with $fMRI$ data. Their findings demonstrated the effective impact of exploratory analysis for the detection of latent connections and physiological representations using DBN learning. Kuang and He [106] used the algorithm DBN for the extraction and classification of features using fMRI data from the ADHD-200 cohort to classify the $ADHD$ brain disorder from the control.

(II) **Generative Adversarial Networks**

As a result of their ability to learn deeply encoded representations without highly labeled training data, GAN has generated a lot of interest in computer vision.

This network has found its direction in Goodfellow et al. [107] Grnarova et al. [108]. Notably, there has been a growing focus on them because of their potential to generate data and because they are extensively employed in several domains, encompassing segmentation and classification. *GANs* are being extensively used in a variety of image algorithms, as the performance rate of the *GAN* models is better for image processing problems. Several research papers have also summarized and categorized the most recent models related to *GAN*, which are discussed and classified in terms of loss function and especially in model development Creswell et al. [109], Guo et al. [110]. Their study focused on the refinement of model development, summarized in terms of supervised and unsupervised algorithms Hong et al. [111]. The improvement in stability and quality are the results generated from the model based on *GAN*, as proposed by Salimans et al. [112]. In the *GAN* extensive analysis of $2D$ to $3D$ image transformation, the relevant data set must first perform real-time data retrieval and develop a standard with significant features discussed in Wu et al. [113]. The main goal of *GAN* is to train a generator, that is, a convolutional neural network, together with a discriminator, which is a deconvolutional neural network. These architectures are discussed in Hiasa et al. [114]. The goal of generation can also be classified as data simulation and data augmentation for a limited data set Zhang et al. [115]. Generally, the *GAN* model is built as a min-max game. In this model, the generator network (G) tries to minimize the discriminator network (D) by using the latent space vector (Z) while (D) performs improvements and differentiates between actual and generated data. The two networks generate an attempt to optimize the most efficient way to achieve individual goals, since each network has its own objective function, as shown in Figure. 2.1. The cost value of

both networks is defined as

$$L_{(GAN)} = V(D,G) = \mathbb{E}_{X\sim p_{data}(X)}\big[LogD(X)\big] + \mathbb{E}_{Z\sim p_Z(Z)}\Big[Log\big(1 - D(G(Z))\big)\Big]$$

Where $\big[LogD(X)\big]$ is a loss function for the discriminator network and $\Big[Log\big(1 - D(G(Z))\big)\Big]$ denotes a loss function for the generator network and the two distinct networks.

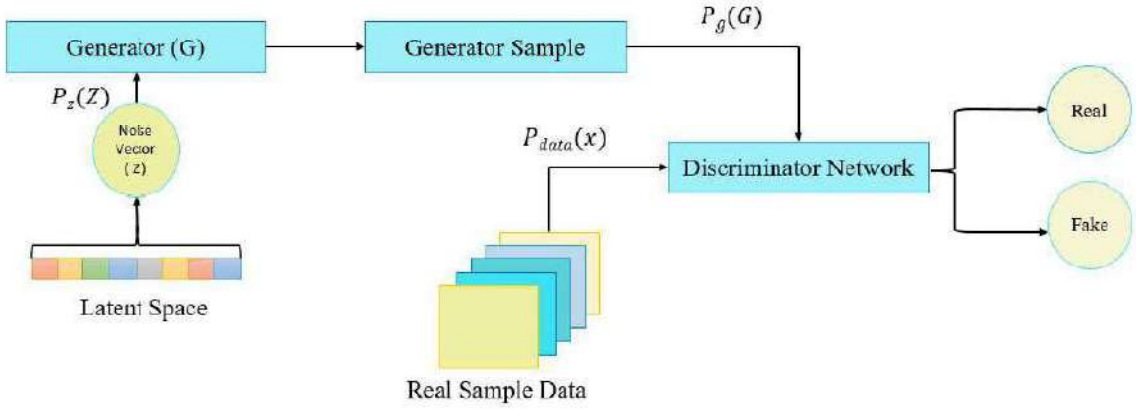

Figure 2.1: Architecture for GAN, where D's goal is to maximize its cost and G's goal is to minimize its cost.

Several variants of GAN such as Deep Convolutional GAN ($DCGAN$) proposed by Radford et al. [116] to improve the training process of GAN and modify the original model GAN. Wasserstein GAN ($WGAN$) was proposed by Arjovsky et al. [117] in which they modify the stability of learning in the original GAN model and produce significant learning curves. Vanilla GAN ($VGAN$) was created by Jiang et al. [118] to perform by retrieving sample data, which depend on a certain data distribution, despite particularly modeling the fundamental probability density function. The vanishing gradient problem will nevertheless take place while undergoing the learn-

ing phase, therefore, resulting in a loss function. With respect to this problem, Mao et al. [119] proposed a model of generative adversarial networks of least squares ($LSGANs$) that acquires the loss of least squares. A generator in the original GAN model entirely produces a latent space. The conditional GAN rectifies this challenge, which is proposed by Mirza and Osindero [120] by providing an additional parameter to the generator added to latent space and finally training the GAN model to generate the resulting images. Map the actual data set to the latent data by using mapping methods for the probability distribution of the actual data to the latent data.

- **Generative Adversarial Networks for Neuroimaging:** This GAN method has a lot of potential for neuroimaging applications. Several previous studies of $GANs$ have mainly focused on the technical aspects of medical imaging. Yi et al. [121] discussed and performed the review of the latest advancements in the adversarial training mechanism in medical images; Sorin et al. [122] their reviews focus on the reconstruction of various modalities of medical images such as CT, MRI, PET/CT and PET/MRI using the model GAN. Qu et al. [123] systematically provide reviews and summarize the application of the original and various variants of the GAN models for the classification of Alzheimer's disease. Laino et al. [124] discuss descriptive reviews for the application of the GANsegmentation, model for brain imaging, such as progressive disease modeling, image segmentation, and brain decoding.

(III) **Convolutional Neural Networks (CNN)**

Deep learning techniques such as CNN, which are capable of learning data repre-

sentations, could have been used effectively in many different kinds of fields LeCun et al. [125]. The CNN was developed in order to store and use crucial data more effectively between adjacent pixels and simply require a small amount of preprocessing using images that are two-dimensional $2D$ or three-dimensional $3D$ as input LeCun et al. [126]. Krizhevsky et al. [127] suggested the standard CNN design serves a computer vision task that includes three different types of layers, ie, convolutional layers, pooling layers, and dense layers or fully connected layers. To classify a problem with studies related to DL, various CNN-based classification frameworks have been created, including MobileNet Howard et al. [128], ZFNet Zeiler and Fergus [129], EfficientNet Tan [130], Inception Szegedy et al. [131], ResNet He et al. [132], GoogleLeNet Szegedy et al. [133], AlexNet Krizhevsky et al. [127] and VGGNetSimonyan and Zisserman [134]. A new state-of-the-art deep architecture model DL that can derive significant details using medical data and predict the variation proposed by Nguyen et al. [135].CNNs are used in the classification of brain disorders, as described in Zhang et al. [136]. Firat et al. [137] proposed a CNN-based architecture known as the temporal CNN model that uses spatial clustering for neural decoding. Dolz et al. [138] evaluated the HyperDense-Net framework from neonatal neuroimaging data to illustrate the performance of the proposed model.

- **Convolutional Neural Networks on fMRI Data:** According to Bernal et al. [142] (2019), convolutional neural networks ($CNNs$) have been used in multiple areas of neuroimaging. CNN convolution approach may extract data from pre-processed $fMRI$ images and the distinctive features of neighboring voxels to present all the complicated features used in disorder classification. The strategy is based on CNN, and the method has been shown to be effective

Table 2.1: **Observation and characteristics between the different Pre-trained CNN models**

Author	**Model and Year**	**Layers**	**Parameter**	**Major Feature**
LeCun et al. [139]	LeNet-5 1998	7	0.060 M	Simple to implement and effective in resolving smaller image recognition
Krizhevsky et al. [127]	AlexNet 2012	8	60 M	LeNet-5 & AlexNet are identical while AlexNet is a deeper. Filter Size in 3×3 , 5×5 & 11×11.
Zeiler and Fergus [129]	ZfNet 2014	8	60 M	Applied Deconvolution while error backpropagation in the convolution Layer.
Simonyan and Zisserman [134]	VGGNet 2014	16 & 19	134 M	3×3 kernels are used in each convolution layer.Stacked convolutional layer.
Szegedy et al. [133]	GoogLeNet 2015	22 & 9	4 M	Convolution & pooling layers operate simultaneously a lesser computationally intensive model than AlexNet & VGG-16
He et al. [132]	ResNet 2016	50 & 101	25.6 M	Core of batch normalisatusage of ion of identity connection.Uses bottleneck residual block.
Szegedy et al. [131]	Inception V3 2016	42 & 10	22 M	Enhances a network efficiency.Batch Normalisation allows for faster training. Building blocks efficiently going deeper.
Chollet [140]	Xception 2017	50 & 71	8.6 M	Depthwise convolution followed by a Pointwise convolution
Huang et al. [141]	DenseNet 2017	201	8.06 M	It is including a transition layer & dense blocks
Howard et al. [128]	MobileNet 2017	28	4.2 M	Lightweight Deep CNN using depthwise separable convolutions.

in detecting brain disorders in several research studies. Sato [143] presented a technique based on CNN to segment brain tumors, this architecture CNN consists of a sequential 5-layer network where five distinct categories are created

from the images MRI using the CNN model. Labels for two classes, such as 0 and 1 when determining outgoing edges, are discussed in Agrawal and Thierauf [144]. Li et al. [145] used the $3D-CNN$ model to extract important features from the whole brain to estimate the age of the brain. Sarraf and Tofighi [146] Used a LeNet-5-CNN model have incorporated $rs-fMRI$ data as well for the AD classification by converting an array of $2D-fMRI$ images from $4D-rs-fMRI$ data.

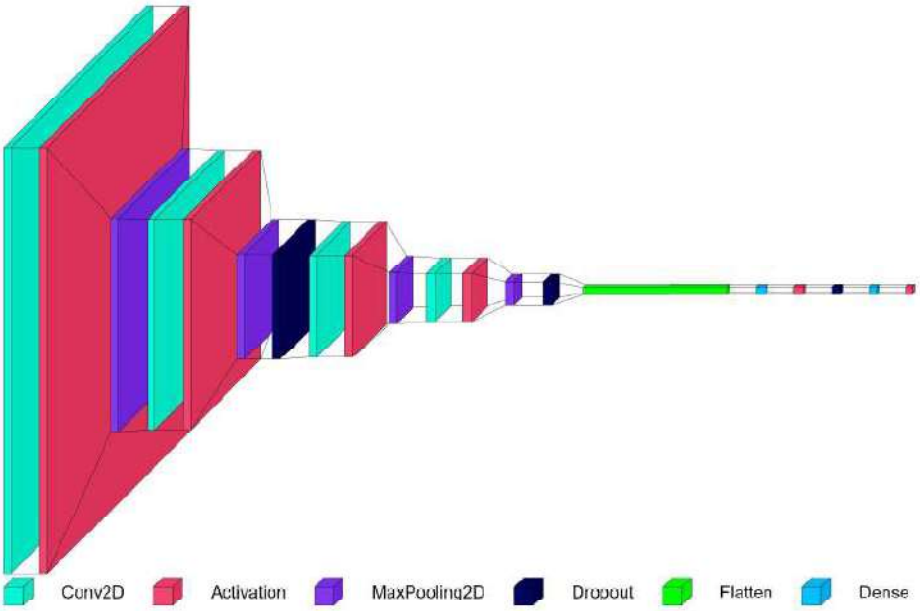

Figure 2.2: Architecture of Convolutional Neural Network

Zhao et al. [147] proposed a $3D$ convolutional kernel-based CNN model that can effectively classify the functional networks of the human brain using whole brain fMRI data to reconstruct the brain, and this model has excellent classification capacity while using the Human Connectome Project (HCP) $fMRI$ image. Zou et al. [148] proposed a multimodality CNN model that classifies neuroimage among healthy subjects and $ADHD$ applying $fMRI$ images. $3D$ voxel-wise $fMRI$ data classification using models based on CNN, Mitchell et al. [149] converted a $3D-fMRI$

image into a $2D$ mean value $fMRI$ image along the z axis for classification using the $2D-CNN$ model. Neuronal visualization can be seen by the $fMRI$ signal in terms of the observed image. Therefore, an interpretation of an image.Agrawal et al. [150] $fMRI$ signals were initially encoded using CNN characteristics taken from $fMRI$ images. Güçlü and van Gerven [151] has shown a correlation between CNN characteristics of the composition layer of the model $VGG-19$ and $fMRI$ activity. The task of analyzing fMRI activity is to interpret the observed $fMRI$ signals, and it uses CNN features to display the image that is being observed. Richards et al. [152] Classified $4D$ task fMRI time series data using $3D-CNN$. $3D$ voxel-wise $fMRI$ data classification using models based on CNN An objective for classifying data evoked by tasks $fMRI$ using computational techniques is to create feasible prediction models that can detect how the brain responds to various types of task activation Wang et al. [153].

(IV) **Recurrent Neural Network (RNN)**

This is an abstraction of an internal memory-equipped feedforward neural network. RNN has had the capacity to process, remember, and retain complicated signals for a very long time due to this model. RNN is capable of handling data streams of different lengths, which has been demonstrated in neuroimaging data, specifically $fMRI$ time series data Livezey and Glaser [171]. RNN is capable of handling every previous input from the sequence. Moreover, from the subsequent sequence, which will evaluate the temporal dynamic behavior, the most significant advantage of switching from traditional neural network models to $RNNs$ is that, over a period of time, their weights are distributed throughout the neurons in hidden layers.

Table 2.2: **Summary of CNN Models for detection and classification of various brain disorder**

Reference	Deep Model	Sample Size	Datatype	Neurological Category	Featured Objective
Cherukuri et al. [154]	CNN	15	CT	Neurological Disorder	The volume of CSF has to be measured
Vu et al. [155]	3D-CNN	1440	fMRI	BOLD Response	Classification of Neuronal Activation
Talo et al. [156]	CNN	1074	MRI-T2WI	Neurological Disorder	Classification of Brain Disorders
Mao et al. [157]	4D-CNN -LSTM	ADHD -200	rs-fMRI	ADHD	ADHD Diagnosis
Wang et al. [158]	CNN	624	MRI-T2WI	Alzheimer's Disease	AD vs MCI Classification
Eitel et al. [159]	CNN	147	MRI-T2WI	Multiple Sclerosis	Multiple Sclerosis diagnosis
Wang et al. [160]	CNN	334	MRI	Brain Tumor	Diagnosis of Liver Tumor
Rauschecker et al. [161]	3DU-Net	517	MRI-T1	Brain Lesions	Brain Tumor Segmentation
Meng et al. [162]	CNN	30	Retinal Vessel	Cerebrovascular	Cerebral vessel Segmentation
Ko et al. [163]	CNN-LSTM	727392	CT	Stroke Trauma	Intracranial Haemorrhage detection
Phang et al. [164]	CNN	84	FC	Schizophrenia	Schizophrenia diagnosis
Park et al. [165]	FCNN	102	MRI-T2WI	Parkinson's Disease	Segmentation for DBS
Dubreuil-Vall et al. [166]	CNN	40	EEG	ADHD	Healthy Control vs. ADHD
Guilherme et al. [167]	3D-CNN	23165	sMRI	Alzheimer's Disease	AD vs MCI
Dyrba et al. [168]	CNN	663	MRI-T1WI	Alzheimer's Disease	AD MCI
Özyurt et al. [169]	CNN	500	MRI-T1WI	Brain Tumor	Brain tumor detection
Wang et al. [170]	CNN -LSTM	144	EEG	ADHD	ADHD and subtypes

$fMRI$ time-series have been correlated over time; therefore, $RNNs$ are capable of being used to decode neuronal activity Huang et al. [172]. For the analysis of

the data $fMRI$, neural activity as an effect of sensory stimulation could be accurately modeled through RNN Güçlü and Van Gerven [173]. The vanishing gradient problem influences RNN while using the high-dimensional feature vector as input. The problem of gradient vanishing is solved with long- and short-term memory ($LSTM$), since it is developed by releasing memories Hochreiter and Schmidhuber [174] Hochreiter et al. [175]. Therefore, a particular kind of RNN is an LSTM network. As stated above, $LSTM$ prevents vanishing gradients and allows identical credit assignment. For the weight adjustment that is connected to the network, a complete gradient training is used in the $LSTM$ model given by Graves and Schmidhuber [176]. $LSTM's$ capacity for learning has an influence on several areas; eventually, it became a state-of-the-art model. Without any uncertainties for the implementation, a neural network would not be as widely used in the absence of an excellent theoretical foundation. Recently, a study carried out by Yi et al. [177] presents a summary of the $LSTM$ cell and its features and various architectures. The basic $LSTM$ unit consists of a cell with a forget gate, an input gate, and an output gate. The $LSTM$ network did not originally have a forget gate.Andersen et al. [178] uses the forget gate in the $LSTM$ network state, which has to be reset.$RNNs$ offer computing structures that can be used to predict spontaneous brain signals over time because $RNNs$ are created by connecting pairs of basic neurons that are recurrently coupled, which encode the temporal occurrences of the input data, such as rs-fMRI signals and learning within processes. After that, these conditions are decoded to provide predictions.

- **Recurrent Neural Network for Spatiotemporal Data:** There are plenty of problem domains where the $LSTM$ network is used. As has already been

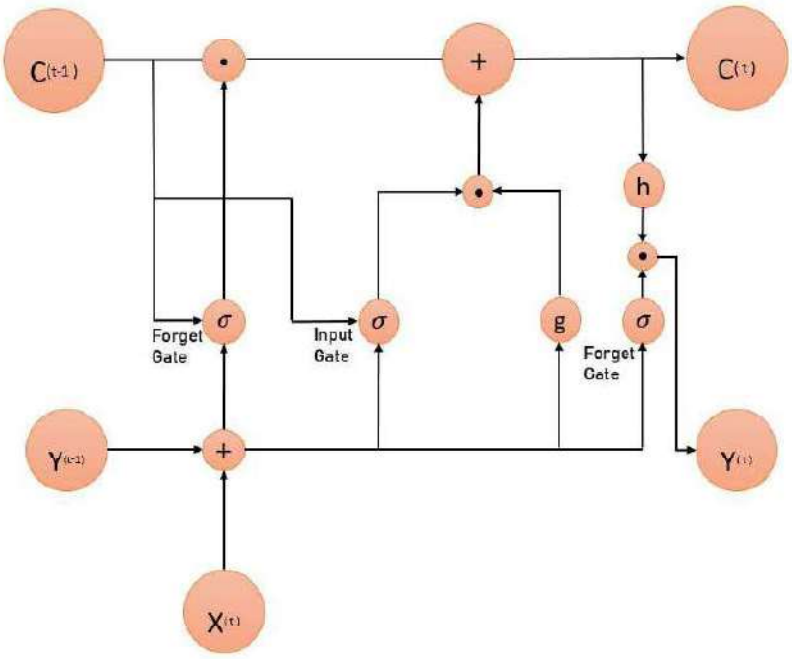

Figure 2.3: Vanilla LSTM architecture, which is composed of the different gates, where the input signal and output signal are denoted by $X^{(t)}$ and $Y^{(t)}$, respectively, along with the peehole connection and activation function, i.e. gate activation function (σ), input gate activation function (g), & output gate activation function (h).

stated, $LSTM$ serves as one of the most sophisticated networks for processing temporal sequences. Gers and Schmidhuber [179] proposed time series data for Gers and Schmidhuber [179] are modeled using $LSTM$ and then subsequently integrated with the input of text data, which enhances the predictions. Even when time series data is provided as input, the LSTM model may not always be able to make accurate predictions based on the subsequent data in the series since this information can be used to learn a classifier.Uddin [180] showed that the $LSTM$ model has the ability to recognize a task that has been performed based on data provided by many wearable medical sensors.Hou et al. [181] proposed a method to identify face features to obtain images and videos captured under independent circumstances. The present strategy constitutes an integrated framework that, with other $LSTM$, can completely use both temporal

and spatial data to improve accuracy. To enhance the efficiency and accuracy of $LSTM$ models, more than one $LSTM$ layer is often needed to be stacked on top of each other. A modification of the $LSTM$ model is the stacked LSTM which contains several hidden $LSTM$ layers in which several memory cells are present on each layer and is discussed by Yu et al. [182].

- **LSTM on fMRI Time Series Data:** Xu et al. [192] studied using functional near-infrared spectroscopy ($fNIRS$) data to identify autism in subjects and observed that applying a $CNN + LSTM$ classification method helped to detect ASD. Yoo et al. [194] studied $fNIRS$ data to measure sound stimulation in the auditory cortex for the classification of subjects without any feature selection using the $LSTM$ model. Sirpal et al. [190] implemented $fNIRS$ data along with multichannel EEG data using the $LSTM$ model to identify seizures. Another clinical use was studied to obtain $fNIRS$ measurements using deep learning methods Fernandez Rojas et al. [195] using unprocessed $fNIRS$ data using the $LSTM$ model, through which high and low degrees of pain are differentiated. During an activity that requires cognitive effort, Asgher et al. [193] used a model $LSTM$ and observed identical extracted characteristics considering the time domain signals for HbR together with HbO_2; a classification of cognitive strain was established. When requesting participants to complete an activity, Zhao et al. [191] addressed this problem, which implemented a model $LSTM$ to identify whether tasks had been completed. Zhang et al. [187] proposed an integrated model composed of $LSTM$, CNN and an auto-encoder (AE) to extract useful characteristics from motor imagery electroencephalography ($MI - EEG$) to identify the letter that the participant wishes to speak. Most biometric identification systems depend on inherent physiological features. Zhang et al. [188] presented an $LSTM$ model with an attention module to determine user ID using the EEG signals.

Table 2.3: **Summary of RNN and LSTM Models for detection and classification of various brain disorder**

Author	Model Year	Datatype	Sample Size	Featured Application
Dvornek et al. [95]	LSTM 2017	rs-fMRI	1112 (ABIDE-1)	Classification of ASD & TD
Alhagry et al. [183]	LSTM +MLP,2017	EEG	322 (DEAP)	Emotion Classification
Supratak et al. [184]	CNN 2017	EEG	62	Facial Expression
Zhang et al. [185]	RNN +BLSTM,2017	EEG	15	Sleep stages identification
Shah et al. [186]	CNN+LSTM 2017	EEG	19 Channels EEG signals	Seizure Detection
Dvornek et al. [99]	LSTM 2018	rs-fMRI	1112 (ABIDE-1)	Identification of ASD
Zhang et al. [187]	Attention -based RNN,2018	EEG	28000/sub (sub = 10)	Brain Computer Interface
Zhang et al. [188]	LSTM +CNN +AE,2018	EEG	8	User-ID using brainwave
Correa and Patras [189]	CNN +RNN,2018	EEG	37	Personality Trait
Sirpal et al. [190]	LSTM +CNN 2019	fNIRS EEG &Multimodal	40	Epileptic Seizure Detection
Zhao et al. [191]	BLSTM 2019	fNIRS	47	Recognition cerebrovascular accidents
Xu et al. [192]	LSTM 2020	fNIRS	47	Diagnosis of ASD TD
Asgher et al. [193]	BLSTM 2020	fNIRS	192	Cognitive & Mental Workload
Yoo et al. [194]	LSTM 2021	fNIRS	18	Decode & Hemodynamic Response
Fernandez Rojas et al. [195]	BLSTM 2021	fNIRS	18 Non-Verbal	Pain Evaluation

Alhagry et al. [183] used an $LSTM$ model to extract features from emotion-related signals EEG, and these features are advanced to MLP for classification. Supratak et al. [184] developed a deep learning model by combining several views of $LSTM$ and CNN to provide an automated evaluation of the sleep stage, where CNN described the time-invariant dependencies and bidirectional $LSTM$ was used for the temporal characteristics while sleeping. Zhang et al. [185] demonstrated a spatial-temporal RNN model, which uses a RNN layer with many directions to identify distant elements of the context and another bidirectional RNN layer to gather recurrent features resulting from the preceding spatial RNN. Correa and Patras [189] presented a cascaded deep learning model using RNN and CNN together to predict personality detection. Shah et al. [186] explored $CNN - LSTM's$ combined efficacy for seizure detection using the EEG channel. Dvornek et al. [95] proposed a $LSTM$ model for the classification of ASD and typical controls directly using the $rs-fMRI$ data. Dvornek et al. [99] present various approaches to applying phenotypic data with the $rs - fMRI$ Autism Brain Imaging Data Exchange ($ABIDE$) to classify the ASD from the $LSTM$ framework.

2.2.2 Functional Magnetic Resonance Imaging (fMRI) Schemes

Noninvasive procedures can determine cerebral physiological responses during neuronal activation. $fMRI$ has been one of the significant methods by applying an MRI procedure that measures neurological activity by identifying $BOLD$ (blood oxygen level dependent). A higher blood oxygen level will lead to a more significant $fMRI$ signal, as discussed by Geyer et al. [46]. The primary objective of $fMRI$ data analysis is to explore the time series information of every voxel to identify how much the $BOLD$ signal has occurred in response to a specific stimulus and, subsequently, to identify neural activity. Several

neuroimaging methods have been used for the study of neurodegenerative disorders, as discussed by Wolters et al. [196]. Baggio and Junqué [197] proposed one possibility: that $rs-fMRI$ with its consistency and reliability, is capable of evaluating regional $BOLD$ signal variations and highlighting the underlying functional anatomy of the brain.

fMRI BOLD Signal

The initial research on humans $BOLD\ fMRI$ was published in 1992 by Destrieux et al. [44]Bandettini et al. [198]Kwong et al. [199]. fMRI depends on the measurement $T2*$ and is more susceptible to neighborhood concentrations of deoxyhemoglobin paramagnetic, as defined by Destrieux et al. [44].

(a) In response to the functional stimuli, positive $BOLD$ responses are observed, indicating a drop in HbR resulting in an overoxygenation from the response area, as observed by Attwell and Iadecola [200]. To analyze the signals of $fMRI\ BOLD$ proposed by Boynton et al. [201], the neurovascular coupling typically appears to be deep whenever there is a rise in neuronal activity that significantly improves local blood flow, regardless of the pathological condition of the brain region, as well as the neurodevelopment studied by Logothetis [202]. Schölvinck et al. [203] emphasizes that the global significance of the fluctuations in $BOLD$ signal recorded at $rs-fMRI$ is, in fact, closely related to a weak modulation of apparently prevalent neural activities in the cerebral cortex.

(b) The time-dependent characteristics of the $BOLD$ signal are influenced by hemodynamic responses that include related fluctuations CBF and CBV. An illustration is shown in Figure. 1.8. From HRF an instantaneous stimulus is provided at time $t = 0$ seconds.

2.3 MRI Edge Identification

Magnetic resonance images have become a crucial component of medical diagnosis and treatment. Numerous noises, imaging inaccuracies, and other factors can affect MRI images. MRI images have unclear edges; therefore, an extensive study is required on MRI image edge identification. Qian [204] used the Sobel operator to determine the magnitude and direction of the gradient. Karras and Mertzios [205] applied the Sobel filter to the MRI image and obtained edge detection without Gaussian noise. Shankar et al. [206] gives a detailed discussion about coherent optical processing systems (COPS) that can solve many image processing problems. Cao [207] uses the Canny algorithm for edge detection in medical imaging. Xu et al. [208] apply the Canny edge detection on brain images and compute the gradient using a Gaussian filter to detect the edges.

2.4 Resting state-fMRI for Brain Disorder

The primary objective of RS-fMRI is to investigate spontaneous low-frequency fluctuations inside the $BOLD$ signal. Meszlényi et al. [12] was the first to highlight the functional importance of these factors.Fox and Raichle [209] analyzes spontaneous low-frequency fluctuation within $(0.01–0.1Hz)$. FC is the major metric produced by $rs-fMRI$, which is an estimate from the statistical correlation between any number of voxels and the underlying $BOLD$ signal's temporal dynamics.

(a) Different resting state networks were identified using rs-fMRI in healthy subjects and patients Smith et al. [210]. Since then, $rs-fMRI$ has been widely used by healthy and diseased subjects, including those with mental and neurological disorders, to examine spontaneous fluctuations present in various resting state networks Smith

[211].

(b) A significant $rs - fMRI$ experiment involving healthy subjects with $ADHD$ in adults discovered a default mode network (DMN) that had reduced functional connectivity. Since then, a significant number of studies with $rs - fMRI$ have been published among those with $ADHD$ Castellanos and Aoki [212]. Castellanos et al. [213] explore whether $RSNs$ are common in adults with $ADHD$ 20 previously discovered independent components and calculate their spatial cross-correlation. DMN activity among individuals with $ADHD$ was examined in two MRI studies that implemented metrics FC Uddin et al. [214]. Taking into account the data from $rs - fMRI$, the spatiotemporal dependence of neural behavioral patterns is termed functional connectivity of structurally distinct brain regions, as this study has proposed by Aertsen et al. [215].

(c) Functional connectivity between cerebral regions is taken into account by $rs - fMRI$. Several analysis methods used to examine connectivity $rs - fMRI$ are analyzed by applying independent component analysis (ICA) and seed voxel techniques Chen and Glover [216]. FC may be used for the purposes of imaging a biomarker of neurodegenerative conditions for brain function in the MS area proposed by Hohenfeld et al. [217]. Various studies show several FC patterns that change during various stages of the disease, including low FC within the progression of MS and the initial stage of MS Cocozza et al. [218] Basile et al. [219]. Roosendaal et al. [220]Demonstrate the FC in MS individuals with healthy spatial memory. Cecchi et al. [221] intended to compare the assessments FC with clinical measurements but chose not to because the subject with the $MS's$ FC metric did

not show any signs of disease.

2.4.1 RSN computation with rs-fMRI

The functions of the human brain are governed by a variety of complex networks, and despite spatial separation, the regions of the brain are connected. $RSNs$ indicate synchronized low-frequency ($< 0.1Hz$) occurs, temporal fluctuations without explicit tasks are studied by Damoiseaux et al. [65]. RSN extraction from high-dimensional $rs-fMRI$ data is a complex analytical problem that becomes feasible by appropriate technique; it is commonly known as ICA and is reviewed byArslan and Rueckert [57]. $RSNs$ derived from a spatial ICA are conceptually involved with fundamental assumptions. Lee and Frangou [222] proposed brain resting-state networks RSN can change in FC, either slightly or significantly. Most functional RSN studies are defined by correlation analysis in association with the different areas of the brain and the temporal behavior of the brain, determined by the degree to which voxels correlate with the signal.

2.4.2 Tensor ICA Approach in rs-fMRI data

A data-driven technique known as ICA allows for understandable splits of data, as it consists of a certain amount of linearly mixed sources achieved by analytical methods based on models by Beckmann and Smith [223]. The $fMRI$ data decompositions of the ICA comprise concatenation in time or space, and after that use a typical $2D-ICA$ decomposition strategy Lukic et al. [224].Harshman and Lundy [225] has proposed an abstraction that is known as a trilinear model of parallel factor analysis ($PARAFAC$).

$$X = \sum_{r=1}^{R} a_r \otimes b_r \otimes c_r$$

Three vectors, which together make up an input, represent the tensor product X.

2.4.3 DMN in Neurological Disorder

Various procedures related to DMN unusual events in mental disorders are proposed by SJ [226]. The FC of the DMN has received the majority of attention in empirical studies within the constraints of the $fMRI$ data and the $BOLD$ signal. An indirect assessment of neural activity that takes into account blood oxygen levels when comparing contrasts in the brainFox and Raichle [209]. It may be difficult to distinguish $ADHD$ symptoms compared to childhood misbehavior and the impact on various biological or mental factors, which is discussed in Bradstreet et al. [227]. Posner et al. [228] proposed a relationship in the pathophysiology of $ADHD$ in which there could be a significant role for the DMN cognitive control network. According to two studies Cao et al. [229], DMN dysfunction could have an impact on normal attentional activity in $ADHD$. DMN was extensively studied to evaluate the treatment results in $ADHD$. Liu et al. [230] proposed a new method named $MLP - CNV$ in which they used complex biological data to perform genome sequencing; furthermore, they applied structural variational intensities in the sequence region to perform the classification of disorder $ADHD$ from the healthy control.

2.5 Voxel-based Classification

Measurement of a voxel, which constitutes a rectangular cuboid $3D$ with a size in millimeters Λ specific cognitive function can be used to map the region of the brain through

the $BOLD$ signal of each voxel Worsley et al. [231]. Visualization was improved by voxel-based approaches that evaluate the results of the $3D$ brain space. It was discovered that there was a strong correlation between high connectivity and effectiveness. Functional brain networks composed of voxels have been defined as scale-free networks, as reported by Cecchi et al. [221] van den Heuvel et al. [232]. In several studies, a data-driven method is used in the $CONN$ toolbox to analyze data; typically, it is known as multi-voxel pattern analysis ($MVPA$) Muehlhan et al. [233] Whitfield-Gabrieli et al. [234]. The search procedure for highly recurrent spatial patterns of activities is part of $MVPA$ and varies depending on the experimental parameters. Consequently, $MVPA$ is considered a supervised classification problem in which the classifier draws the association between the experimental test condition and $fMRI$ activity Davatzikos et al. [235]. Aberg and Wessberg [236] examined the efficiency with which evolutionary algorithms perform when determining only a certain number of voxels that can most effectively distinguish between different volumes $fMRI$. Nakao et al. [237] apply voxel-based morphological evaluation in $ADHD$ reported a decrease within the volume GM of the lenticular nucleus.

2.6 Application of Deep Learning for Brain Disease

Various studies have been conducted with essential findings that distinguish the disease MS from the healthy control Akkus et al. [8]. These studies focus on the specific application of machine learning, including deep learning-based frameworks, and consider MRI scans to determine the severity of the disease. Beare et al. [238] have considered a deep learning-based architecture CNN and used a large volume of brain voxel data MRI for further analysis of MS lesion segmentation. Benedict et al. [239] have proposed

a CNN-based MS classifier known as DeepScan to identify the MS lesion. Birenbaum and Greenspan [240] have discussed various deep learning-based techniques that consider the publicly available Brain MRI image segmentation dataset. Chhatbar and Kara [241] discussed the framework known as Toolkit (ITK) and applied the watershed transform method for the detection of region boundaries in MRI scans. Cho et al. [242] have focused on effective neural network training to classify MRI images with limited data and to prevent overfitting the network. They have simplified the proposed model to optimize the volume of the dataset by using image data augmentation, which improves accuracy. Chollet [243] used precision reduction methods to reduce spatial resolution in different features of the feature map generated by the $LeNet-5$ network.Ding et al. [9] Oliva et al. [244]discussed the discrimination of the region in the input image, and the class activation map is influenced by the deep learning model for classification.

2.7 Conclusion

In this chapter, we present some important approaches and some theories on the future of deep learning. Numerous applications and in-depth studies on deep learning have already been carried out and have performed magnificently when used in real-world applications. The creator of GAN, Ian Goodfellow, demonstrated that by using opposing instances, neural networks can be strategically misled. But there is even more to be discovered in the field of deep learning and many possibilities for use, such as neuroimaging. We discussed previous studies on fMRI data to identify numerous brain disorders and neural activity using models CNN, RNN, and $LSTM$. In addition, visualization and classification based on CNN and $LSTM$ offer a clear understanding of the classification of neural

disorders. This might be an effective replacement for $fMRI$ data analysis.

CHAPTER 3

NEUROIMAGE ANALYSIS AND DEEP LEARNING MODEL FOR FMRI

3.1 Introduction

In this chapter, we discuss the methodologies of the (1) spatial neural gradient across the edge of the brain using comparative methods, as well as the identification of edges and ROI in $fMRI$ visualizations. Concentrated on work that uses multimodal neuroimaging data $fMRI$ together with the whole brain atlas to determine computer vision goals, including data for acute stroke speech arrest MRI located within the left precentral gyrus. We perform a clustering for $fMRI$ and a further analysis of FC in the $fMRI$ images. (2) However, spontaneous brain activity showed that the event occurred at a low frequency which is present during the $BOLD$ signal ($0.1Hz$). We developed a method to determine the correlation between the FC measure and neuronal activities that examined fluctuations of the $BOLD$ signal, which is constant between participants and areas of the brain. (3) Perform the classification for neural activity using $fMRI$ data with the proposed $2D - CNN$ model. When working with high-dimensional data $4D - fMRI$,

neuronal activity varies over time in FC, the extracted features using the correlation of various voxels. (4) Apply the feature selection method to reduce dimensionality, and this frequency domain feature is decoded by a bidirectional LSTM ($BLSTM$) network to classify the results of $ADHD$ and healthy control. (5) Apply a strategy to reduce distortion in the significance of a feature estimation using a nonlinear model such as CNN and feature attribution techniques. A guided backpropagation algorithm using the $ReLU$ activation function creates the saliency map of the $fMRI$ images that produce and analyze gradient maps to help understand how a CNN model behaves.

3.2 Proposed Methods

The variations within a voxel's activity level are observed within its $BOLD$ time series.To determine a time series that accurately demonstrates region of interest (ROI).Generally, ROI time series can be obtained as efficient visualizations of the voxels' motions inside the ROI.The ROI was used for extracting the BOLD signal. To identify the regions that are active during each task,Convolution was performed on a gamma-function.The BOLD signal's variations during periods of time are represented by the hemodynamic response function (HRF) which accurately describes brain activity.

3.2.1 Visualization of Region of Interest

fMRI images provide an experimental platform through which to view an active, functional human brain. A magnetic signal is present in the $fMRI$ image; these signals originate from hydrogen nuclei in water. The intensity of the hydrogen nuclei varies and depends on the environment; as a result, it serves as the mean of discrimination in structural fMRI,

which contains both matter, that is, white matter (WM) and gray matter (GM), as well as cerebral spinal fluid (CSF). Using $fMRI$ time series data, which distinguishes between neurobiological and non-neurobiological signals, to analyze FC. Monoexponential reduction $X(\tau) = x_0\ e^{-\tau/T2^*}$ is commonly used to model the signal $fMRI$ in a voxel. where x_0 denotes the intensity of the signal, $\tau = 0$ represents the activation of the radio frequency and $T2^*$ represents the time constant.

(a) Activity Response using Discrete BOLD Signal

Based on the HRF, the $BOLD$ activity responds to brain signals. The HRF model that represents the $BOLD$ signal as $x_i(t)$ with the respective HRF is $h_i(t)$ and the stimulus function $s(t)$, therefore it is possible to define its relationship as follows:

$$x_i(t) = (h_i \times s)t + v_i(t) \tag{3.1}$$

Where noise is denoted by $v_i(t)$, which takes place as the stimulus function $s(t)$, including $h_i(t)$ at $n = 1 \ldots M$ is being sampled, consequently, the $BOLD$ signal's discrete convolution for i^{th} pixel at n^{th} second is defined as:

$$x_{n,i} = \sum_{k=n}^{N} \sum_{j=1}^{N} S_{(N-k+n)} h_{(k,j)} + v_{(n,i)} \tag{3.2}$$

The matrix of stimulation $S \in R^{(M \times N)}$ and the temporal basis function T. The associated basis function $\psi(.)$ is used by every pixel in the $fMRI$ image. Thus, the HRF has been defined in the following matrix:

$$[h_i] = [\psi_1, \psi_2 \dots \psi_T] \times \begin{bmatrix} a_{1,i} \\ a_{2,i} \\ \vdots \\ a_{T,i} \end{bmatrix}$$

$$\left[h_i\right] = \left[\psi\right] \times \left[a_i\right] \tag{3.3}$$

The obtained design matrix is $\left[D\right] = \left[S\right] \times \left[\psi(.)\right]$ equations Eq. 3.1 and Eq. 3.3 therefore, the design matrix is $\left[D\right] \in \left[R\right]^{(N \times T)}$ displays the convolution model of the stimulus function $s(t)$.

(b) **Estimation of the correlation on BOLD-fMRI signals**

The $4D-fMRI$ image is represented as $\mathbb{R}^{(N_x \times N_y \times N_z \times T)}$ where the stimuli $3D$ of the image $fMRI$ are $N_x \times N_y \times N_z$ in time T. The dimensions of each slice $N_x \times N_y$ are determined along the z-axis; There are N_z number of slices, in which N shows the total quantity of voxels within various cortical regions. The extraction of the time-series BOLD signal through $4D-fMRI$ is applied to the $BOLD$ signals to determine the correlation; therefore, the stimuli could possibly be denoted by a linear function. The convolutional model of the linear function is represented as

$$g(s,t) = \sum_i \delta(t - i.\Delta) \times u_i^2(s,t) \times H_i(t) + g_i(s,t) \tag{3.4}$$

$g(s,t)$ and $g_{(i)}(s,t)$ are estimates of hemodynamic response and noise in a particular region of the brain s at some point t. $\sum_i \delta(t - i.\Delta)$ depicts the waveform that

corresponds to the δ function between the interstimulus interval Δ. In terms of the neural response specified for an event $u_i^2(s,t)$, it is mainly for single responses in addition to H_i (t), which stands for HRF. With this approach, the brain region views itself as a node, along with each brain cortex that has been normalized, and it receives the voxel time-course signal as it relates to a region of the brain as a voxel time-series signal. First, for every subject, time series signal extraction is performed, and then one makes use of these sensory data to produce correlation matrices. However, the connection of the voxels achieves its desired goal. Neuronal visualization of neuronal activation can be seen using its corresponding fMRI image to the sensory image of the vector $3D\ \Psi \to \mathbb{R}^{(D)}$. Convolutional modeling HRF (triggered by events) represented by $H_i(t)$ improves the maximum amplitude of the signal $BOLD$. From the HRF time series $H_i(t)$, both cerebral and sensory stimulation $v_i(t)$ and the hemodynamic modulating function $(HDMF)$ $a_i(t)$ could be summarized into two delays and dispersions to scale the signal.

$$\int_{-\infty}^{\infty} a_i(t)dt \tag{3.5}$$

A time series that displays neural activity, 32504 voxels, is seen in our research from the $fMRI$ images. Under the conditions of viewing movies, these voxels are actively involved. The distinct features of the $BOLD$ signal, which fluctuates throughout all tasks in the active region, have been given by two gamma functions of HRF Γ (.) along with the regression parameters. The time-dependent HRF conducts properly with the canonical $H(t)$ which is presented as:

$$H(t) = \frac{p_1^{\alpha_1} t^{\alpha_1 - 1} \exp^{-\beta_1} t}{\Gamma(\alpha_1)} - \frac{p_2^{\alpha_2} t^{\alpha_2 - 1} \exp^{-\beta_2} t}{\Gamma(\alpha_2)} \tag{3.6}$$

(c) **HRF to Neural Activity**

Consider the voxel $p_{i,j}$ at time t and its time series defined as $p_{i,j} = p_{i,1}, p_{i,2} \ldots p_{i,n}$; estimate the number of scans n in the period between $t_0 \ldots t_n$.$(n = 168)$, Θ_i indicates the stimulation level in the voxel i^{th} and the neuronal response $u_i^2(s,t) \in R^{n \times m}$ is convolved $[H_i(t)]_{n \times 1}$, the signal matrix for neuronal activity $u_i^2(s,t)$ has $n \times m$. Considering the convolution model of a signal, it has a partially symmetric Toeplitz structure; therefore, the resulting matrix arrangement is used as:

$$\left[u_i^2(s,t)\right] = \begin{bmatrix} u_0^2(s,t) & u_{-1}^2(s,t) & \ldots 0 \\ u_1^2(s,t) & u_0^2(s,t) & \ldots 0 \\ \vdots & \vdots & \ddots \\ u_n^2(s,t) & u_{n-1}^2(s,t) & \ldots u_{n-j+1}^2(s,t) \end{bmatrix}$$

Regressors are used to analyze time series, and one of the most popular linear models uses linear regression. Linear regression or correlation is used to determine the weights. We choose and apply a straight line $y = \beta_0 + \beta_1 x + \epsilon_i(t)$ to the seed signal.

(d) **Correlation between voxel**

Voxel time series and seed voxel are correlated and, nonetheless, a widely distributed correlation coefficient is bivariate throughout the entire range of values; as a result,

the Fisher z-transformation was applied to the correlation coefficient. It has an impact on the absolute correlation coefficient. z-transformation is likely to change the correlation.

Algorithm 1: Proposed algorithm for the BOLD signal

Input : Neuronal activities in the brain : $\Psi \rightarrow \mathbb{R}^N$, BOLD signal: $u_i^2(s,t) \in R^{n \times m}$, Activation level of voxel: $p_{i,j}$, Number of scan: n, Observed hemodynamic response: m, zero mean voxel signal: d

Output: Time series of task activated voxel

```
1  i=1
2  for j ← 1 to n do
3      p_{i,j} ∈R^{n×1}
4      Q(Ψ, p_{i,j}) ≡ {d-u_i(s,t)Ψ}^2 ; Ω = constant
5      for i ← 1 to n do
6          e_i − [ ]
7          y_i = [ ]
8          Ω_i = [ ]
9          for t ← 0 to m do
10             e_i(t) ~ N(0,c)
11             y_i(t) = Ω_i{s(t) + h(t)} + e_i(t)
12         end for
13         if d = 0 and σ_d^2 = E | d | then
14             {u_{i,j}(s,t)}_{1×D}
15             Cov {Q_u} = E u_i^T(s,t).u_i(s,t) > 0
16             z = aTanh {Cov {Q_u}
17         end if
18         k = arg min {ψ}
19         if v(i) = 0 then
20             d(i) = u_i(s,t)k + v(i)
21             {d(i), u_i(s,t)}
22         end if
23         p_{i,j} = u_i^2(s,t)
24     end for
25 end for
```

(e) Voxel-based Linear Regression Evaluation

It is carried out with $3D$ ROI node connectivity in which the seed signals are found in the activity. Fluctuations within the seed signal were evaluated for each task

condition related to the fMRI data. $BOLD$ responses across ROI from various cortical regions were specifically extracted from the defined $ROIs$ regions in which $TR = 1\ Second$ where the size of each observed voxel is $(4 \times 4 \times 4)mm^3$. Each spatiotemporal $4D - fMRI$ image dimension is $(50 \times 59 \times 50 \times 168)$ is uniformly scaled.

(f) **Evaluation of the ROI**

A signal-related value is associated with the voxel. In a group of voxels that become functionally coherent during brain activity, the functional ROI usually relies on data and exploration in order to find the voxels, then the responses from these voxels are analyzed. Using a number of $ROIs$ together with certain statistical analyses of the region. The $fMRI$ resolution takes advantage of each voxel's statistical relevance. Based on specific discriminatory standards to reduce the dimensions. Applying Fisher's linear discriminant, which suggests a significant dimension, the criterion is described as follows:

$$F(w) = \frac{\mu_1 - \mu_2}{s_l^2 + s_2^2} \tag{3.7}$$

in which means and variance have been determined as follows:

$$\mu_1 = \frac{1}{N}\sum_{n \in s_l}^{n} x_n \ \ and \ \ \mu_2 = \frac{1}{N}\sum_{n \in s_2}^{n} x_n \tag{3.8}$$

$$s^2 = \sum_{n \in s_k} (y_n - \mu_k)^2; \ \ y_n = w^T x_n \tag{3.9}$$

In Eq. 3.7 which expresses the data using the vector w, for the input of a certain number of distinct points belonging to class s. $fMRI$ data gets processed using data-driven techniques that employ cerebral spinal fluid CSF that has been extracted with white matter signals WM. Gray matter GM covers the cerebral surface.

3.2.2 Edge Detection and Similarity Measurement

The essential algorithmic feature that needs to be modified for each of these techniques associated with the intensity of the image. Rorden et al. [245] recommended the second derivative ($Gaussian$) for spatial scale of interest for medical images which describe the efficiency and visual quality. To improve edge recognition within MRI images containing brain tumors, an 8-directional template with sobel algorithm was used by AS and Gopalan [246]. Yunhong et al. [247] apply the canny operator for complete edge detection to optimize the parameter of MRI image for training output of artificial neural network. The ROI might be implicitly determined, and task-based $fMRI$ certainly has some limitations. It is possible to acquire ROI, and this is a standard method to find edges. The ROI method can enhance the statistical efficacy derived from any random gradient histogram. Images change as a result of edge detection, which involves sudden changes in intensity; it is a method for finding and recognizing intensities.

(I) **Laplacian Edge Detection:** Considering the edge detection technique, this approach is probably the most appreciated.In order, the significance of the pixel intensity $I(x, y)$ Laplacian of I is: $\Delta I = \nabla^2 I = \nabla\dot{\nabla} I$ where $\nabla = \frac{\partial}{\partial x_1} \dots \frac{\partial}{\partial x_n}$

$$\Delta I = \sum_{i=1}^{n} \frac{\partial^2 I}{\partial x^2} \tag{3.10}$$

The Laplace operator has been employed here and performs the edge detection with *OpenCV*. They were able to obtain the edges on MRI images.

(II) **Discreet Differentiation Operator:** This operator performs edge extraction in MRI images that contain brain disease, that is, acute cerebral infarction. The components are linked for a spatial gradient $2D$ to the transverse region, since the vertical orientations of the individual pixels that result in the image are encoded on the x and y axes; therefore, the characteristic of the image is represented by a function $f(x, y)$ as:

$$\frac{\partial f}{\partial x} = f(x+1, y) - f(x-1, y) \tag{3.11}$$

$$\frac{\partial f}{\partial y} = f(x, y+1) - f(x, y-1) \tag{3.12}$$

according to the above illustration, the descent of MRI image is described as $(n \times n)$ $2D$ vectors, specifically. $\nabla f(x, y) = g_x + g_y$, particularly $g(x, y) = \sqrt{(g_{x^2} + g_{y^2})}$ furthermore, the convolution kernel (3×3) represented as:

$$T_x = \begin{bmatrix} -1 & 0 & 1 \\ -2 & 0 & 2 \\ -1 & 0 & 1 \end{bmatrix} \quad T_y = \begin{bmatrix} -1 & 2 & -1 \\ 0 & 0 & 0 \\ 1 & 2 & 1 \end{bmatrix}$$

In order to obtain the edges of an acute cerebral MRI image, T_x and T_y are horizontal and vertical operators, respectively.

(III) **First-order Differential Operator:** An operator to calculate the gradient between eight pixels of the images MRI, which divides each pixel evenly. As a result, it produces the approximate gradient in rows and columns, which is determined as:

$$P_x = \begin{bmatrix} -1 & 0 & 1 \\ -1 & 0 & 1 \\ -1 & 0 & 1 \end{bmatrix} \quad P_y = \begin{bmatrix} -1 & -1 & -1 \\ 0 & 0 & 0 \\ 1 & 1 & 1 \end{bmatrix}$$

The overall structure and brightness of the MRI image are altered by the gradient since the gradient varies in each direction. The histogram of the Oriented Gradient (HOG) method extracts the gradient perspective.

3.2.3 BOLD signal indicating neural activation

After preprocessing the response $BOLD$ using the data $fMRI$, the voxels were used for additional analysis. For the relevant region of the cerebral cortex, the corresponding signal intensities $BOLD$ are currently determined, which are based on the data $fMRI$ with $TR = 1.0$ and $slice = 50$. In each of the active voxels, the $fMRI$ time course was retrieved to provide the data for CNN. Task-related $fMRI$ voxel time series has affected the relationship of the signal with the baseline signal $BOLD$. The detection of cognitive and neurological activity characteristics, which is based on fMRI data, uses seed-based correlation. To achieve actions throughout the different regions of the brain, it also defines the development of temporal action within the brain. The size of its correlation matrix

(19, 19) for every subject and the fact that it depicts the 19 parts of the brain among which CSF indicates stimuli and has been identified as physiological noise and makes use of linear regression increases the specificity FC'.

(I) **Functional Connectivity for Neurodevelopmental fMRI:** The intensities of the voxel $fMRI$ describe fluctuations in local concentration in neural stimulation; these are the hemodynamic responses of the voxel. The intensities are extracted from the voxel, which evolves over time. Sharp fluctuations occur in the signals. The stimulus is presented every two seconds, with $TR = 1$ second. Consider an expected response $BOLD$ $a_i(t)$ resulting from neuronal activity; $v_i(t)$ represents the signal of BOLD activity within each outcome with a linear time-invariant (LTI). Therefore, brain activity and HRF $h_i(t)$ interact together, which is possibly defined as: $h_i(t) = v_i(t) \otimes a_i(t) + \epsilon(t)$ where $\epsilon(t)$ is deduced to exist in $N(0, \sigma^2)$ and σ^2 represents noise.

(II) **Seed-Based Connectivity in Neurodevelopmental fMRI:** This approach produced a time series and a spatial map of $fMRI$ images. The selected voxel surrounded by specific ROI, as well as other voxels, has a correlation with its $BOLD$ signal in ROI. Using task-based $fMRI$, time series extraction is performed for all voxels within a seed region. The correlation across time series is used to measure connectivity with respect to the time series and the a priori seed of the remaining voxels. The connection between voxels that are close to each other in space is made using a time series $BOLD$ that is evaluated between voxels while the stimulus is present. This generates a regional network, including the seed voxel, in which the seed time series is extracted.

(III) **Seed Based Procedure for CNN:** The region inside the brain is described as a node, and every region of the brain's normalized time-series signal comes from each voxel. Time series signals extracted from all activated voxels are used as input to CNN. The overlapped brain mask covers the entire volume, where the total number of voxels is 32504, and the structure of the overall mean time series, including the seed voxel time series, is 168×1. The precision achieved by $2D-CNN$ is affected by the choice of seed.

3.3 Transformation of 4D-fMRI

3D whole-brain volumes sequentially represented by $4D-fMRI$ images are observed for data completeness over various successive time points. A 4D tensor containing 3D space $\times$ time is generated from an fMRI dataset. Tensors contain correlation data.Observing $4D-fMRI$ images which analyze correlations that are spatiotemporal.

Processing of $4D-fMRI$ data is very challenging due to the enormous amount of data. Voxels describe the characteristics, including their correlation in the $4D-fMRI$ data. When $fMRI$ images are pre-processed, the $ADHD$ $fMRI$ data have been cleaned of a number of confounding factors. In RSN masking on insignificant data is performed for the purposes of assessments. $3D-fMRI$ maps containing t statistics have been generated as a test in which ($p < 0.05$) with the 85 voxel cluster, resulting in the dimension of the voxel header ($53 \times 63 \times 46$) for 28 RSN in addition to a time interval of 1.0s. Each voxel in the MNI space has been estimated to have $(3 \times 3 \times 3) - mm^3$ spatial resolution. The $4D-fMRI$ image input to the $LSTM$ models is represented as $[x_1, x_2, x_3, \ldots, x_n]$ and demonstrates a series of $4D$ frames. where the corresponding index (I) can be used to

express each $4D - fMRI$ image & transformed into $3D$ EPI.

$$F \in \mathbb{R}^{|I| \times m}$$

$$V \in \mathbb{R}^{n \times m}$$

$rs-fMRI$ feature vector that has been reshaped which can be expressed in the following matrix:

$$V = \begin{bmatrix} I_{x_1} \\ I_{x_2} \\ I_{x_3} \\ \vdots \\ I_{x_n} \end{bmatrix}$$

3.3.1 Application of Tensor to Reshape rs-fMRI Data

The reshaping process for $4D - fMRI$ image time series $4D$ data array $(x \times y \times z \times t)$ is transformed into a series of $2D$ data arrays. This specific reshaping procedure is illustrated as follows.

- *Step-1:* The trilinear structure of the $rs-fMRI$ data is denoted by $(D \times V \times S \times N)$ D-DMN at time T points for V-voxels in S- slices.

- *Step-2:* Apply the algorithm $PARAFAC$ to determine the value of V, S and N with components a_{ir}, b_{jr} and c_{kr} using the trilinear model according to:

$$x_{ijk} = (a_{i1}b_{j1}c_{k1} + a_{i2}b_{j2}c_{k2} + \cdots + a_{ir}b_{jr}c_{kr} + \cdots + a_{iR}b_{jR}c_{kR}) + e_{ijk}$$

Where, x_{ijk} represents the input within a $3D$ data array X, and e_{ijk} indicates an error.

- *Step-3:* Signifies the tensor product X which provides linear independence for a signal. The generalization of X could be described as follows:

$$X = \sum_{r=1}^{R} a_r \otimes b_r \otimes c_r$$

In this instance, the total matrix of components is R, especially the signal matrix which is referred to as the entire ranks, since the data array $V \times S \times N$; a_r contains a vector having dimensions in V; b_r is the vector that has dimensions in S, and c_r containing a vector with dimensions N.

- *Step-4:* Specifies three vectors a_r, b_r, and c_r representing spatial components that use r dimensions. in which $a_r \in R^V$, $b_r \in R^S$, and $c_r \in R^N$ through the $V \times S \times N$ three-dimensional data array. Furthermore, the signal matrix X becomes a series of $2D$ data that is composed of voxels $V^{(v)}$ for the element v^{th} in the time period of the slice $\{s(t)\}$ within $\{N\}_{i=1}^{n}$ RSN having linear independence.

- *Step-5:* Assume that a $y_i = t \times v$ is the matrix that evaluates the $fMRI$ data matrix obtained through (i^{th}) RSN.

- *Step-6:* Concatenates each RSN data set and produces a matrix of $fMRI$ data array $g = nt \times v$.

- *Step-7:* The spatially independent component p generates the matrix $p \times v$. Based on $2D$ data matrix $nt \times v$ including an error matrix $e_i = t \times v$ correlate with i^{th}

RSN. Using $g = nt \times v$ the matrix used for mixing is $A = [a_1 a_2 \dots a_n]^T$ in which $a_i = t \times v$ considers i^{th} RSN of ($RSN28$).

- *Step-8:* Estimates a tensor of the trilinear model $a_r \otimes b_r \otimes c_r$ and $C = n \times p$ where n involves n^{th} RSN as well as p involves an independent component p^{th}. In this case p, acts as the vector of phenotype loading data, using the $rs-fMRI$ trilinear data that are represented by the use of the Kronecker product of matrices $C \otimes A$ or $KRON(C, A) = [CA]^T$is the essential idea.

$$C \otimes A = [C_1 A^T C_2 A^T \dots C_m A^T]^T$$
$$- [C_1 A_1 \dots C_1 A_n, C_2 A_1 \dots C_m A_n]^T$$

- *Step-9:* Apply Khatri-Rao product: $C \otimes A$=$C \odot A$ considering that every single pairwise Kronecker product is a mix of the column of input matrices.

- *Step-10:* Vectorized, the primary diagonal of the matrix is given by $C \odot A = (C \otimes A)A^T$, where $C \odot A$= $[C_1 \otimes A_1 \dots C_n \otimes A_n]$using the diagonal matrix D also the vector d with diagonals $D = Diag(d)$ in addition to $d = Diag(D)$ are commutative.

The proposed procedure for reshaping the $4D-fMRI$ image is demonstrated in Figure. 3.4in which the reshaped data matrix is considered a feature vector (V) with a pre-trained data value for the $LSTM$ architecture, and the model classifies the data $rs-fMRI$ between healthy subjects and $ADHD$. Our work has been centered around a binary classification methodology that aims to obtain the variable y_i that only takes two values, that is, 0 and 1. y_i is used to estimate the precision of subjects with $ADHD$ and

healthy, and x_i as input feature of the image $fMRI$. Therefore, pair (x_i, y_i) has been taken into account as a training pair. It comprises each subject's RSN and re-shaped $fMRI$ image data array.

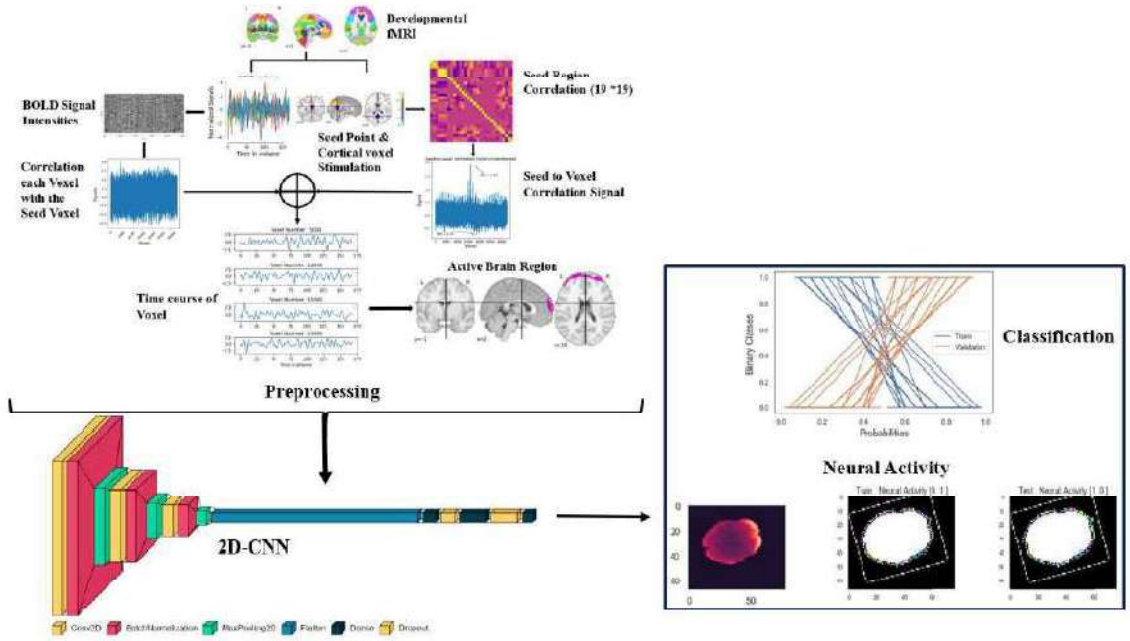

Figure 3.1: Proposed 2D CNN framework for classification brain activity

3.4 Proposed 2D-CNN Architecture

The $2D - CNN$ model for FC data, while $2D$ kernels are used, might produce the characteristics of time series data. $fMRI$ image data are applied in the CNN model, and three convolution layers are also included. It is distributed with batch normalization; maximum-pooling is put first, then the fully connected layer. The seed-to-voxel connection of a region of the brain serves as input data for the convolutional layer. The image $2D - fMRI$ must pass through a 3D array while fitting a data set; ideally, that would be $(height \times width \times channels)$. Displays the information of each layer in Table 3.1.

- ***Input Layer:*** In this input layer, it takes functional connectivity from the data

$2D$ as input. In this specific case. the original measurement for the input image dimension $fMRI$ is $[67 \times 77 \times 3]$.

- ***Convolution Layer:***Using this layer as an instance $Conv(f, k, a)$, where there are f filters determining how many filters are used for feature maps, and the size of the kernel is indicated by $k = (3, 3)$. There are three convolutional layers in this model and each convolutional layer uses batch normalization. 32 output channels are present in the first convolutional layer. The next layer has 64 output channels, and 128 output channels are present in the third layer. The resultant non-linear activation function uses a non-linear function $ReLU$ with a learning parameter of 0.1.

- ***Batch Normalization:*** It allows a higher rate of learning. At first, this layer is used that normalizes the data and influences the performance of $ReLU's$ by reducing the mean of the batch μ then the division is performed through the standard deviation σ effectively minimizing the loss of data between hidden layers.

- ***Max Pooling Layer:*** In this layer the input volume provided was pooled in this particular layer with dimension $[65 \times 75 \times 32]$ and the filter $dimension = (33)$ implemented with $stride = 1$ producing the output dimension $[32 \times 37 \times 32]$ after downsampling. This $2D - CNN$ approach also has a learnable hyperparameter and contains three $2D$ convolutional layers. The three convolutional layers extract the characteristic with the initial dimension of the $fMRI$ image as $[67 \times 77 \times 3]$, after which a $ReLU$ activation function is applied.

- ***Flatten Layer:*** This layer transforms the entire aggregated feature map matrix $3D$ into a vector $1D$ using the subsequent Max pool layer, which includes the convolution

Table 3.1: **2D-CNN Architecture for the Classification of Neural Activity**

Operation	**Kernel Size**	**Data Dimension**	**Weights (N)**	**Weights (%)**
Input Layer	(3×3)	[67×77×3]	-	-
Conv2D Layer	(3×3)	[65×75×32]	896	0.10%
ReLU	(3×3)	[65×75×32]		
Batch Normalization	(3×3)	[65×75×32]	128	0.00%
Max Pooling Layer	(3×3)	[32×37×32]	0	
Conv2D Layer	(3×3)	[30×35×64]	18496	1.20%
ReLU	(3×3)	[30×35×64]		
Batch Normalization	(3×3)	[30×35×64]	256	0.00%
Max Pooling Layer	(3×3)	[15×17×64]	0	
Conv2D Layer	(3×3)	[13×15×128]	73856	4.60%
ReLU	(3×3)	[13×15×128]		
Batch Normalization	(3×3)	[13×15×128]	512	0.00%
Max Pooling Layer	(3×3)	[6×7×128]	0	
Flatten Layer	-	5376		
Dense Layer	-	256	1376512	85.9%
ReLU	-	256		
Dropout	-	256	0	0.00%
Dense Layer	-	512	131584	8.20%
ReLU	-	512		
Dropout	-	512	0	0.00%
Dense Layer	-	2	1026	0.10%
Softmax	-	2		

sequence. It is followed by fitting the input to a dense layer in order to classify.

- ***Fully Connected Layer:*** $1D$ vector linking to fully connected layers from a flat layer in which all inputs and all outputs are connected through the learnable weight parameter accompanied by the activation function $ReLU$. For the pre-trained model, there are an additional three dense layers. The first dense layer has 256 neurons, while the next dense layer has 512 neurons, including the activation function $ReLU$.

- ***Classification Scheme:*** The method to classify the fMRI response is implemented in the final segment of the CNN model; this part of CNN classifies neural activity and there is no neural activation. This model includes a fully connected layer with the goal of having 512 neurons accompanied by the activation function $ReLU$. There are two neurons in the output layer and a Softmax activation function, which gives the output probabilities for both classes in binary classification with respect to the image $fMRI$.

3.5 Saliency Map for MRI Visualization

At this point, we continue with our visualization work, in which we apply a regularization technique to bias the images, which are identified by optimization as complex-valued moving MRI images that are easier to interpret visually. The use of MRI allows the indirect measurement of various region-specific lesions and the formation of three-dimensional representations in the human brain.

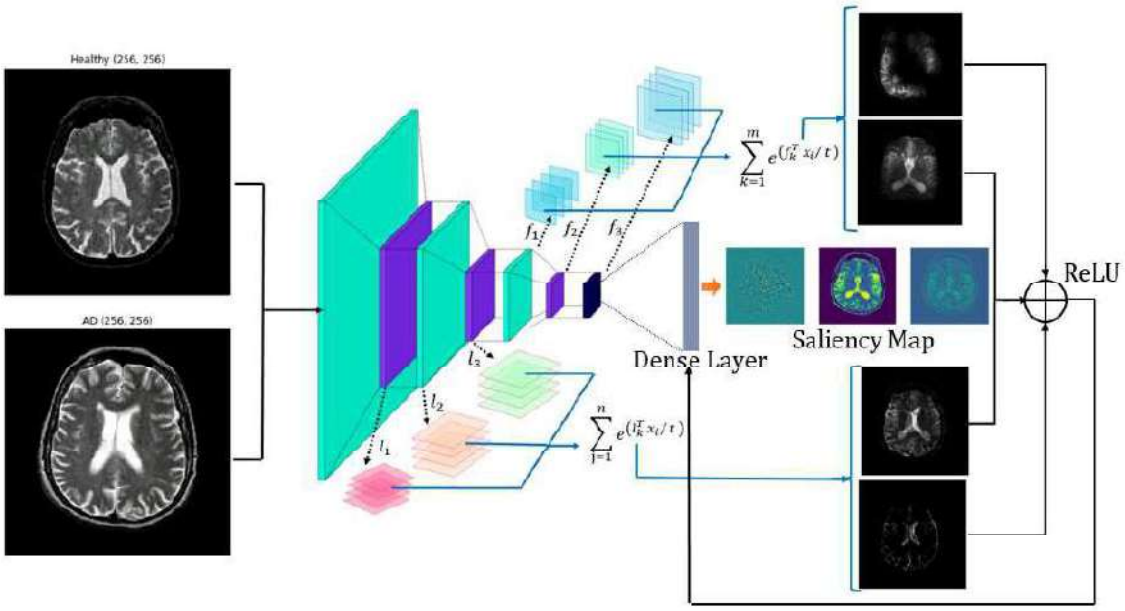

Figure 3.2: Schematic 2D-CNN framework for the saliency map generation of T1-weighted Healthy and AD MRI image, which states the modified contrast image slices.

3.5.1 Using the Saliency Map to Interpret MRI image

An input image $3D - MRI$ of size $\{I = x_i \in R^{II \times W \times C} \rightarrow R^d\}$. Based on d-dimensional vector information with 227 pixels for each of the height (H) width (W) and number of feature channels $C = 3$, it subsequently combines spatial data from each input image MRI to $x_i \in R^d$. The input image MRI is denoted by x_i of the class $C_i \in [0, 1]$ class, the corresponding probability p_i of the MRI image x_i identified as the class c_i may have been determined using the softmax function for each component $l_1 l_2 \ldots l_n \in \mathcal{L}$ and characteristic of the characteristic $f_1 f_2 \ldots f_n \in \mathcal{F}$ in 3D lookup tables $\mathcal{L}$ in addition to the characteristic cue $\mathcal{F}$ in terms of the smoothing measure at temperature t is determined as follows:

$$p_i = \frac{e^{(l_i^T x_i/t)}}{\sum_{j=1}^{n} e^{(l_j^T x_i/t)} + e^{(l_k^T x_i/t)}} \tag{3.13}$$

The monotone function that is Log then determines an argmax from the logarithm of likelihood (LL), and, subsequently, it has to match a (LL) argmax. To maximize the probability of p_i, one of our objectives is to choose c_i.

$$LL = \sum_{i=1}^{n} \log p_i^{x_i} [1 - p_i^{(1-x_i)}] \tag{3.14}$$

the measurement for the $\mathfrak{L}_2$ using normalized input MRI image vector $x_i \in R^d$

$$\|x_2\| = \sum_i (|x_i|^2)^{\frac{1}{2}} \tag{3.15}$$

within factor $1 + \varepsilon$ in which ε is a minimal positive value. Subsequent to forward propagation, the prototype value l_n is modified together with a momentum η.

$$l_n \leftarrow \eta l_n + x_i(1 - \eta) \tag{3.16}$$

The softmax classifier evaluates probability distributions to establish objective functions that will be used to train the proposed network. When an efficient softmax and cross-entropy loss are applied together, this is frequently applied for training the deep learning framework when implementing multinomial logistic regression. These loss functions in the context of x_i are all updated in a specific manner, l_n as a result of incorporating the softmax function. With respect to x_i, the partial derivative is represented as:

$$\frac{\partial p_i^{x_i}}{\partial x} = \begin{cases} p_i^{x_i}(1 - p_i)^{(1-x_i)}, & for\ i = j. \\ -p_i^{x_i}, & otherwise. \end{cases} \tag{3.17}$$

Following these features, $(f_1 f_2 \dots f_n)$ is provided in the expression prediction framework to train the MRI image by reducing this loss function. It produces a probability vector $p_i \in R^{C_i}$ as its output results in the use of the softmax function.

3.5.2 Generation of Saliency Maps Using the Region

Architecture for the region-based saliency technique ($XRAI$) in addition to the Integrated Guided Gradient (GIG). The basic premise of Integrated Gradient (IG) occurs when some non-linear differentiable function is defined by χ:

$$R^{C_i} : C_i \longrightarrow [0, 1] \tag{3.18}$$

$$x \longrightarrow C_i(x) \tag{3.19}$$

The attribution vector are represented as $v = (v_1, v_2..., v_n)$ is used to masked the data provided by the MRI image x for the purpose of displaying the ROI for the specified predicted score. These data are obtained from ROI for an MRI image slice:

$$IntGrad(x - x_i) = \int_0^1 \frac{x_i + \alpha(x - x_i)}{\partial x} d\alpha$$

In the above equation, the difference between the input MRI image and the output MRI image is denoted by $x - x_i$ for every pixel.

3.6 Proposed BLSTM model for ADHD classification

Taking into account the above, a $LSTM$ layer is part of the $BLSTM$ classification framework that takes into account the $2D$ size of 261×20 the input vector. Consequently,

$BLSTM$ encompasses the advantages of long-term memory-based bidirectional processing. Within the proposed model, there are three bidirectional $LSTM$ layers and a $ReLU$ activation function among all the hidden layers. Each layer possesses an LSTM hidden layer in the forward and backward directions, as well as a dropout layer with a dense layer, as shown in Figure. 3.3. The reshaped data are fed into our proposed $BLSTM$ model, which further processes the stream of data corresponding to both directions, that is, forward and backward $LSTM$ layers. The processed data $rs - fMRI$ are combined in a dense layer and then used by the layer $Softmax$ to classify the healthy and $ADHD$ subjects and produce the normalized probabilities for each class. Generally, the $Softmax$ classifier enables and deals with the labels $y_i \in \{0, 1\}$ where $i \in \{1 \dots N\}$ and N classes. For the training data set labeled m $fMRI$ $\{(x_1, y_1) \dots (x_m, y_m)\}$ in two-class classification $n \in \{N = 2\}$. The hypothesis $h_\alpha(x)$ is applied to normalize the probabilities distribution $P(y = \frac{n}{x})$ for the test set of $fMRI$ $\{x\}$ it is determined as:

$$h_\alpha(x) = \frac{1}{\sum_{j=1}^{N} exp(\alpha^{(j)T} x)} \tag{3.20}$$

$$P\Big(y_i = n/x_i; \alpha\Big) = \frac{exp(\alpha^{(n)T} x_i)}{\sum_{j=1}^{N} exp(\alpha^{(j)T} x_i)} \tag{3.21}$$

The dense layer applies the Binary Softmax Classification yields the necessary results.

3.6.1 Experimental Setup

For experiments, a step-by-step approach has been defined and uses $LSTM$ models to classify brain diseases. The proposed model $BLSTM$ is based on functional and time-dependent data $fMRI$ in which the time stamp predicts the time series $rs - fMRI$.

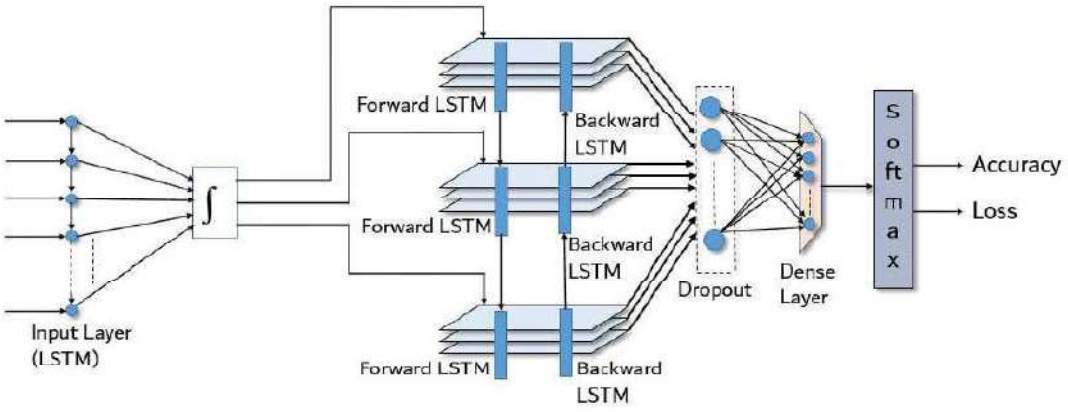

Figure 3.3: Proposed model of a BLSTM layered perspective for rs-fMRI

Moreover, to classify brain diseases, the spatial as well as temporal $fMRI$ data array is used in the development of the $LSTM$ framework for classification. Spatial parameters determine the feature weight by using Eq 1.1 and Eq 1.2 for evaluating the pattern of connectivity of every brain area. The following steps are used to discuss the different portions of Figure. 3.4:

- *Step-1:* The input feature vector of several $rs-fMRI$ images is acquired from the $4D-fMRI$ image and processed as $(3D+t)$ data. It is considered as $3D-fMRI$ data with the timestamp t.

- *Step-2:* Masking has been performed on $3D-fMRI$ images that allows $fMRI$ data to be revealed in a long $1D$ data array. Applied the reshaping procedure which is defined in subsection: 3.3.1 on the $rs-fMRI$ images. One feature vector of each voxel time series $rs-fMRI$ image data is arranged in the matrix for further processing and analysis.

- *Step-3:*In this instance, the resultant matrix appears to be $(S \times W)$, where S scans are being performed in (t) seconds and (W) the total voxels in every scan. Discovered $ADHD$ time series data A_i (t) at voxel (i) at a given moment (t). Therefore, the

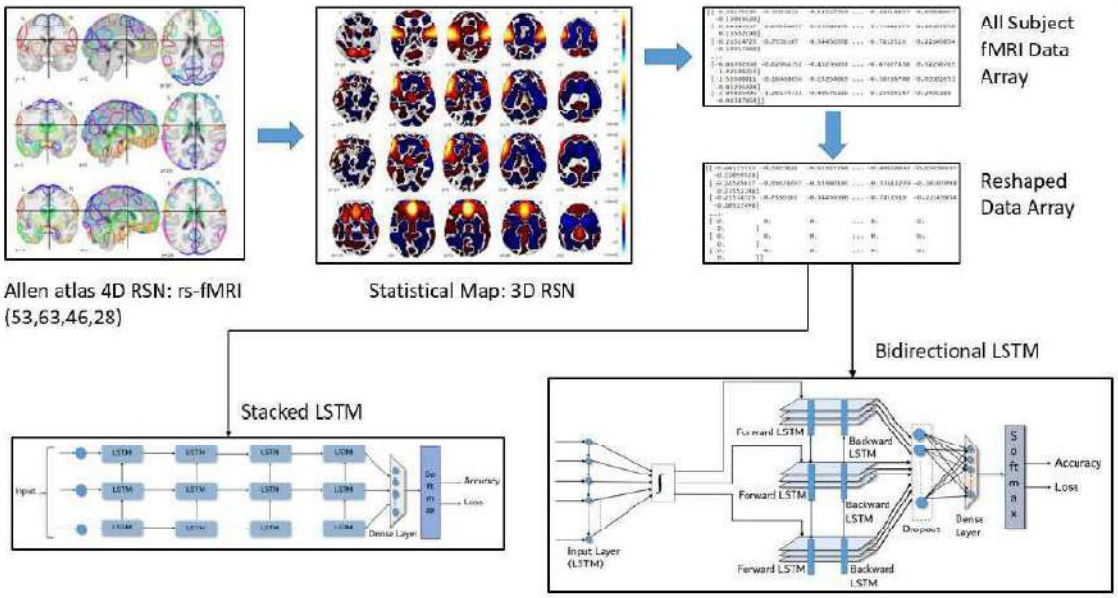

Figure 3.4: Model and accuracy. $4D$ Nifti datasets of rs-fMRI data using stacked LSTM and the proposed model to learn the initial state of RSN28 then changes into its constituent volume $3D$ with statistical map. Convert $3D$ voxels to a data set using Numpy and reshape the data set of all patients with ADHD and subjects without ADHD. The LSTM and the proposed model package the input to measure the precision and loss of 32 training data and 8 test data on 50 epochs.

$fMRI$ images can be stated as follows:

$$A - [a_1, a_2, a_3, \ldots, a_t]^T \tag{3.22}$$

- *Step-4:* The resultant output using stacked $LSTM$ recurring memory cells and the proposed updated model $BLSTM$ according to the following steps:

  (i) $BLSTM$ model's cell component structure of the $BLSTM$ model works as the subsequent $LSTM$ layer, and the entire cell internally uses two activation functions such as *sigmoid* and tanh. Furthermore, the three hidden layers in the model $BLSTM$ maintain the input weights 30%, 34.2% and 24.3% respectively, having a dropout of 0. 5%, furthermore a recurrent dropout of 0.20% for each weight $LSTM$ and finally a dense layer using a $Softmax$ activation

function which predicts the $ADHD$ classification as shown in Figure. 3.4.

(ii) Secondly, the $Softmax$ activation function of the stacked $LSTM$ processes the output. The functional network serves as the first $LSTM$ layer that takes the input feature. The hidden state layer receives input from the first hidden layer. Finally, the second hidden layer passes the output to the third hidden layer and delivers significant accuracy.

3.6.2 Training strategy for BLSTM model

The $BLSTM$ model is used to get access and effectively learn the rs-fMRI time series through forward and backward LSTM for each small duration.

$$ForwardLSTM : \overrightarrow{A} = \overrightarrow{BLSTM_3}(\overrightarrow{BLSTM_2}(\overrightarrow{BLSTM_1}(x)))$$

$$BackwardLSTM : \overleftarrow{A} = \overleftarrow{BLSTM_3}(\overleftarrow{BLSTM_2}(\overleftarrow{BLSTM_1}(x)))$$

But in both directions, either forward or backward, $BLSTM$ encodes only half of the sequences over various intervals. Therefore, the modified $BLSTM$ model captures the previous and subsequent feature sequences obtained from the $rs - fMRI$ images, as demonstrated in Figure. 3.4 for each time step. Six identical $LSTM$ cells (three in both directions) are arranged in a stack to represent the three layers of representation. To test and train the modified $BLSTM$ model. The $BLSTM$ model is a combination of a 3 hidden layer along with a $1D$ dropout layer, with a probability of 0.5 to avoid possible overfitting along with a fully connected layer. $ADAM$ optimizer is used to train the $BLSTM$ network in order to optimize the "cross-entropy" loss function. The learning rate has been set to lr to 0.1 and then began to decrease with each update. For every

training epoch, the weights are regularly updated. In each iteration, we have used one epoch, which affects the convergence time and the loss of validation of the data after 50 epochs have passed, which serves as the basis for the stopping criterion to establish the learning of the proposed model.

3.7 Deep Learning Model for MS Classification

In this section, we have described the proposed model for the detection and classification of MS lesions, as shown in Figure. 3.5. The proposed model consists of three modules: image pre-processing, MobileNet, and 2D-CNN. The detailed functioning of these modules is discussed in the following subsections. The architecture of the baseline convolutional neural network $MobileNet$ is used for the initial stage of data set training. The $MobileNet$ contains a stack of layers that consists of four blocks named the (i) Convolutional Layer. (ii) Batch Normalization (iii) Depthwise convolutional layer, followed by (iv) Global Average Pooling (GAP) layer. Using $MobileNet$ to classify natural images is not similar to the numerical data array, so more convolutional blocks are required for proper tuning of the brain image dataset MRI.

3.7.1 MRI Pre-processing

Here, we apply various preprocessing steps, such as cropping, resizing, and augmentation, to the MRI images before feeding them into the $MobileNet \quad 2D \quad CNNmodel$. These preprocessing steps are discussed below.

(I) **Cropping and Resizing:** Due to the computational task and the limitation of fitting a complete MRI image into the model, we reduce the size of the brain image

from $(256 \times 256 \times 3)$ to $(131 \times 176 \times 3)$. We have worked with the data-driven strategy and have performed cropping on the MRI images to remove unwanted regions.

- Edge detection: To compute the gradient magnitude of the brain image, we have applied the Sobel edge detection method to obtain the minimum and maximum gradients inside and at the edges of the various MRI images as shown in Figure. 3.5.
- *Thresholding:* Once the edge is detected, we perform the thresholding that divides the pixels in the grayscale image and converts the scans MRI into binary images Oliva et al. [244].
- *Filtering:* Further, filtering uses the Sobel filter and removes the noise of low frequencies from the MRI images.
- *Segmentation and Contour:* Here, we apply a watershed algorithm to the filtered image to extract the segmented regions by finding watershed linesBeare et al. [238]. Choosing the largest contour of the watershed transformed the image and applied a grayscale to convert it into binary images.

(II) **Image Augmentation:** The image enhancement strategy that the network will use for more training data also reduces the overfitting of the proposed model. Image augmentation comes from transformation, color space, random cropping, orientation, mixing images, kernel filters, etc. The classification accuracy of the Deep Learning model performs much better in the augmented test data set Shorten and Khoshgoftaar [248]. We have performed data augmentation on MRI images, using the *ImageDataGenerator* API from *Keras* inside the *Tensorflow 2.5* before we feed

into the *MobileNet* network. The enhancement of images includes factors such as rotation, shifting, shearing, horizontal flip, vertical flip, and brightness that generate the new training data set as shown in Figure 3.5. The augmentation operation is performed by random rotation by 45^0 and then applies to shifting, shearing with the rotated images, and applying horizontal and vertical flipping of the transformed image. Finally, resize the *MRI* images, which correspond to the input size of the baseline model, that is, (224 × 224) pixels.

3.7.2 BaseLine MobileNet with 2D-CNN

The *MobileNet* network we implemented with acquired sample values and output characteristics from the baseline model fed into the $2D - CNN$ network, which is shown in Figure. 3.5 The baseline model is based on a depth-wise separable filter and performs a single convolution for each input channel. For the target network, by adding one convolution layer followed by one maximum sharing layer and two fully connected layers of size 256 and 2, the dropout is 0.5% and we have used the root mean square propagation optimizer *RMSprop* to train the model with a learning rate of 0.0001. Here, *RMSprop* performs the simulated annealing while adjusting the learning rate and optimizer, which are defined according to the following equation:

$$E[g^2]_t = 0.9E[g^2]_{t-1} + 0.1g_t^2 \tag{3.23}$$

$$\theta_{t+1} = \theta_t + \frac{\eta}{\sqrt{E[g^2]_t + \epsilon}} g_t \tag{3.24}$$

Where $E[g^2]_t$ is the running average at time t depend upon momentum $\gamma = 0.9$ and the default value of the learning rate $\eta = 0.001$ on the previous average $E[g^2]_{t-1}$, the

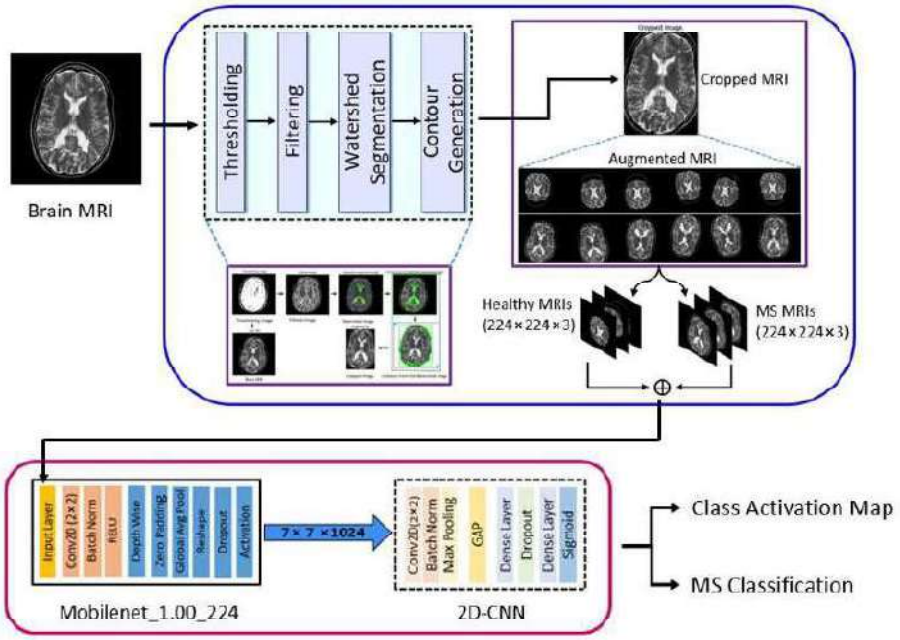

Figure 3.5: Proposed MobileNet-2D-CNN framework for the classification of Multiple Sclerosis

gradient of the objective function is denoted by g_t for the update parameter θ at every time step t.A combination of these $2D-CNN$ layers is applied along the $MobileNet$ network.The features generated from the $MobileNet$ are further fed to a shallow custom CNN architecture, as shown in Figure. 3.5. The output shape obtained from MRI image from $MobileNet$ will be input to $2D-CNN$. The proposed model is trained in 20 epochs, as we used a training and testing scheme of $80-20$.

3.7.3 Class Activation Map (CAM)

For a specific class, the class activation map with global average pooling is applied to the proposed model. These weighted activation maps are generated by the hidden layers of the MRI images.The network visualization pattern is activated by each unit of the network. CNN learns while being trained to recognize the object. The obtained features are fed into the dense layer, which is regulated by the $Softmax$ activation function and provides the

Table 3.2: Proposed Architecture of using baseline MobileNet network and 2D-CNN.

OPERATION	**DATA DIM**	**WEIGHTS(N)**
Input Layer	$224 \times 224 \times 3$	–
MobileNet_1.00_224	$7 \times 7 \times 1024$	3228864
Conv2D	$5 \times 5 \times 32$	294944
Batch Normalization	$5 \times 5 \times 32$	128
Max Pooling 2D	$1 \times 1 \times 32$	–
Global Avg Pooling 2D	32	–
Dense	–	8448
ReLU	256	–
Dropout	256	–
Dense	–	257
Sigmoid	1	–

result of the calculated probabilities for further classification. We illustrated the activation of the convolutional layer. Let us consider the activation k from the convolution layer at the location (i, j) then the activation function for the MRI image will be denoted as $f_k(i, j)$. Here, the global average pooling (GAP) at activation k is represented by G_k as shown in Equation 3.25.

$$G_k = \sum_{i,j} f_k(i, j) \tag{3.25}$$

The activation function $Softmax\ \sigma_{C_i} = \sum_k \omega_k^{C_i} G_k$ is used to calculate the probabilities of the class label C_i P_{C_i}

$$P_{C_i} = \frac{\exp(\sigma_{C_i})}{\sum_{C_i} \exp(\sigma_{C_i})} \tag{3.26}$$

$$\sigma_{C_i} = \sum_k \omega_k^{C_i} \sum_k f_k(i, j) \tag{3.27}$$

The class activation map (CAM) is obtained through the weighted feature map gov-

erned by the softmax weight σ_{C_i} that classifies the heat map corresponding to a specific class.

Visualization of Class Activation

In the input network, the input MRI image $f_k(i,j)$ with height h, width w, and depth d passes through the $MobileNet\text{–}2D-CNN$ model. Here, the input image MRI with the tensor $(h \times w)$ maps each dimension of the pixels with its color value class C_i. Furthermore, the classifier considers the input image MRI and maps it with the class saliency map $H \in \mathbb{R}^{h \times w}$ and applies the activation function G_k to each pixel of the input image $f_k(i,j)$. Furthermore, the weighted neurons are calculated as the gradient of the activation function $Softmax$ σ_{C_i} to the activation of the feature map obtained f_k for the convolutional layer, which is defined according to the following:

$$\omega_k^{C_i} = \left.\frac{\partial \sigma_{C_i}}{\partial f_k}\right|_{f_k(i,j)} \tag{3.28}$$

Taking the partial derivative of G_k w.r.t. $f_k(i,j)$ i.e.

$$\frac{1}{N} = \frac{\partial G_k}{\partial f_k(i,j)} \tag{3.29}$$

$$H = relu\left\{\sum_k \omega_k^{C_i} f_k(i,j)\right\} \tag{3.30}$$

This formulation of the computation allows us to generate the visualization of the saliency map of multiple sclerosis MRI images.

3.8 Conclusion

To summarize, the methods demonstrate the activity of $BOLD$, which responds to the brain signal based on HRF. We briefly introduce the canonical HRF model, which is made up of two gamma functions combined linearly. HRF gives details of the activation time period. The nature of $BOLD$ $fMRI$ correlations is identified as clusters of regions in the term of RSN with mutual correlation. Compared to statistical analysis based on ROI, the main advantage of using the voxelwise method is its ability to provide a spatially unbiased evaluation of brain images. A voxel has a value corresponding to the signal. Applying various types of $ROIs$ together with a specific statistical analysis of the region. The statistical importance of each voxel can be increased by the $fMRI$ resolution. CSF, WM, and GM are used in data-driven strategies to interpret the fMRI data. ROI may be calculated implicitly, and this is an essential technique to identify edges on images MRI. An ROI method is applied to determine the intensities of the signal. The fluctuation has been defined by the $fMRI$ voxel intensities in the spatial concentration of the neuronal stimulation. Seed-Based Connectivity uses a task-based $fMRI$ for $BOLD$ time series extraction, and it measures throughout all voxels as long as the stimulus is active. Apply masking to the irrelevant data in RSN for evaluation criteria and reshape the $rs-fMRI$ feature vector. $2D-fMRI$ image data require a $3D$ array to properly fit a data set. The correlation between a brain region's seed and voxels serves as the input data for the convolutional layer in the $2D-CNN$ model. The $2D-CNN$ model is used to classify the response or neural activity of $fMRI$ according to the False-Belief scheme between the age group of 3 to 80 years while watching a silent movie. Study of MRI image visualization of a hidden layer of the CNN model that used

a regularization technique to bias the image. Two approaches, such as $XRAI$ and GIG, are applied to generate the saliency map of the image MRI. Finally, we develop a model $BLSTM$ to classify healthy control subjects and subjects affected by ADHD.

CHAPTER 4

FUNCTIONAL CORRELATION IN FMRI

4.1 Introduction

Correlated Region and Functional Network: We evaluated the $BOLD$ signal as a marker for processing spatial or temporal factors through spontaneous and specific forms of tasks. $BOLD$ signal may be triggered by concurrent coactivation signals. The parameters we identified to measure FC and use Pearson's correlation provide insight into FC. Applying $BOLD$ signals with an estimated maximum probability, the voxel-wise linear method yields the correlated components of the regressors. fMRI results are generated directly from the $BOLD$ signal; from the $fMRI$ data, the GM, WM and CSF signals are extracted. In the context of functional networks, White matter (WM) also known as axon which perform the structural connectivity and connect several brain regions. In the brain, the majority of the cells that make up neurons are found in the grey matter (GM).GM has substantial effects on mental processes, memory, emotions. A watery fluid known as cerebrospinal fluid (CSF) flows constantly across the surface of the cerebral cortex and spinal cord as well as inside the ventricles.

4.2 Correlated Region and Functional Network

The values of $T1$ vary among various types of brain tissue. CSF has significantly more relaxation time than WM, as seen in Figure 4.1a, which shows it due to a certain amount of time needed to relax WM, GS and CSF. Figure 4.1 b shows the calculated correlation mean of the Functional Connectivity Network. The values obtained are $CSF = 642.63$, $WM = 678.78$,$GS = 869.95$, $SDVars = 1.36$, $DVars = 39.23$ and $FD = 0.27$. $T1$ differs according to the types of tissue that can be used to illustrate the boundaries between CSF, GS, and WM.

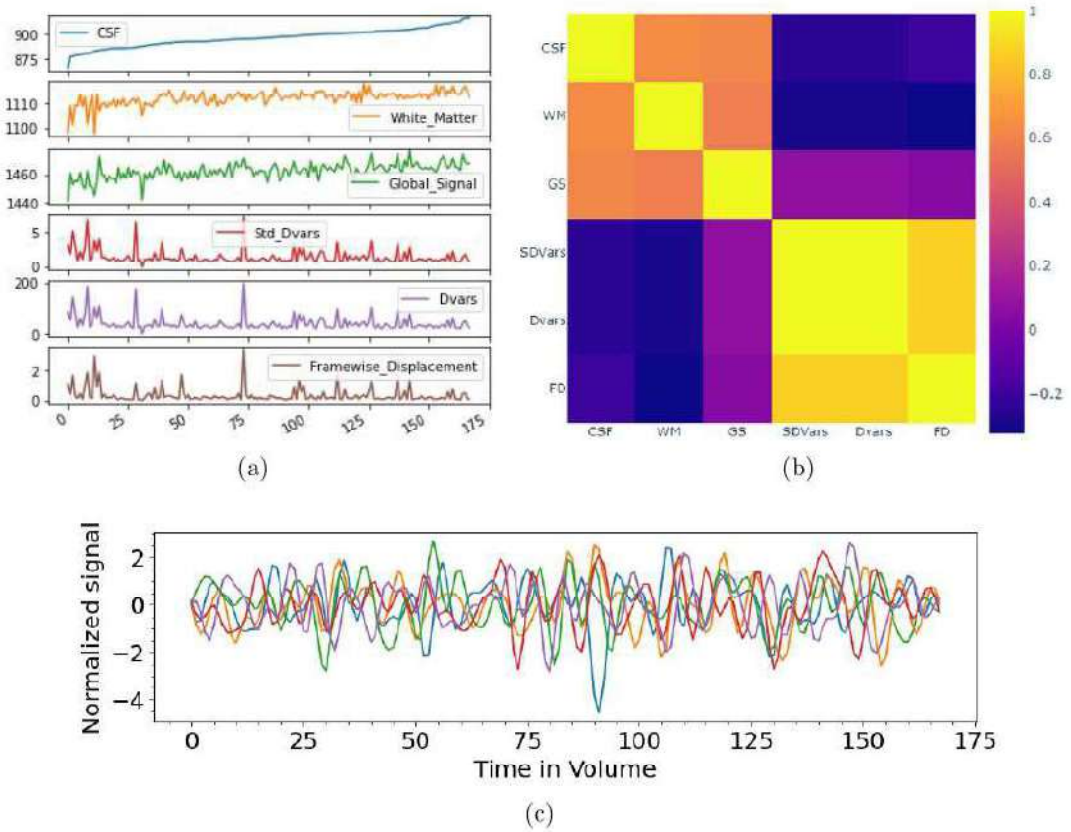

Figure 4.1: (a) BOLD time series depicts the signal that is from CSF, white matter, Global signal DVARS, and framewise displacement. (b) Correlation matrix of the Voxel region in time series with the mean network structure. (c) Normalized time-series shape of the voxel.

Figure 4.1b shows the connections between CSF, WM, GS, $SDVars$, $DVars$, and

FD in the different regions of the brain. In our experiment $fMRI$, a series of $fMRI$ images was obtained based on the oxygenation pattern within the brain over time. Therefore, the sequence of brain images obtained is shown here. The single voxel representing a spatial position and intensity is correlated to this; essentially, we obtain each voxel containing the subsequent images shown in Figure 4.1c the temporal sequence of the intensity value for that specific spatial region over time. Changes in the $fMRI$ signal have been caused by instantaneous brain activity (HRF). The BOLD signal might decrease as a result of early increases in deoxyhemoglobin. The time course of every voxel, or essentially 32504, is a part of WM, GS, and CSF. In particular, the voxels are part of CSF.

The resulting voxel activation parameter is shown in Figure 4.2 a, which determines the amplitude, distribution, and latency of activation response signals $BOLD$ related to brain activity. The extracted brain network in Figure 4.2d and the corresponding correlation mean matrix in Figure 4.1b show the spanning on every region of the brain that was recovered. At this particular time, the $fMRI$ image and the proposed algorithm were implemented, which automatically discovered the proper locations to map connectome networks. We were able to determine the correlation between the various regions of the brain, and the correlated results are $[0.02, -0.57, -0.06]$, which we have shown in Figure 4.2c using the correlation matrix. The voxel time series generally appears to be stationary in the analysis of $fMRI$, and the voxel-by-voxel FC of the signal $BOLD$, as demonstrated in Figure 4.2e, was determined using temporal correlation. A correlation coefficient was obtained. We discovered the Pearson correlation coefficient $\{r = 0.69\}$ and linear regression is demonstrated in Figure 4.2b $\{r = 0.0094\}$ across seed signals as well as seed data. Minimum differences between total measured seed data and seed signal are $\{p < 0.00005\}$ and $\{R^2 = 0.45\}$, and the precision of the predicted signal and the

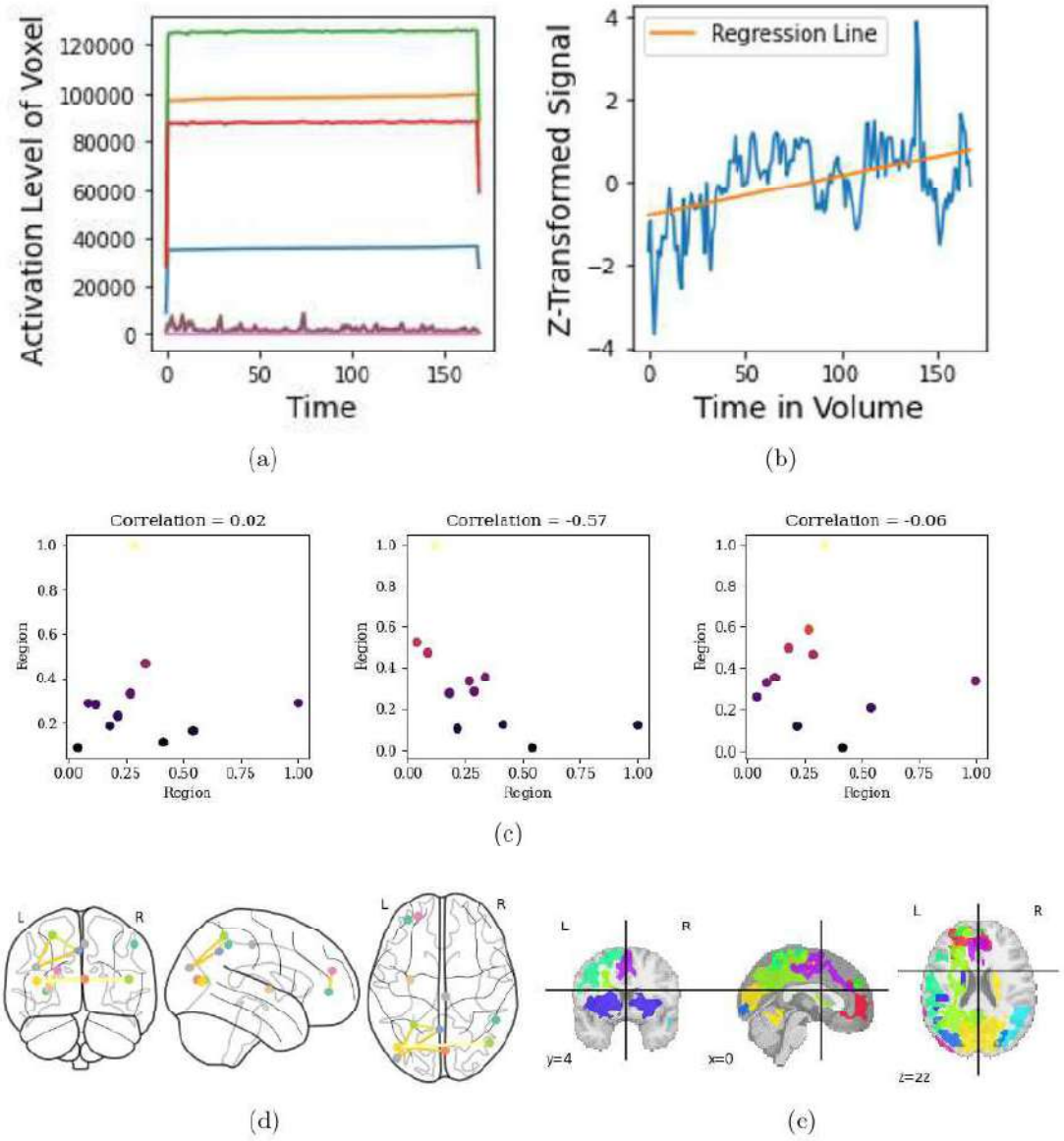

Figure 4.2: Functional Correlation and fMRI time series from different ROI. (a) For every voxel in the seed region, Toeplitz convolution based on the BOLD signal is performed at the task activation level. (b) Seed region regression; (c) Coefficients of correlation illustrate how the mean affects the fMRI time series. (d) Connection and correlation of the fMRI regions (e) Strongly correlated neuroactivity is observed in the functional network

precision with respect to the predicted signal are $\{s = 0.0014\}$. Regularization of a time series that appears in the mask that is generated by Global Signal (GS) with minimal pre-processing FD) and evaluation of DVARS is based on variation over voxels, especially time courses, to produce an exclusive head motion specification within every time frame.

FD and derivative root-mean-square $DVARS$ motion measurements are obtained from three translational and 3 rotational parameters determined by $R = [XYZ \text{ yaw }]$ Observed in Figure 4.2a. The calculated value of (FD) is considered to represent the sum of the absolute derivatives of the independent term using three rotational parameters as well, and the stipulated parameters are multiplied by a consistent radius value of 50 to convert them to a certain extent. To evaluate the effectiveness of linear regression for eight networks, both the linear estimate and the voxel time series are taken into account. The minimum and maximum correlation information that we were able to estimate was $[-0.731, 1.927]$, respectively.

4.3 Edge Detection on MRI

Shocking fluctuations in the intensity of the MRI image specifically correspond to the image. The Laplacian, Sobel, and Prewit operators are most frequently used to detect edges, as discussed in Section 3.2.2. The Laplacian edge of the MRI image was obtained in Figure 4.4a. An ROI approach is used to calculate the intensities of the signals, which are produced in Figure 4.4d. The beginning point of brain clustering occurs when gray and white matter coexist and Laplacian is applied to gray matter. The concentration of the histogram can be observed in the middle of the scale along an edge pixel. The histogram observation shows the intensity of an MRI image toward the center of the horizontal axis; it is the highest value that is allowed. Figure 4.4b displays the magnitude of the Sobel gradient. Calculating the Sobel gradient for the distribution, the resultant of $|g_x| + |g_y|$ is predicted to be 255. The spatial distribution of the entire axial image is demonstrated by the signal strength along the x-axis and the number of pixels on the y-axis that correlate

with the signal, which is shown in Figure 4.4e and Figure 4.4f.

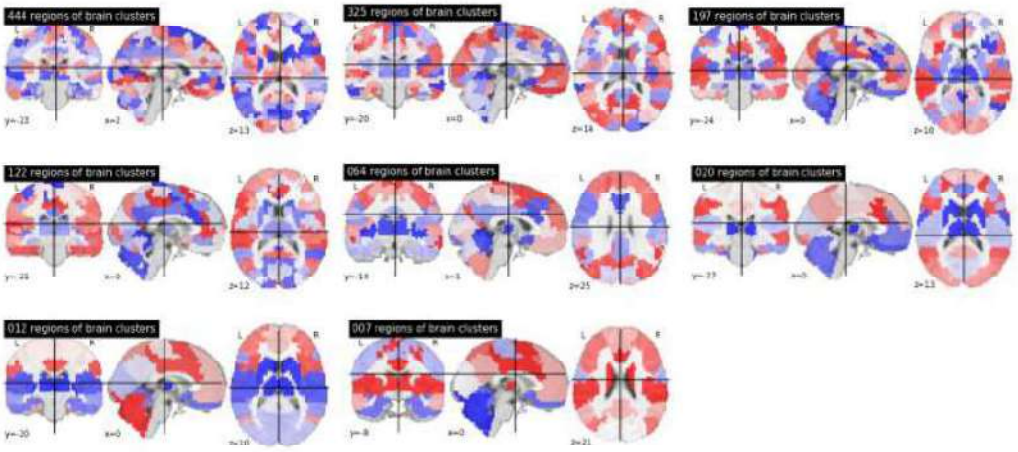

(a)

Figure 4.3: Brain Cluster Multiple scales (number of networks) are available and include 7, 12, 20, 36, 64, 122, 197, and 325

4.3.1 MRI gradient's similarity measure

The MRI image changes from location (i, j) to a different position; subsequently, the gradient of the image varies the brightness and pattern of the image due to the differences in the gradient in each direction. The HOG method extracts the gradient orientation. Prewitt and Sobel masks are composed of two kernels, (3×3). The rate at which the intensity of the image changes is demonstrated in Figure 4.4 b. In Prewitt, the gradient MRI signal is nearly constant; however, as shown in Figure 4.4d, it is related to the Sobel gradient, which shows an abrupt change in intensity at the highest point and represents the edge threshold in the MRI image of the subject. The object within the image benefits significantly from this skewed gradient. Due to the smaller size of the kernel matrix when using the Laplacian gradient, the intensities vary most quickly, with a slight fluctuation in intensity $I(x, y)$, which produces a brain signal. Figure 4.4 shows fluctuations in brain

intensities and a significant increase in intensity in each case. We illustrate the gradient information that possesses an effective contrast MRI image. In this study, we examined that Figure 4.4a is made sharper due to the Laplace gradient, in which the intensity function rapidly changes and the edge pixel is rapidly modified, demonstrating the presence of noise in the signal. Figure 4.4b shows the similarity between each pixel. The right portion of the MRI image is nearly white with minor noise. Figure 4.4c shows nearly identical white edges; however, the central region within the smooth gradient image presents some noise.

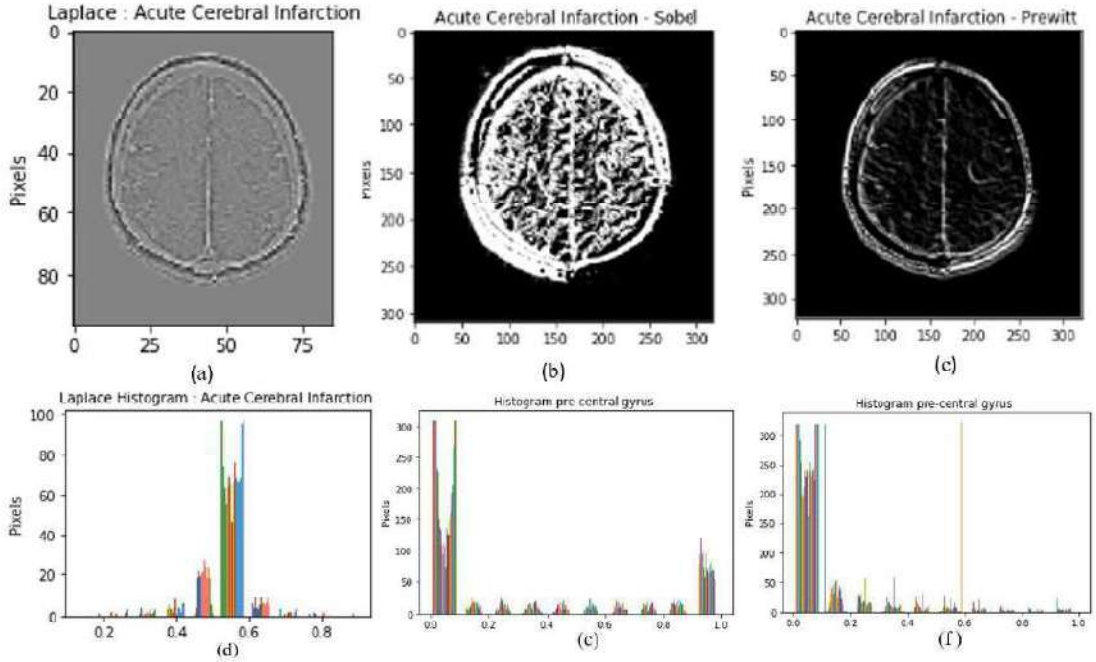

Figure 4.4: Gradient Image for MRI.(a) Laplace gradient MRI image. (b) Sobel gradient MRI image. (c) Prewit gradient MRI image. (d)Histogram for the pixel distribution for Laplace gradient MRI. (e) Histogram of the pixel distribution for Sobel gradient MRI. (f) Histogram for the pixel distribution for Prewit gradient MRI.

4.4 Conclusion

In this chapter, we have discussed and examined several MRI edge analysis methods, and techniques that have been formulated for studying how brain networks work utilizing the essential, task-related fluctuations in BOLD fMRI signals. We developed a computational method that works well and demonstrates a new way to analyze functional networks with a common spatial structure deduced from BOLD signals. By evaluating the FC score and voxel deviation across the $fMRI$ time series. The spatial patterns of WM connectivity are identified by activation based on times series WM. When measuring human brain activity using fMRI after completing a particular task, it is highly helpful in identifying a region. A general clustering was produced for each of the distinct clustering replications combined in a pool, thus producing clusters of groups. The identification and analysis of voxel clusters are provided by the ROI. Edge selection, which depends on the edge identification operators of Laplacian, Sobel, and Prewitt.

CHAPTER 5

CLASSIFICATION OF BRAIN ACTIVITY AND DISORDER

5.1 Introduction

It has been discussed in extensive detail whether specific and spontaneous types of neural activity occur from identical cognitive processes or more accurately represent various processes. In addition, the use of the Convolutional Neural Network (CNN) framework along with the $LSTM$ network helps to develop deep learning predictive models from the available data set, such as images MRI and $fMRI$. We tested our proposed deep learning models on a publicly available dataset $MRI/fMRI$ to obtain the following results:

1. **Seed Based FC and neural activity classification:** Task-based $fMRI$ shows that the $BOLD$ signal activates neurons to a particular task. Spontaneous variations in signal strength at low frequencies ($< 0.1 Hertz$) occur when the $BOLD$ signal is used for a cognitive task. Our proposed $2D-CNN$ model extracts the fMRI feature maps to classify brain activity. The performance of the proposed model $2D-CNN$ for the classification of neural activity is shown in Figure 5.3, these results were

obtained using an fMRI task-evoked data set.

2. **Saliency Map generation of MRI images:** Due to the highly complex behavior or nonlinearity of $2D-CNN$, there are several challenges. The saliency map serves as an effective strategy for the evaluation and visualization of the non-linear behavior of the $2D-CNN$ model.

3. **LSTM and CNN based model for ADHD/MS classification:** The rs-fMRI BOLD signals can be used to diagnose neurological disorders and it is suitable for visualization of RSN. For the classification of disorders such as ADHD, we have proposed a modified BLSTM model to classify brain disorders. In the case of brain disease, that is, multiple sclerosis, we implemented a MobileNet network at baseline along with 2D-CNN to generate the class activation map for MRI images, which can be visualized in Figure 5.13, the result of the lesion detection and classification of MS disease are demonstrated in Figure 5.14.

5.2 Seed-Based Functional Connectivity

Section 3.2.3 deals with the seed-based technique, which produces a spatial map of temporal sequences that cause the fMRI dataset to regress. Extracted time series fMRI, including every voxel in the seed area. The size of the seed voxel has a covariate effect. The correlation may be observed in the functional network as displayed in Figure 5.1a between the seed voxel and the voxel, where the dimension of the BOLD time series is 32504168 and the input size of the dimension of a seed to the voxel is 325041. CNN accuracy for neural activity classification is influenced by the specific kind of seed-based analysis. As a result, we determine that the minimum and maximum correlated parameters are

-0.624 and 0.958, respectively, which is shown in Figure 5.1b of the cognitive covariate that influences functional connectivity from seed to voxel. BOLD fluctuations and brain activity can be observed in the input dimension, which is equivalent to $67 \times 77 \times 34$ in the proposed model $2D - CNN$. The accuracy obtained from $2D - CNN$ is affected by the choice of seed-based analysis.

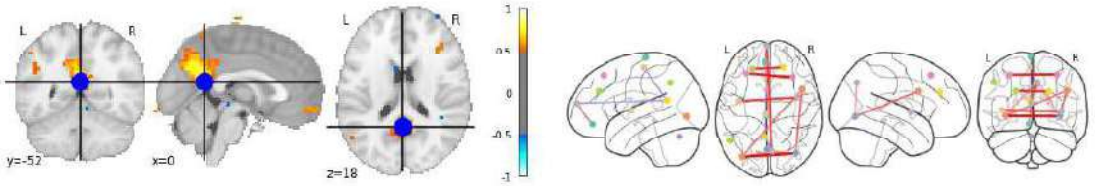

(a) (b)

Figure 5.1: Seed-voxel connectivity (a) Seed-to-voxel coordination (b) Seed-to-voxel Functional Connectivity

5.2.1 Neural Activity Accuracy of $2D - CNN$ model

A random rearrangement was performed on 134 training samples, which included $4D - fMRI$ time series data. The entire fMRI image is made up of two classes, which also form the responses $fMRI$. Furthermore, there are 34 fMRI validation datasets that account for 20% of the total $fMRI$ images. The $2D - CNN$ framework is updated over 200 epochs, then enabled $StochasticGradientDescent$ using a single training update learning rate of ($lr = 0.000001$). Each $fMRI$ image had a mean, which was subtracted from it. The $2D - CNN$ uses kernel size (3×3), three convolution layers, and a single $Softmax$ function was added to each kernel. A batch size of 16 was used for layer training and hyperparameter values were adjusted. The impact of loss has been measured using a categorical cross-entropy, and the $ADAM$ optimizer has been used to improve convergence. Based on the response to the voxel, the prediction precision of the proposed

Table 5.1: **Accuracy and Loss for training and Validation Data**

Model	Kernel	Activation	Training Accuracy	Training Loss	Validation Accuracy	Validation Loss
2D-CNN	3×3	ReLU	84.32	41.85	85.29	36.19

$2D-CNN$ framework has been determined. Voxel responses are used to calculate the prediction accuracy of the proposed framework $2D-CNN$ presented in Table 5.1. In Figure 5.2a, the higher levels of accuracy are displayed for the validation data produced by the $2D-CNN$ framework.

5.2.2 Evaluation of Model Performance

The results of the evaluation of the proposed $2D-CNN$ model are presented, which considers the precision, precision, and F1 score of the 168 samples collected from subjects 155. The typical procedure for assessing a learned CNN model is to maximize the accuracy score. Metrics such as precision, F1 score, recall, sensitivity, specificity, and precision are part of the empirical analysis. When addressing the binary classification problem for class labels such as TP, TN, FP, FN and considering Neural Activity, No Neural Activity be the predicted true positive and false negative class labels, To calculate these measures, use the following expression:

$$Sensitivity = \frac{TP}{TP+FN},\ Precision = \frac{TP}{TP+FP},\ Specificity = \frac{TP}{FP+TN}$$

$$F1-Score = \frac{TP}{TP+\frac{1}{2}(FP+FN)},\ Accuracy = \frac{TP+TN}{(TP+FP)+(TN+FN)}$$

Statistical analysis is performed to assess the classification performance of the CNN

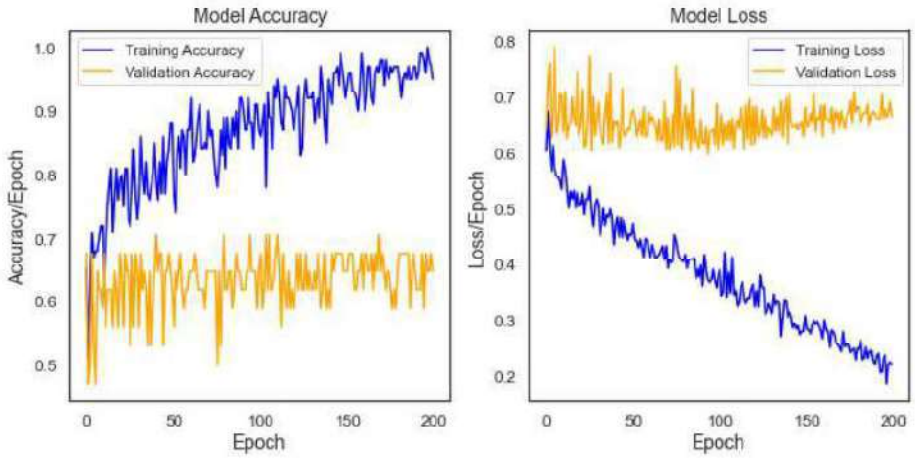

(a) (b)

Figure 5.2: Model Performance (a) Training and Validation Accuracy (b) Training and Validation Loss.

model and then visualize the correlation among the predicted and observed results with the help of a confusion matrix. The performance of the proposed $2D-CNN$ model using the four distinct categories of a confusion matrix is shown in Figure 5.3a, and the estimated classification probability is shown in Figure 5.3b. Using the Matthews correlation coefficient (MCC) that exists between the predicted and observed brain activity of the confusion matrix, we found the classification information as demonstrated in Table 5.2. MCC lies in the $[-1, +1]$ interval. Prevalence (P) influences MCC, specificity, as well as Sensitivity & Bias (B), which are determined by the data set and the classifier. The prevalence (P) is the percentage that represents every predicted positive neuronal activity within the test data set. Furthermore, bias measures how well the classifier predicts for the test data set and is described as follows.

$$MCC = \frac{(TP \times TN) - (FP \times FN)}{\sqrt{(TP+FP)(TP+FN)(TN+FP)(TN+FN)}};\ P = \frac{TP+FN}{N}, B = \frac{TP+FP}{N}$$

Figure 5.4a shows the predicted class of brain activity for the original fMRI. The predicted binary class correlates with Figure 5.4b, which includes validated and training

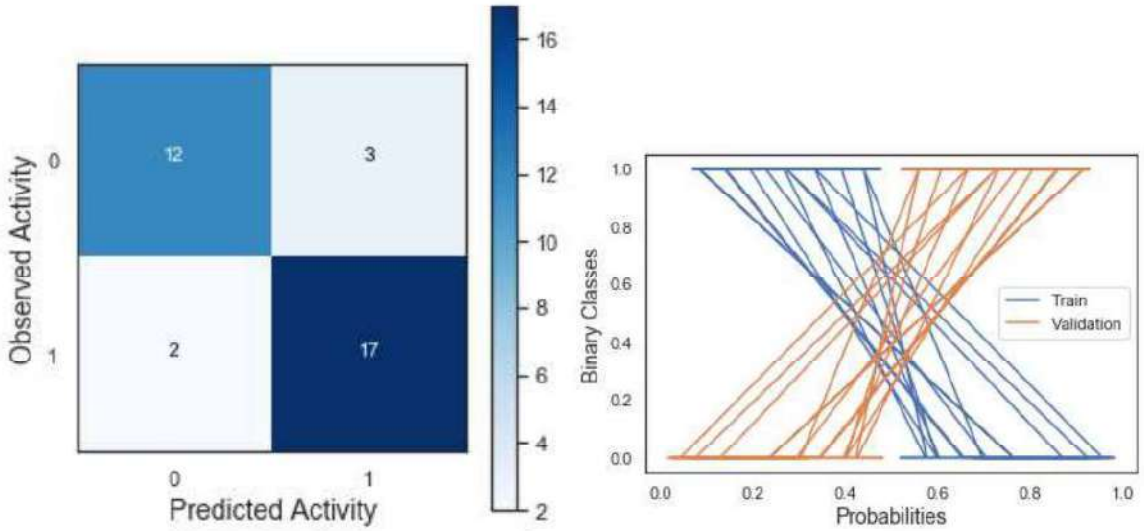

(a) (b)

Figure 5.3: Classification performance (a) Confusion Matrix for fMRI response using 2D-CNN model (b) Predicted classification value for Training and Validation fMRI data.

fMRI data.

Table 5.2: **Classification Report of Proposed 2D-CNN Model**

Classifier	Accu	Sens	Spec	Prec	F1-Score	Prev	Bias	MCC
2D - CNN	85.3	89.5	80	85	87.2	55.9	58.8	70.1

In the Table 5.2 where Accu: Accuracy, Sens: Sensitivity, Spec: Specificity, Prec: Precision, Prev: Prevalence

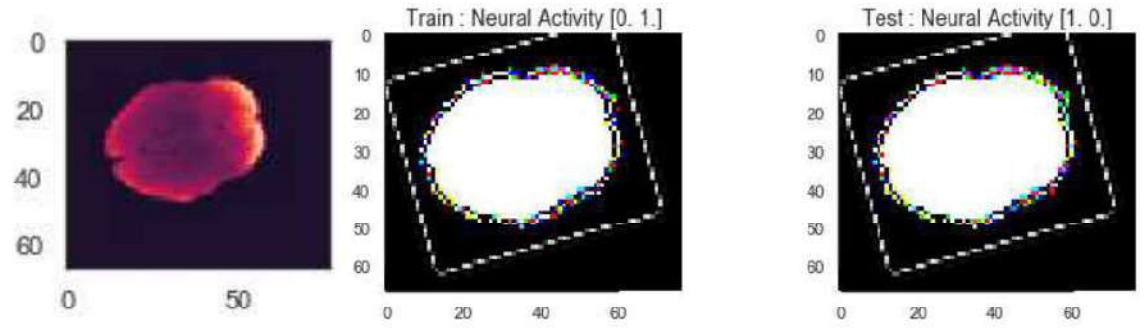

(a) (b)

Figure 5.4: Active state of brain fMRI (a) Convolution Layer activated fMRI (b) Neural activity activation of fMRI response

5.2.3 Classification of Voxel Response fMRI images

Tensorflow and Keras were used to develop $2D-CNNmodel$ and is trained using a $Nvidia\ Geforce\ GTX\ 1080\ GPU$. To classify the voxel response, the optimizer $ADAM$ must discriminate between activation and nonactivation of the voxel. The entire brain voxels (size = 50×59×50 and to extract time series) specify the extraction mask to fill the dimension of the brain with a brain mask to obtain data from the cerebral region were used as input for the model CNN. Here, we classified the image $fMRI$ using the characteristic extracted from the response $fMRI$. With our proposed model $2D-CNN$, we achieved an accuracy of 85.3% in the classification of brain activity activation.

5.3 Saliency Map for MRI images

We applied an end-to-end deep neural network to generate a saliency map for the Alzheimer's Disease (AD) affected image MRI. $ImageNet$ was used to train the CNN-based $VGG-16$ network, in which we initially reduced the mean of each pixel in the images before feeding the training images to the $VGG-16$ network in $ImageNet$. Pre-trained network $VGG-16$ as base frameworks for classification of AD in MRI images. In the case of the extraction of attributes, a differential threshold-based sensory characteristic was used. The differential threshold is the lowest possible variation that the human visual system is able to distinguish between two identical homogeneous physical stimuli, as shown in Table 5.3. The input layer of a $VGG-16$ network receives and forwards the input MRI image to a number of hidden layers, and these layers modify the input of the MRI image data. The weight is a learnable internal parameter for the whole network, and it is modified to provide the appropriate output and the required result. A change in input weight

will have varying effects on the output. A minimum weight value will not affect the input, whereas a maximum weight value will mostly influence the result. Figure 5.5 illustrates how the performance curves for the minimum and maximum weight vary significantly depending on the size of the image MRI.

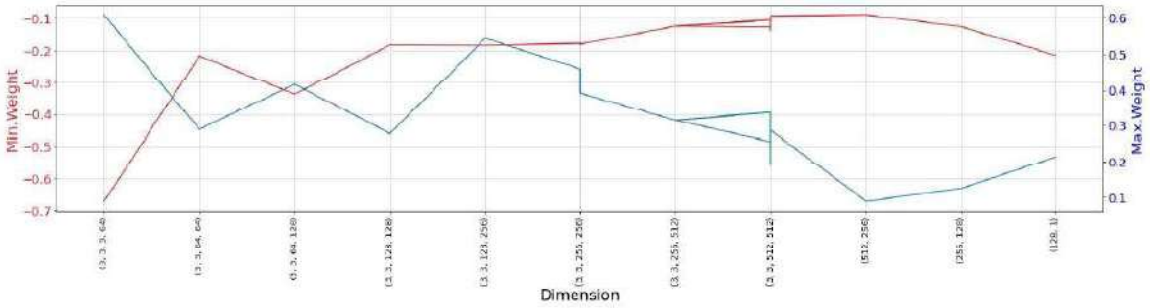

Figure 5.5: Weight parameters for the dimension of CNN layers

5.3.1 Attribution for MRI images

The fundamental idea of our proposed interpretation strategy, as discussed in Section 3.4.1, is that visual analysis is essential for decision-making in MRI evaluation. Consider the saliency map to obtain computing metrics. The absolute number of total attributions throughout the color channel is shown in Figure 5.6(a), (b), (c), and (d). This involves creating a random mask for healthy and AD affected MRI images that were originally completely blurry. The fully blurred MRI image has the same score as the original image MRI or a higher score. Table 1 shows an overview of the experimental findings. Table 4.3 shows an overview of the experimental findings that calculate the AUC value for each experiment. We use integrated gradients to highlight which pixels appear to be the most essential for the appropriate prediction generated by the $VGG-16$ network. The most significant pixels are represented by white pixels. We can observe in Figure 5.6(a) & (b) where $x_i \mid \alpha(x \quad x_i)$. The healthy MRI image that was interpolated between the

input and baseline healthy images, the gradients in the MRI image that was interpolated, adding several gradients of similar types across α.

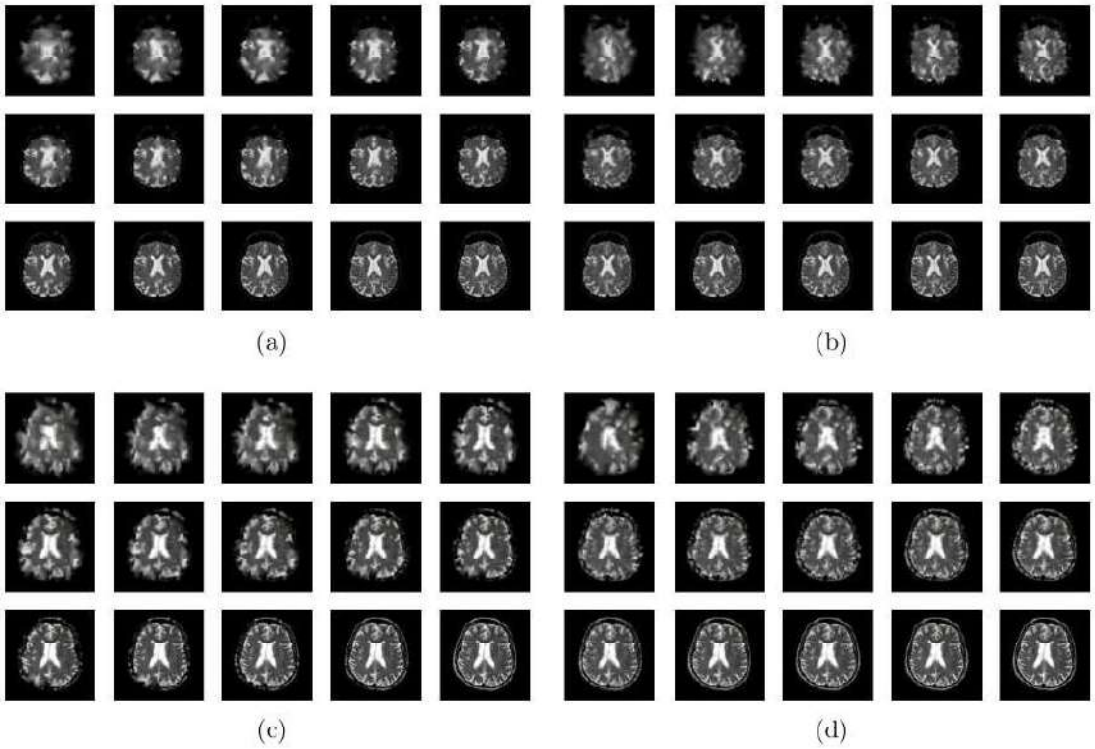

Figure 5.6: Fully blurred Healthy and Alzheimer's MRI images have the same or higher score as compared to the original MRI image (a) Healthy Integrated Gradient (b) Healthy, Smooth Gradient (c) Alzheimer's Integrated Gradient (d) Alzheimer's Smooth Gradient

5.3.2 Integrated Gradient on MRI Image

An improved $VGG-16$ was used as the classifier. In Figure 5.7, the integrated calculated gradients are shown, which are generated from the baseline model. With the least amount of noise, the saliency precisely determines the areas that have been affected by AD. Visual incoherence is significantly greater in integrated gradients and behaves much like saliency maps that are produced at random. A non-smooth binary map is generated using the fixation data for every MRI image and contrasted with a binary map that represents the aforementioned values in Table 5.3 with a steadily increasing threshold for every saliency

Table 5.3: **fMRI Image Saliency Map Prediction**

	Healthy MRI			**Alzheimer's MRI**		
Threshold	x	$x - x_i$	p_i	x	$x - x_i$	p_i
0.000	0.000	0	0.0003	0.001	0	0.0005
0.005	0.003	0	0.0009	0.001	0	0.0006
0.010	0.003	0	0.0019	0.001	0	0.0019
0.020	0.001	0	0.0054	0.000	0	0.0351
0.030	0.013	0	0.0066	0.001	0	0.0127
0.040	0.008	0	0.0128	0.002	0	0.0642
0.050	0.007	0	0.0132	0.003	0	0.5848
0.009	0.070	0	0.0045	0.032	0	0.3794
0.013	0.100	0	0.0488	0.001	0	0.7168
0.086	0.130	0	0.0390	0.191	1	0.3440
0.123	0.210	0	0.0412	0.201	1	0.5546
0.118	0.340	0	0.3541	0.725	1	0.3972
0.213	0.500	0	0.4685	0.563	1	0.1785
0.553	0.750	1	0.4373	0.474	1	0.3678
0.396	1.000	1	0.3960	0.376	1	0.3763

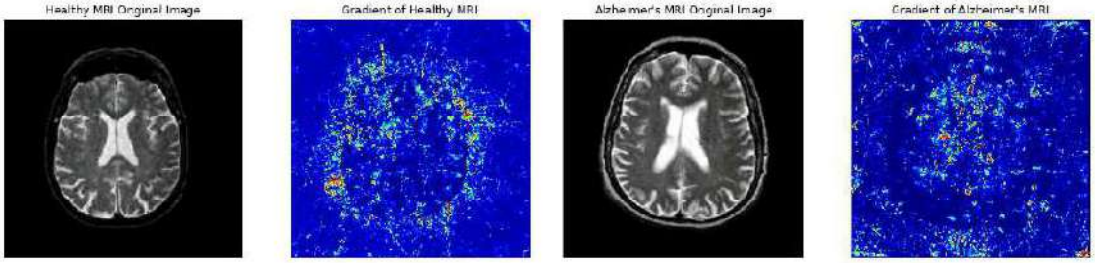

(a) (b)

Figure 5.7: Integrated Gradient of Healthy and Alzheimer MRI Image and attribution maps in ImageNet Data Set

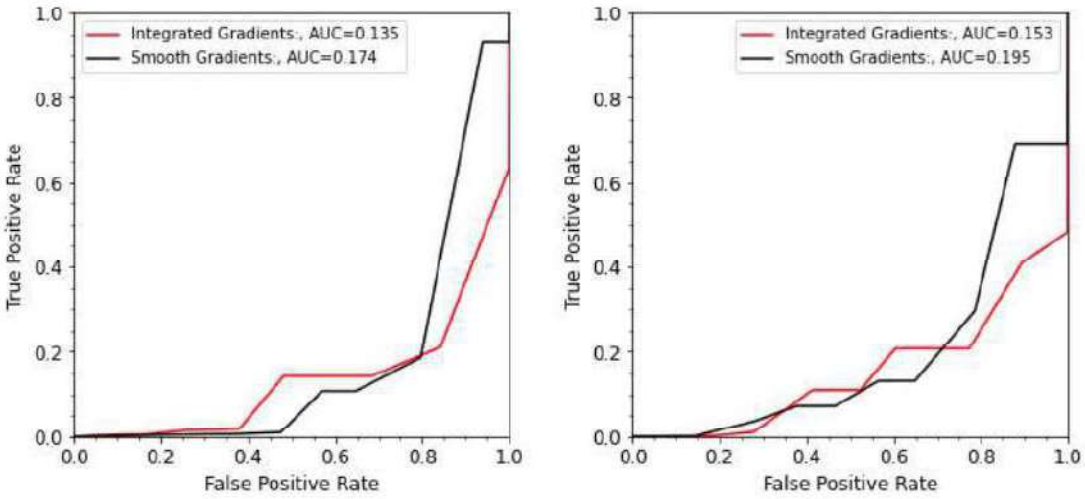

(a) (b)

Figure 5.8: Comparative AUC score of the integrated and smooth gradient for the Healthy and Alzheimer MRI image (a) Healthy MRI image (b) Alzheimer's MRI image

map. Total attributions in the color channel are displayed in Figure 5.7a, and Figure 5.7b. It produces an arbitrary mask for the first fully blurred image obtained from healthy and AD MRI scans. According to Table 5.3 which determines the AUC score demonstrated in Table 5.4, the completely blurred image receives a score similar to the original image or a higher score.

Table 5.4: AUC score determined from Table 5.3.

Subjects	**Integrated Gradients**	**Smooth Gradients**
Healthy	0.135	0.153
Alzheimer's Disease	0.174	0.195

5.3.3 Gradient MRI Images on ImageNet

For the $ImageNet$ dataset, a refined $VGG-16$ architecture was used to show the efficacy of the structure and depth of the network. Figure 5.7 illustrates that a resulting image generated from an active hidden layer of the baseline model, a saliency map applied to an image $fMRI$, using a computed integrated gradient and a smooth gradient, accurately detects the regions that have been affected with the minimal amount of noise. A smooth gradient creates smooth saliency maps. Integrated gradients appear similar to arbitrarily produced saliency maps and have significantly higher degrees of visual incoherence.

5.4 LSTM based model for ADHD classification

The proposed BLSTM methodology and model, as described in Section 3.4.3, use $rs-fMRI$ images for a wide variety of evaluations, such as image pre-processing; furthermore, dimension reduction is applicable to feature vectors in which the $fMRI$ temporal signal from every voxel is connected to another voxel. Our study further reveals the $fMRI$ voxel activation feature, which represents the neural response to a stimulus. We have shown particularly low-frequency variations in Figure 5.9, which is $< 0.1Hz$ considering the spontaneous signal of $BOLD\ fMRI$ during rest and in the absence of any task. The efficacy of the proposed $BLSTM$ model is assessed using various RSN feature vectors of the $rs-fMRI$ time series data for healthy subjects and $ADHD$. In contrast, the proposed enhanced performance of the $BLSTM$ model and that of the stacked $LSTM$ were obtained with the help of training and testing of the $rs-fMRI$ feature vector. An automated deep learning Python package has been used to process the $rs-fMRI$ feature vector to train the $LSTM$ model. The details of the experiments and the results

are given in the following subsections.

5.4.1 RSN Feature Visualization

In order to show RSN, we have taken into account the data set that contains participants with and without $ADHD$ in this section. The input image $rs - fMRI$ uses the yellow area in Figure 5.9a, which was found using the statistical map approach for the image $fMRI$. An axial slice is produced by considering the entire data set. The visualization generates a map $28 - RSN$, as stated in Table 5.5 that defines every active location that influences the classification. The brain voxel has a dimension of $(61 \times 73 \times 61)mm^3$, it has 271633 voxels.

Table 5.5: **T-maps of 28 RSN Components**

Resting State Network	**Indices**	**Connected Node**
Basal Ganglia	21	1
Auditory	17	1
Sensorimotor	7, 23, 24, 38, 56, 29	6
Visual	46, 64, 67, 48, 39, 59	6
Default mode	50, 53, 25, 68	4
Attentional	34, 60, 52, 72, 71, 55	6
Frontal	42, 20, 47, 49	4

each of which is $(3 \times 3 \times 3)mm^3$ in size. Additionally, the behavioral data of the 40 participant $fMRI$ time series are collected and organized with a matrix size of $[40 \times 65]$ that contains 176 time stamps, indicating a significant fluctuation.

The stimulated voxel sequence is optimized during each time stamp after obtaining the time stamp range, and Figure 5.9c displays the temporal pattern of the voxel. Additionally, Figure 5.9b illustrates at volume 75 , the kernel density curve estimation process

Table 5.6: **rs-fMRI parameters**

fMRI Parameter	**Value**
$4D$ array from resting state fMRI	(61, 73, 61, 176)
Sequence of $3D$ resting state fMRI volume	(61, 73, 61)
Number of Voxel	271633
Re-shape the array with voxel and time	(271633, 176)
Max. value for the array of all $4D$ resting states	21922.8526

starts and finishes in volume 261 . This curve shows the probability density measurements, at both volume 75 and 261 , correspondingly 0.003 and 0.004.

(I) **V**oxel fMRI Response: $BOLD\ fMRI$ The signal is contained in the time series, it is a mixed signal and depends on the three limitations such as (i) Blood Flow (ii) Blood Volume and (iii) Blood Oxygenation. The $BOLD$ responses are included in the aforementioned resting state data set and applied to preprocessing for each voxel. The voxel-specific response period was calculated and reconstructed from the seven brain regions shown in Table 5.5. As we pre-processed the values of the $rs - fMRI$ time series, we evaluated the amplitude and size of the $BOLD$ signal. The signal variations over the volume that are specific to each of the seven RSN, Figure 5.10 display the time of activation and nonactivation in close vicinity. The voxel signals are extracted from the volume using the $rs - fMRI$ time series, and the signal itself determines it. For 40, the study is carried out on these reshaped $RSN28$ data. There are 20 participants with $ADHD$ and 20 controls, and each subject has a unique feature vector $(40 \times 261 \times 28)$, According to Figure 5.9b, they were fitted with a model $LSTM$.

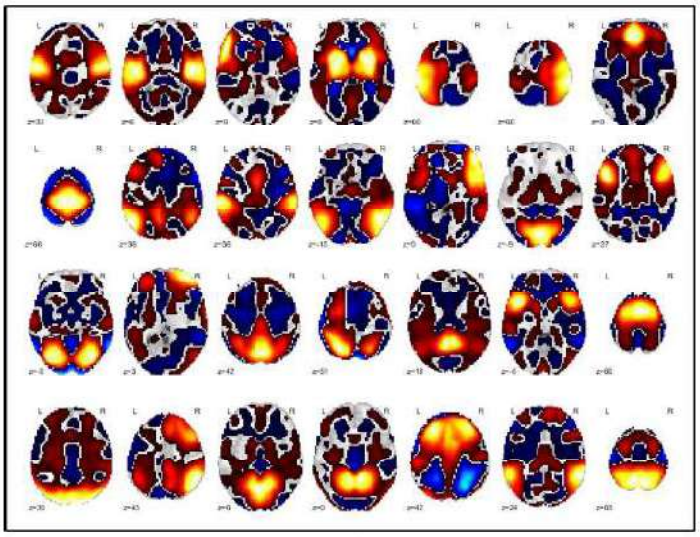

(a)

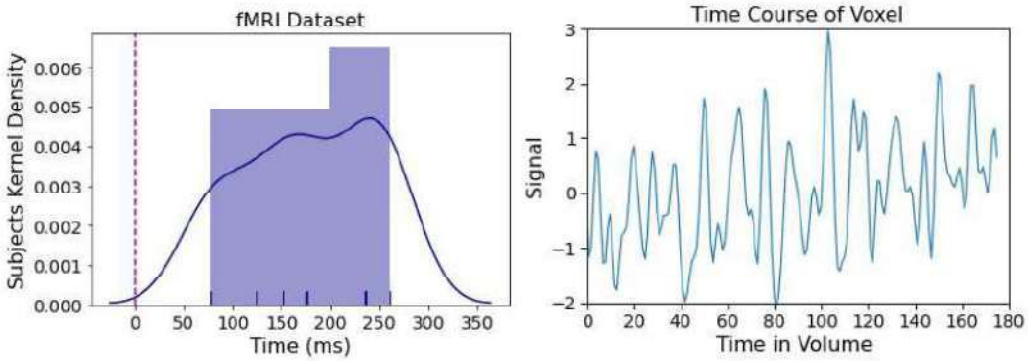

(b) (c)

Figure 5.9: Visual Results of RSN and Signal Visualization (a) The yellow region shows 28 RSN (b) Histogram and kernel density estimation curve of all subjects' fMRI data from ADHD and controls with 261 images (c) volume $4D$ rs-fMRI dataset ($3D$ *spatial* + $1D$ *Time*) and signal observation from the voxel array.

(II) **S**ignal variation: It is possible to determine neural activity using the signal $BOLD$. Each voxel's time series value corresponds to the $BOLD$ signal. We observe the significant variations in the $BOLD$ signal, which is illustrated in Figure 5.9a statistical map. We have also examined the $fMRI$ time series in order to find a signal at certain points in time. In functional connectivity, FC, according to Table 5.5, several brain regions are functionally related. A process has been used to identify each of the seven unique regions in order to calculate the temporal correlation of

$(Low\ frequency\ \approx 0.01 - 0.1Hz)$.

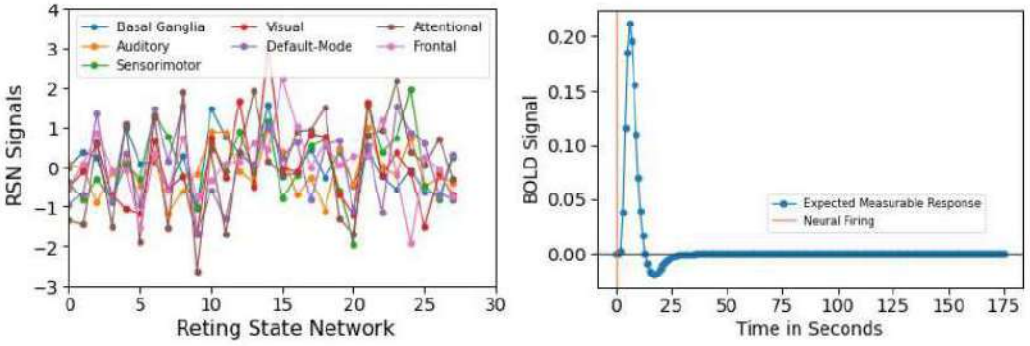

(a) (b)

Figure 5.10: Signal variation in the FC network and the BOLD response (a) RSN-28 Activation Signal and (b) BOLD signal, which is an indicator of neural activity in the resting state in the 28 RSNs.

variations in the $ADHD$ participant's magnetic resonance signals while in a rest state. We observe that spontaneous variations in blood flow are reflected by the low frequency. When determining the voxel in each region of the brain, signals from additional voxels are thus calculated simultaneously. Additionally, as Figure 5.9b illustrates, we have discovered that inside the continuous voxel time series $BOLD\ fMRI$ the signal fluctuates in frequency ($< 0.1Hz$) while it is at rest, which causes the intensity of the signal to change with volume. As demonstrated by the curve in Figure 5.9 b, it is highly probable that a pair of voxels or adjacent voxels in the brain perform a similar function. The highest and lowest spectral levels for amplitude exhibit a substantial correlation within the voxel time series spectrum. Figure 5.10 a shows the rs-fMRI signal in each of the 28 $RSNs'$ voxels, whereas Figure 5.9c displays the brain's throughput, thus the obtained signal spectrum indicates the coherent brain activity that appears in RSN. The degree to which each of the voxels is functionally connected to one another is shown by the time series as well as by each other voxel.

5.4.2 ADHD Accuracy

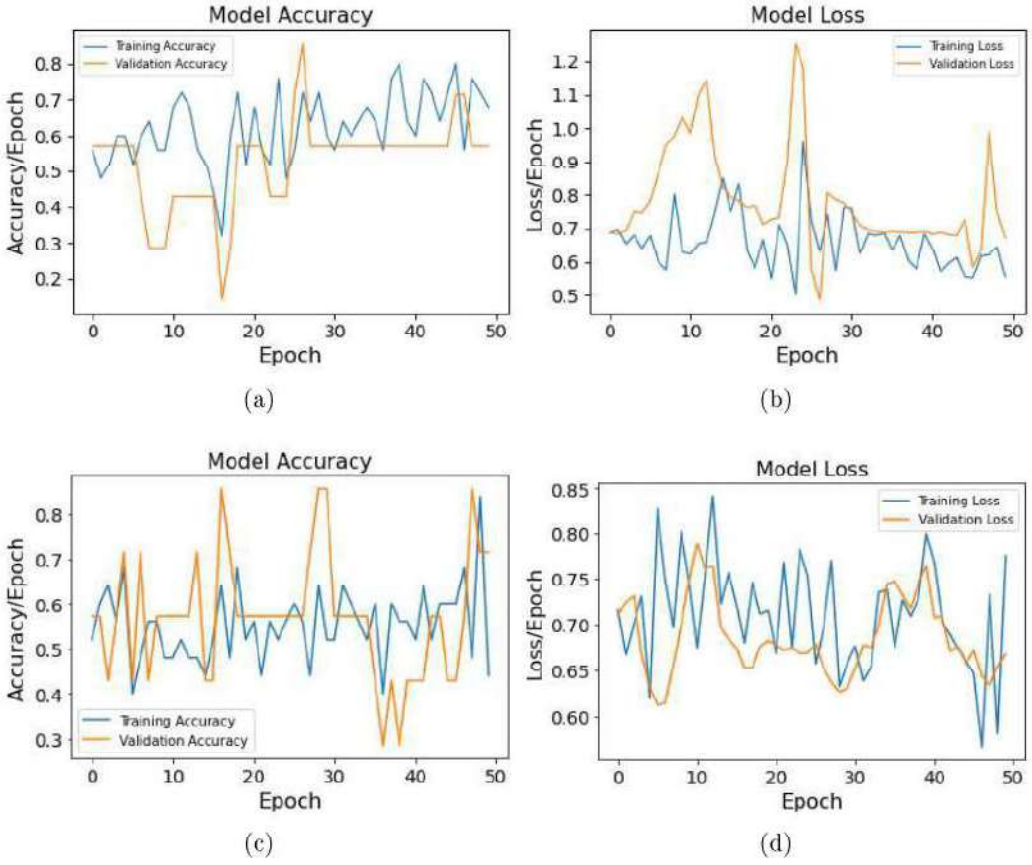

Figure 5.11: Stacked LSTM vs. Proposed modified bidirectional LSTM plot (a) Stacked LSTM accuracy and (b) Stacked LSTM loss. (c) Proposed modified Bidirectional LSTM Accuracy. (d) Proposed modified Bidirectional LSTM Loss.

The proposed enhanced $BLSTM$ model considers the feature vector sequence of $rs - fMRI$ time series data as input. The aforementioned feature vectors are trained using the proposed $BLSTM$ model, which includes 50 epochs and 50 iterations. Different hyperparameters concerning the training data set instantly adjust the model; these parameters are learned from the training data set. With every network pass, the weights are modified; consequently, despite the overfit and underfit, the ensuing curve finds an appropriate fit. The restructured data array comprised of $rs - fMRI$ images is used to implement both $LSTM$ models, such as stacked and modified $BLSTM$) to obtain more

Table 5.7: **Stacked LSTM Model**

Operation	Data Dimension	Weights (N)	Weights (%)
Input	(261,28)	-	-
LSTM,Tanh	(261,80)	34880	26.60
LSTM,Tanh	(261,70)	42880	32.30
LSTM,Tanh	(261,60)	31440	24.00
LSTM,Tanh	(50)	22200	17.00
Dropout	(50)	0	00.00
Dense	-	102	00.10
Softmax	2	-	-

Total params: 130,902
Trainable params: 130,902
Non-trainable params: 0

Table 5.8: **Proposed modified BLSTM Model**

Operation	Data Dimension	Weights (N)	Weights (%)
Input	(261,20)	-	-
LSTM,Tanh	(261,80)	32320	11.50
Bidirectional	(261,140)	84560	30.00
Bidirectional	(261,120)	96480	34.20
Bidirectional	(100)	68400	24.30
Dropout	(100)	0	00.00
Dense	-	202	00.10
Softmax	2	-	-

Total params: 281,962
Trainable params: 281,962
Non-trainable params: 0

training. Furthermore, we used the regularization procedure when the training dropout rate was 0.5 and an arbitrary choice of neurons from a network was neglected. The findings of both approaches concerning accuracy and data loss are shown correspondingly in Figure 5.11 a,b,c, and d. According to the findings, as more epochs are added, it can be observed that the accuracy of $ADHD$ subjects increases and decreases with

loss. Based on our findings, we were able to achieve binary precision 75.00% and loss 57.01%, respectively, with stacking $LSTM$. The accuracy and loss scores are 87.50% and 48.25%, respectively, for the proposed modified $BLSTM$. The total quantity of trainable parameters is shown in Table 5.7 and Table 5.8.

5.4.3 Model Performance Measure

In order to evaluate the efficacy of the proposed modified $BLSTM$ network, the "Bagging" or "Bootstrap Aggregating" method has been implemented. The approach creates more training datasets and reduces the variation in the learning algorithms. This approach has been used for the prediction of network accuracy and sample training. Additionally, we resampled the input vector, which has a significant sample size, and applied parametric analysis for distinct levels of variability. The null hypothesis distribution implies the absence of a relationship. An arbitrary substitution sampling is applied for training and testing in order to estimate the accuracy of the model. The hypothesis test is conducted using the bootstrapping approach to evaluate the precision of the proposed model, which is shown in Figure 5.12a and Figure 5.12b.

The proposed $BLSTM$ has obtained an $AUC = 0.88$ for the classification $ADHD$, as shown in Figure 5.12d. In contrast, the stacked LSTM has obtained $AUC = 0.62$ depicted in Figure 5.12c, which has less value when comparing the results of AUC with $BLSTM$. As a result, the stacked model $LSTM$ behaves less on average compared to the proposed modified model $BLSTM$. We took the $(p - value < 0.05)$ into account while estimating the AUC. Decision criteria are inferred from the demonstrated ROC curves.

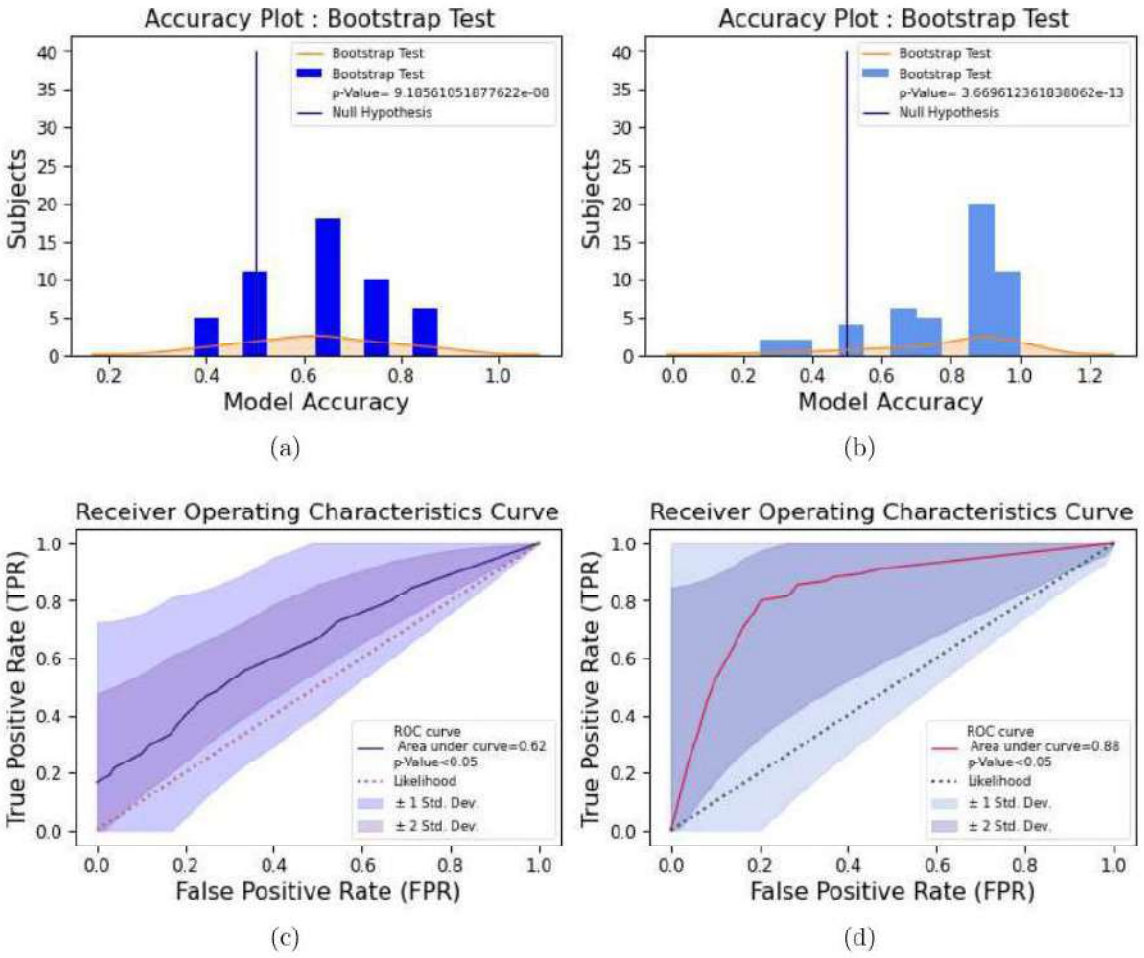

Figure 5.12: Performance of LSTM models and ROC curve measure (a) Stacked LSTM (b) Modified BLSTM.(c)AUC : Stacked LSTM, (d) AUC : Bidirectional LSTM

Evaluation Metrics

The performance metrics of both models are determined on the basis of resting state $fMRI$ data from Allen's atlas. When classifying $ADHD$ subjects with healthy controls in the basic classification task, the accuracy is determined by the type of classifier that has been used for measurement. All data $rs-fMRI$ are classified into two classes according to the proposed approach, which also classifies subjects directly into four categories such as true positive (TP), true negative (TN), false positive (FP) and false negative (FN). The following measurements can be used to calculate the different performance evaluation

metrics:

$$Sensitivity = \frac{TP}{TP + FN} \tag{5.1}$$

$$Precision = \frac{TP}{TP + FP} \tag{5.2}$$

$$F1 - Score = \frac{TP}{TP + \frac{1}{2}(FP + FN)} \tag{5.3}$$

$$Accuracy = \frac{TP + TN}{(TP + FP) + (TN + FN)} \tag{5.4}$$

The comparison of the stacked LSTM model and the proposed enhanced BLSTM is presented in Table 5.9 and AUC is shown in Figure 5.12 c and Figure 5.12 d.

5.5 Comparative Analysis with the other State-of-the-art Methods

Furthermore, we had compared the proposed modified $BLSTM$ with the other end-to-end techniques, such as $4D - CNN - LSTM$, $LSTM$, $MLP + CNV$, and $3D - CNN$. Table 5.10 displays the comprehensive comparison. To enhance classification performance using the $rs - fMRI$ data, these models have taken into account several preprocessing techniques. However, significant classification performance is achieved by the proposed modified BLSTM structure compared to another end-to-end model. Compared to existing models, the modified proposed $BLSTM$ achieved a significantly better accuracy of 87.50% and AUC of 0.88 in the classification of $ADHD$.

Dvornek et al. [99] obtained the accuracy, however,they classified ASD using the behavioral features and $rs - fMRI$ obtained from the ABIDE dataset. When classifying

Table 5.9: Performance metrics of the proposed modified BLSTM and Stacked LSTM models

	Performance Metrics					
Model	**Accu (%)**	**Sens**	**Prec**	**F1-Score**	**AUC**	**p-value**
Modified BLSTM	87.50	0.7647	0.8125	0.7878	0.88	3.66E-13
Stacked LSTM	75.00	0.6250	0.6666	0.6667	0.62	9.18E-08

Table 5.10: Comparison of the proposed modified BLSTM model with the other State-of-Art methods.

Existing Methods	**Model**	**Accuracy (%)**	**AUC (%)**	**Sensitivity (%)**	**t-test** $(p-value)$
Dvornek et al. [99]	LSTM	70.01	–	–	$p < 0.1$
Dvornek et al. [14]	LSTM	68.50	–	–	$p < 0.05$
Liu et al. [230]	MLP+CNV	78.00	–	–	–
Mao et al. [157]	4D-CNN-LSTM	71.30	80	73.2	–
Vu et al. [155]	3D-CNN	78.50	–	–	$p < 0.041$
Proposed Method	**Modified BLSTM**	**87.50**	**88**	**76.47**	$p < 0.05$

European American children with ADHD in this study, Liu et al. [230] used 262 healthy control children and 89 instances of the $ADHD$ disorder. Mao et al. [157] utilize ADHD-200 dataset for the identification of the disorder in the children. Vu et al. [155] evaluated the feature maps that are produced neural activity using a distinct open-access dataset obtained from the Human Connectome Project.

5.6 MobileNet-2D-CNN for MS classification

The proposed model detects and evaluates the classification of multiple sclerosis, which is present in the images MRI. Our model produced an accuracy of 98.15%. Since the

data set used in this study is gray images, therefore, the value of pixels from the MRI images is between 0 and 255. We have visualized the hidden layer gradient images, MS classification, and performance of the proposed model. The visualization of the MRI images shows how perfectly the proposed model extracts the characteristics for the MS classification.

5.6.1 Grad-CAM Visualization

The proposed $MobileNet$–$2D-CNN$ architecture is trained to produce heat maps from input MRI images. These heat maps detect the location of the MS lesion on the MRI image as shown in Figure 5.13. The heat maps generated from the convolutional layer use a single input channel due to grayscale images MRI. Here, the convolutional layer considers the weighted average output. In each channel, the feature map uses the weight in the Fully Connected layer. $Softmax$ layer performs the computation for class prediction of heat maps.

The output of a gradient of the $Softmax$ layer with respect to each channel forms a feature map of the specific layer that shows a gradient of the respective output channel. We have obtained feature maps generated from each activated layer as per Table. These gradient feature maps of MRI images are fed into the Global Average Pooling layer GAP) that considers the size of the MRI image tensor as $(5 \times 5 \times 32)$ and performs the average across the (5×5) convolution. The average value of each of the input channels generates one output channel, i.e. a one-dimensional tensor with 32 images. These weighted feature maps $2D$ are generated by the GAP layer, which is used as a heat map of an MRI image.

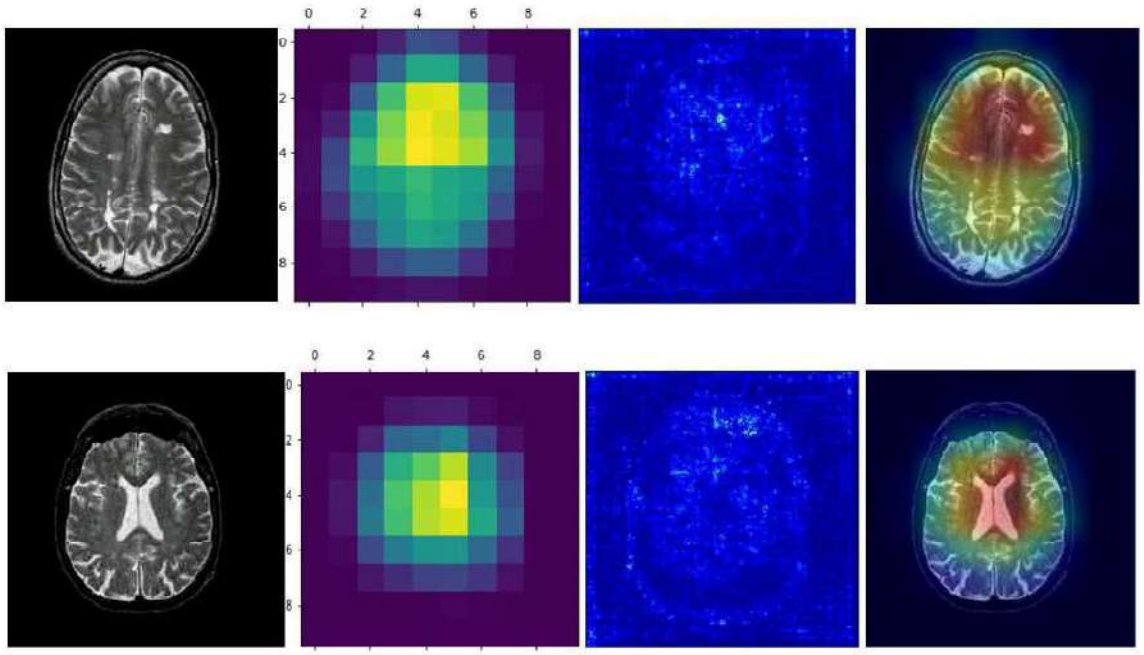

Figure 5.13: Visualization of Multiple Sclerosis affected Vs. Healthy MRI image size (224×224) on the Proposed model (a)Class activation map of Multiple Sclerosis (b) Class activation map for Healthy Brain MRI.

Table 5.11: Generated Feature Map from activation channels.

Activation Layer	**No. of Feature Map**
Mobilenet_1.00_224	32
Conv2d	128
Batch_Normalization_1	256
Max_Pooling2d _1	512
GlobalAveragePooling2D	512

5.6.2 Classification of MS Lesion

The proposed model predicts the class label, as shown in Figure 5.14. The classification process is applied to a preprocessed data set that consists of 475 MRI images, including healthy controls affected by MS. The combined data set MRI is divided into training and testing purposes with a ratio $80:20$, and 5% of the training data set has been used for validation purposes in the proposed model. The $2D-CNN$ segment of the proposed model classifies MS lesions. Figure 5.14 shows the detection of MS lesions from the MRI

image training and testing dataset.

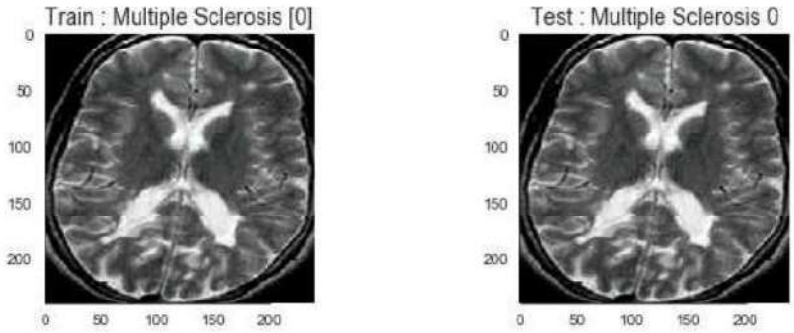

Figure 5.14: Classified MS affected brain MRI

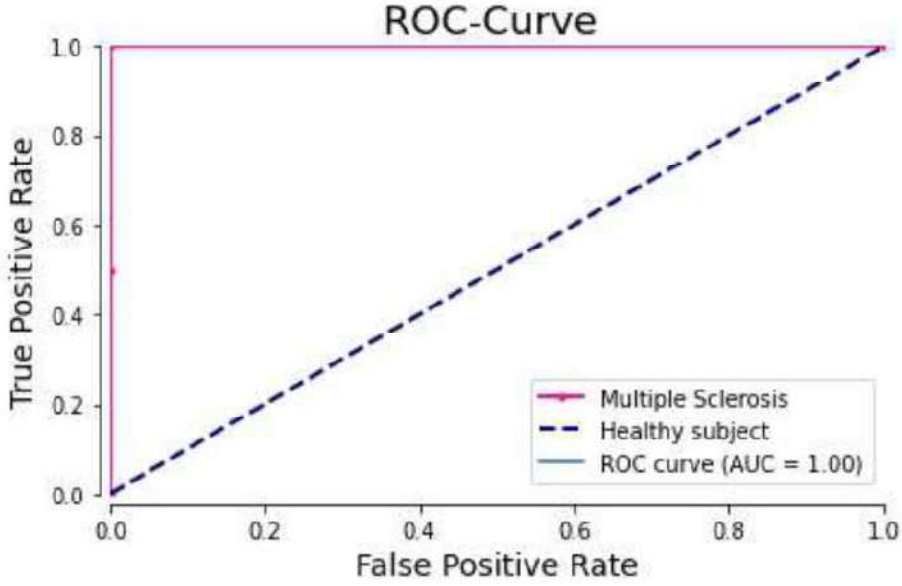

Figure 5.15: AUC for MS-affected brain MRI

5.6.3 Model Evaluation

In binary classification, the calculated probability determines the expected classes based on the continuous variable. Probability is classified as positive if the *computed probabilities* > *threshold value* otherwise it is negative. The classification performance of the proposed model is measured using the area under the curve (AUC) to determine how effectively the proposed model performs in classification. The receiver operating characteristic curve

(ROC) computes the area under the ROC curve. ROC curve is created between the true positive rate and the false positive rate, where the AUC is in the range between 0.5 and 1.0. It can be interpreted as the probability that an MS affected subject with a higher test value will be selected at random, rather than a random selection of healthy individuals. The total efficacy of the classification model is measured by the value AUC. The suggested MobileNet-2D-CNN classifier is shown in Figure. 5.15 with an AUC of 1.00. It shows how effectively the proposed model performs when applied to MRI image data, which are perfectly classified. An orange curve that extends over the threshold diagonal line and from the bottom left to the top right depicts a class of multiple sclerosis.

CHAPTER 6

DISCUSSION AND CONCLUSION

6.1 Summary

The primary objective of the current study was to analyze the implementation of deep learning techniques in the characteristics of fMRI with the objective of classifying brain activity and disorder in two distinct contexts, such as task-based fMRI and rs-fMRI. In both, the challenge included various stages, namely edge detection, neural activity, MRI saliency map generation, and classification of brain disorders.

Preprocessing fMRI data remains an important challenge; thus, here we carefully examine the brain activity signal using fMRI data. The brain needs oxygen to be maintained both structurally and functionally. When measuring human brain activity with fMRI after performing a particular task to identify a region, it is quite helpful. Neural activity under different conditions using the *BOLD* approach and signals to analyze the measurement Through data-driven experiments and multiscale brain parcellation, the present work is based on the Functional Connectome Project. Each fMRI data set had adjustments for the variation in acquisition time between slices, and the components of rigid-body motion were determined for each time frame. ROI provides signal estimation, activation, and

cluster decision making for voxels. The ROI selection method may have implications for data interpretation. As mentioned in Section 1.5 edge detection techniques for MRI analysis and classification are useful for determining the edge; they focus on the edge detection operators of Laplacian, Sobel, and Prewitt. The experimental achievement demonstrates the proposed technique.

In this work, we developed a useful computational method that signifies a unique approach to the study of useful networks in $fMRI$, which generates the spatial arrangement from BOLD signals that are present in all individuals after seeing an animated movie of $fMRI$. Using the $fMRI$ time series, calculate the voxel variance and the connectivity measure of function. To provide data on the functional significance of the white matter constituents that have been found, it is necessary to measure the possible contribution of enormous white matter networks while performing challenging tasks. The spatial structure of white matter connections is identified via time-series-based white matter activation. The general results of the current study show how the functional connection has changed.

Our demonstration indicates that the global signal fluctuations are derived from the white matter along with the CSF time series since each voxel has a different stimulus, and this is the case with all voxels. Variations in blood flow and BOLD signals are closely linked. The fluctuation of the BOLD signal in neural activity is used to assess functional connectivity; despite this, there is a correlation between brain activity and the hemodynamic response. fMRI-based spontaneous activity demonstrates the procedure by which the brain processes stimuli. Taking into account the enormous amount of voxel responses

and signals from $3D - fMRI$ images According to the voxel signal extracted from the fMRI data, the activation patterns in the original fMRI image were analyzed using a proposed $2D - CNN$ model & focusing on the state-of-the-art method for neural activity in fMRI classification with a validation of 85. 3%. The feature maps were obtained after applying this 2D-CNN model, which displays all 128 two-dimensional fMRI images.

Although the method we proposed is suitable for saliency maps, we discovered that it continuously covers saliency techniques when it becomes necessary to distinguish between a smaller number of classes. In the case of fMRI images, it might be useful to distinguish between an fMRI image that is healthy and one that has Alzheimer's. We are working with ImageNet weight in the proposed method for more than two classes. In this work, we implemented the integrated gradient corresponding to a VGG-16 model; it explains the Smooth Gradient approach, as well as the distinction that exists between the stimulus and baseline, which removes saliency map noise.

In order to assess a brain disorder, functional connectivity analysis is one of the prescribed approaches that specifies the spatiotemporal relationship between neurophysiological activities that are physically distant. In this study, we observed $(rs - fMRI)$ as an essential resource for analyzing brain images and assessing ADHD. Every active RSN voxel has been used in the proposed modified BLSTM architecture, which chooses the distinctive features that describe the time-series fMRI images belonging to the relevant voxel. The model is subsequently trained using these data to classify ADHD. The classifier's performance metrics indicate that the proposed BLSTM model achieves a successful accuracy of 87.50% in classification as well, and the F1 score maintains the equilibrium

between sensitivity and precision. Lastly, Table 4.9 presents a comparison between the proposed approach and other current state-of-the-art techniques. According to the acquired comparison statistics, the proposed approach works better than the other strategy.

6.2 Limitations

It is important to recognize some limitations for future work. Because fMRI research is expensive to conduct and the methodology of research is challenging, gathering fMRI image samples is another challenging issue. In the edge detection of MRI, an irregular region can be identified using the Laplace, Sobel, and Prewitt detection methods inside the specific region of the brain. When using the Laplacian method, due to the smaller kernel matrix, some noise is present in the intensities. The edge detection technique is insufficient to manage noise. The BOLD signal indicates the spatiotemporal structure of the functional network of fMRI.We argue that fMRI is used for the development of frameworks that explain how the brain functions, which are based on knowledge of the connections and structure of the brain. Currently, BOLD fMRI is the most effective technology available. Still, an essential question has to be addressed: What does the term "neural activity" certainly mean? The volume of the voxel directly affects how the BOLD signal changes. The voxel volume is visibly affected by spatial resolution and is usually adjusted by varying the gradient intensity of the spatial encoding. A voxel in fMRI usually contains hundreds of thousands of neurons, and a blood-flow response is caused by some portion of the aforementioned neurons activating. Typically, variations in voxel volume have a minimal impact on noise. However, there is a direct correlation between the volume of the voxel and the intensity of the signal. Random signal fluctuations

that affect fMRI time-course datasets are the result of several physiological processes not exactly connected to the functional region. The BOLD response, which is correlated with the number of active neurons, has not been well understood. Deep learning techniques such as CNN and RNN are becoming more and more common in neuroimaging. As mentioned in Tables 2.2 and 2.3 in previous studies, brain disorders and identification were performed and the diagnosis was performed based on the application of fMRI images to various CNN architectures. If CNN fails to learn, it may not be possible to gain any useful features at all. To develop a more accurate decoding architecture, reconstructing related sensory information using fMRI data employing deep learning remains susceptible to various challenges. Even though our proposed 2D CNN model has demonstrated exceptional performance in classifying neural activity, there are several problems that still require consideration, emphasizing the complexities and challenges of determining the results because of calculations that are particularly non-linear, particularly in terms of data overfitting. To solve the binary classification and detect whether or not a subject had Alzheimer's disease, we demonstrated the application of VGG16 models and techniques for identifying saliency regions in MRI images. The major challenge of the study was to find a solution for the interpretability issue with pre-trained network results when it came to fMRI images. In another experiment, we used rs-fMRI for the classification of ADHD and used an LSTM-based model. Interpretation of the RSN is much better possible, and it is crucial to resolve the problems and challenges that occur during preprocessing in the RSN-activated multiple for classification.

6.3 Future Direction

The primary objective of future research will be to overcome these limitations. An additional possibility for expansion would be to investigate functional connectivity; this explains the correlation pattern of the fMRI time series. In further studies, it would be stimulating and feasible to investigate RSN in other contexts using attention networks. Functional connection within the brain network has emerged as one of the main objectives of neuroimaging studies. It is possible to improve the standards and varieties of fMRI image reconstruction; hence, it is essential to enhance the feature extraction capabilities of deep learning models for fMRI data. The state-of-the-art model is now functioning. As the quantity of high-dimensional data in the fMRI datasets keeps growing, manually implementing aspects is not the way of the future; however, it is important to comprehend other data-driven functionalities. Taking into account the substantial variation within FC, future research will use constant upgrading across participants and time frames, including convolutional layers. In the future, the identification of ADHD,we anticipate that a more comprehensive ADHD biosignal database will soon be available to the researcher. Brain areas that are more active when people are at rest than when they are participating in activities with an external focus. When directed tasks such as watching a movie are in progress, the default mode network is also operational. The cognitive processes that are employed during recalling memories may benefit from default network.In the future, the deep learning model can be used for the observed irregular network structure features classification in individuals suffering from neurodevelopmental disorders such as ADHD. In order to more accurately analyze the cognitive features of ADHD patients, we intend to create increasingly intricate and sophisticated cognitive models. This will

facilitate a deeper comprehension of the impacts of exercise programs on various individuals.Potentially predictable fluctuations in temporal fluctuation in functional network connectivity that could describe abnormal neurological activity could be the subject of future research. The state-of-the-art method for the classification of neural activity will be determined by future researchers with the help of Table 1.2. When using deep learning models to obtain neural activity detection and classification in a particular brain region, computational analysis requirements play a major role. While the findings of this research indicate a pattern of neural activity in saliency map in fMRI,future research should yield much greater accuracy.

LIST OF PUBLICATIONS

Journals

1. Saurabh, S. and Gupta, P.K. Deep Learning-Based Modified Bidirectional LSTM Network for Classification of ADHD Disorder. Arab J Sci Eng (2023). **(SCI Indexed, IF = 2.9)**

   https://doi.org/10.1007/s13369-023-07786-w.

2. Saurabh, S. and P. K. Gupta (2023). Functional Network of Neurocognitive Development in Correlations of BOLD Signals. J. Phys.: Conf. Ser. 2570 012027. **(SCOPUS Indexed, IF = 0.21)**

   DOI 10.1088/1742-6596/2570/1/012027

3. Saurabh, S., and Gupta, P.K. (2023). Transfer Learning Model on Neurodevelopmental fMRI Images for Classification of Neural Activation. Cognitive Neurodynamics. **(Communicated, SCI Indexed, IF = 3.7)**

4. Saurabh, S., and Gupta, P.K. (2022). Detection and Classification of Multiple Sclerosis from Brain MRIs by using MobileNet 2D-CNN Architecture. Computación y Sistemas. **(Communicated, SCOPUS Indexed, IF = 0.6)**

Conferences

1. Saurabh, S., Gupta, P.K. (2022). "2D-CNN Model for Classification of Neural Activity Using Task-Based fMRI," In: Singh, M., Tyagi, V., Gupta, P.K., Flusser, J., Ören, T. (eds) Advances in Computing and Data Sciences. ICACDS 2022. Communications in Computer and Information Science, vol 1613. Springer, Cham. **(SCOPUS Indexed)**
   https://doi.org/10.1007/978-3-031-12638-3_17

2. Saurabh, S., Gupta, P.K. (2022). "Non-Linear behavior of CNN model interpretation using Saliency Map," 2022 Seventh International Conference on Parallel, Distributed and Grid Computing (PDGC), Solan, Himachal Pradesh, India, 2022, pp. 733-738, **(SCOPUS Indexed)**
   doi: 10.1109/PDGC56933.2022.10053135.

3. Saurabh, S., Gupta, P.K. (2021). "Functional Brain Image Clustering and Edge Analysis of Acute Stroke Speech Arrest MRI". IC3-2021: Proceedings of the 2021 Thirteenth International Conference on Contemporary Computing, Pages 234–240 **(SCOPUS Indexed,)**
   https://doi.org/10.1145/3474124.3474207.

REFERENCES

[1] S. Ogawa, T.-M. Lee, A. R. Kay, and D. W. Tank, "Brain magnetic resonance imaging with contrast dependent on blood oxygenation." *proceedings of the National Academy of Sciences*, vol. 87, no. 24, pp. 9868–9872, 1990.

[2] H. Greenspan, B. Van Ginneken, and R. M. Summers, "Guest editorial deep learning in medical imaging: Overview and future promise of an exciting new technique," *IEEE transactions on medical imaging*, vol. 35, no. 5, pp. 1153–1159, 2016.

[3] R. Damadian, M. Goldsmith, and L. Minkoff, "Nmr in cancer: Xvi. fonar image of the live human body," *Physiological chemistry and physics*, vol. 9, no. 1, pp. 97—100, 108, 1977.

[4] V. Fritsch, B. Da Mota, G. Varoquaux, V. Frouin, E. Loth, J.-B. Poline, and B. Thirion, "Robust group-level inference in neuroimaging genetic studies," in *2013 International Workshop on Pattern Recognition in Neuroimaging*, 2013, pp. 21–24.

[5] A. Castiglione, A. D. Santis, R. Pizzolante, A. Castiglione, V. Loia, and F. Palmieri, "On the protection of fmri images in multi-domain environments," in *2015 IEEE 29th International Conference on Advanced Information Networking and Applications*, 2015, pp. 476–481.

[6] A. Castiglione, R. Pizzolante, F. Palmieri, B. Masucci, B. Carpentieri, A. D. Santis, and A. Castiglione, "On-board format-independent security of functional magnetic resonance images," *ACM Transactions on Embedded Computing Systems (TECS)*, vol. 16, no. 2, pp. 1–15, 2017.

[7] R. Pizzolante, A. Castiglione, B. Carpentieri, R. Contaldo, G. D'Angelo, and F. Palmieri, "A machine learning-based memory forensics methodology for tor

browser artifacts," *Concurrency and Computation: Practice and Experience*, vol. 33, no. 23, p. e5935, 2021.

[8] Z. Akkus, A. Galimzianova, A. Hoogi, D. Rubin, and B. J. Erickson, "Deep learning for brain mri segmentation: State of the art and future directions," *Journal of Digital Imaging*, vol. 30, pp. 449 – 459, 2017. [Online]. Available: https://api.semanticscholar.org/CorpusID:4578542

[9] Y. Ding, R. Acosta, V. Enguix, S. Suffren, J. Ortmann, D. Luck, J. Dolz, and G. A. Lodygensky, "Using deep convolutional neural networks for neonatal brain image segmentation," *Frontiers in Neuroscience*, vol. 14, 2020. [Online]. Available: https://www.frontiersin.org/articles/10.3389/fnins.2020.00207

[10] S. Jain and A. Huth, "Incorporating context into language encoding models for fmri," in *Advances in Neural Information Processing Systems*, S. Bengio, H. Wallach, H. Larochelle, K. Grauman, N. Cesa-Bianchi, and R. Garnett, Eds. Curran Associates, Inc.

[11] T. Horikawa and Y. Kamitani, "Generic decoding of seen and imagined objects using hierarchical visual features," *Nature Communications*, vol. 8, 10 2015.

[12] R. J. Meszlényi, K. Buza, and Z. Vidnyánszky, "Resting state fmri functional connectivity-based classification using a convolutional neural network architecture," *Frontiers in Neuroinformatics*, vol. 11, 2017.

[13] Z. C. Lipton, "A critical review of recurrent neural networks for sequence learning," *CoRR*, vol. abs/1506.00019, 2015. [Online]. Available: http://arxiv.org/abs/1506.00019

[14] N. Dvornek, P. Ventola, K. Pelphrey, and J. Duncan, "Identifying autism from resting-state fmri using long short-term memory networks," vol. 10541, 09 2017, pp. 362–370.

[15] X. Wang, X. Liang, Y. Zhou, Y. Wang, J. Cui, H. Wang, Y. Li, B. Nguchu, and B. Qiu, "Decoding and mapping task states of the human brain via deep learning," *Hum Brain Mapp.*, vol. 41, no. 6, p. 1505–1519, 2020.

[16] R. Liu, Z.-a. Huang, M. Jiang, and K. C. Tan, "Multi-lstm networks for accurate classification of attention deficit hyperactivity disorder from resting-state fmri data," in *2020 2nd International Conference on Industrial Artificial Intelligence (IAI)*, 2020, pp. 1–6.

[17] C. Wachinger, M. Reuter, and T. Klein, "Deepnat: Deep convolutional neural network for segmenting neuroanatomy," *NeuroImage*, vol. 170, pp. 434–445, 2018.

[18] J. Kawahara, C. J. Brown, S. P. Miller, B. G. Booth, V. Chau, R. E. Grunau, J. G. Zwicker, and G. Hamarneh, "Brainnetcnn: Convolutional neural networks for brain networks; towards predicting neurodevelopment," *NeuroImage*, vol. 146, pp. 1038–1049, 2017.

[19] Y. Du, Z. Fu, and V. D. Calhoun, "Classification and prediction of brain disorders using functional connectivity: Promising but challenging," *Frontiers in Neuroscience*, vol. 12, p. 525, 2018.

[20] Y. Yu, X. Si, C. Hu, and J. Zhang, "A review of recurrent neural networks: Lstm cells and network architectures," vol. 31, no. 7, 2019.

[21] A. Graves and J. Schmidhuber, "Framewise phoneme classification with bidirectional lstm and other neural network architectures," *Neural Networks*, vol. 18, no. 5, pp. 602–610, 2005.

[22] S. Vieira, W. H. Pinaya, and A. Mechelli, "Using deep learning to investigate the neuroimaging correlates of psychiatric and neurological disorders: Methods and applications," *Neuroscience & Biobehavioral Reviews*, vol. 74, pp. 58–75, 2017.

[23] M. Brant-Zawadzki, G. Fein, C. Dyke, R. Kiernan, L. Davenport, and J. de Groot, "Mr imaging of the aging brain: Patchy white-matter lesions and dementia," *AJNR. American journal of neuroradiology*, vol. 6, pp. 675–682, 09 1985.

[24] S. Olaf, "The human connectome: a complex network," *Annals of the New York Academy of Sciences*, vol. 1224, no. 1, pp. 109–125, 2011.

[25] M. Boaventura, J. Sastre-Garriga, A. Garcia-Vidal, A. Vidal-Jordana, D. Quartana, R. Carvajal, C. Auger, M. Alberich, M. Tintoré, Àlex Rovira, X. Montalban, and

D. Pareto, "T1/t2-weighted ratio in multiple sclerosis: A longitudinal study with clinical associations," *NeuroImage: Clinical*, vol. 34, p. 102967, 2022.

[26] M. Glasser, M. Goyal, T. Preuss, M. Raichle, and D. Van Essen, "Trends and properties of human cerebral cortex: Correlations with cortical myelin content," *NeuroImage*, vol. 93, pp. 165–175, 2014.

[27] P. A. Bandettini and E. T. Bullmore, "Endogenous oscillations and networks in functional magnetic resonance imaging," *Human Brain Mapping*, vol. 29, no. 7, p. 737–739, 2008.

[28] Y. Wang and Y. Guo, "A hierarchical independent component analysis model for longitudinal neuroimaging studies," *NeuroImage*, vol. 189, pp. 380–400, 2019.

[29] B. Biswal, F. Yetkin, V. Haughton, and J. Hyde, "Functional connectivity in the motor cortex of resting human brain using echo-planar mri," *Magnetic resonance in medicine*, vol. 34, no. 4, pp. 537–541, 1995.

[30] A. Arieli, A. Sterkin, A. Grinvald, and A. Aertsen, "Dynamics of ongoing activity: explanation of the large variability in evoked cortical responses," *Science (New York, N.Y.)*, vol. 273, no. 5283, p. 1868—1871, 1996.

[31] D. A. Leopold and A. Maier, "Ongoing physiological processes in the cerebral cortex," *NeuroImage*, vol. 62, no. 4, pp. 2190–2200, 2012.

[32] X. Shen, X. Papademetris, and R. Constable, "Graph-theory based parcellation of functional subunits in the brain from resting-state fmri data," *NeuroImage*, vol. 50, no. 3, pp. 1027–1035, 2010.

[33] S. M. Plis, D. R. Hjelm, R. Salakhutdinov, E. A. Allen, H. J. Bockholt, J. D. Long, H. J. Johnson, J. S. Paulsen, J. A. Turner, and V. D. Calhoun, "Deep learning for neuroimaging: a validation study," *Frontiers in Neuroscience*, vol. 8, p. 229, 2014.

[34] H. Yang, J. Zhang, Q. Liu, and Y. Wang, "Multimodal mri-based classification of migraine: using deep learning convolutional neural network," *BioMedical Engineering OnLine*, vol. 17, p. 138, 2018.

[35] K. J. Friston, A. P. Holmes, C. Price, C. Büchel, and K. Worsley, "Multisubject fmri studies and conjunction analyses," *Neuroimage*, vol. 10, no. 4, pp. 385–396, 1999.

[36] P. Mansfield, "Multiplanar image formation using nmr spin echos," *Journal of Physics C: Solid State Physics*, vol. 10, p. L55, 2001.

[37] P. Mansfield, P. R. Harvey, and M. K. Stehling, "Echo-volumar imaging," *Magnetic Resonance Materials in Physics, Biology and Medicine*, vol. 2, pp. 291–294, 1994.

[38] M. Greicius, K. Supekar, V. Menon, and R. Dougherty, "Resting-state functional connectivity reflects structural connectivity in the default mode network," *Cereb Cortex*, vol. 19, pp. 72–8, 2008.

[39] P. Hagmann, L. Cammoun, X. Gigandet, R. Meuli, C. Honey, V. Wedeen, and O. Sporns, "Mapping the structural core of human cerebral cortex," *PLoS biology*, vol. 6, no. 7, p. e159, 2008.

[40] J. Vincent, G. Patel, M. Fox, A. Snyder, J. Baker, D. Van Essen, J. Zempel, L. Snyder, M. Corbetta, and M. Raichle, "Intrinsic functional architecture in the anesthetized monkey brain," *Nature*, vol. 447, no. 7140, pp. 83–6, 2007.

[41] K. Zilles, N. Palomero-Gallagher, C. Grefkes, F. Scheperjans, C. Boy, K. Amunts, and A. Schleicher, "Architectonics of the human cerebral cortex and transmitter receptor fingerprints: reconciling functional neuroanatomy and neurochemistry," *European Neuropsychopharmacology*, vol. 12, no. 6, pp. 587–599, 2002.

[42] A. Toga, P. Thompson, S. Mori, K. Amunts, and K. Zilles, "Towards multimodal atlases of the human brain," *Nature reviews. Neuroscience*, vol. 7, no. 12, pp. 952–66, 2007.

[43] T. Knösche and M. Tittgemeyer, "The role of long-range connectivity for the characterization of the functional–anatomical organization of the cortex," *Frontiers in systems neuroscience*, vol. 5, p. 58, 07 2011.

[44] C. Destrieux, B. Fischl, A. Dale, and E. Halgren, "Sulcal depth-based anatomical parcellation of the cerebral cortex," *Neuroimage*, vol. 47, 07 2009.

[45] K. Amunts, A. Schleicher, and K. Zilles, "Cytoarchitecture of the cerebral cortex—more than localization," *NeuroImage*, vol. 37, no. 4, pp. 1061–1065, 2007.

[46] S. Geyer, M. Weiss, K. Reimann, G. Lohmann, and R. Turner, "Microstructural parcellation of the human cerebral cortex – from brodmann's post-mortem map to in vivo mapping with high-field magnetic resonance imaging," *Frontiers in Human Neuroscience*, vol. 5, no. 19, 2011.

[47] R. B. Tootell and S. Nasr, "Columnar segregation of magnocellular and parvocellular streams in human extrastriate cortex," *Journal of Neuroscience*, vol. 37, no. 33, pp. 8014–8032, 2017.

[48] K. Amunts and K. Zilles, "Architectonic mapping of the human brain beyond brodmann," *Neuron*, vol. 88, no. 6, pp. 1086–1107, 2015.

[49] R. Guillery, "Brodmann's'localisation in the cerebral cortex'," *J Anat.*, p. 196(Pt 3):493–496, 2000.

[50] R. E. Passingham, K. E. Stephan, and R. Kötter, "The anatomical basis of functional localization in the cortex," *Nature Reviews Neuroscience*, vol. 3, no. 8, pp. 606–616, 2002.

[51] S. Eickhoff, B. T. Yeo, and S. Genon, "Imaging-based parcellations of the human brain," *Nature Reviews Neuroscience*, vol. 19, no. 11, pp. 672–686, 2018.

[52] R. C. Craddock, G. James, P. E. Holtzheimer III, X. P. Hu, and H. S. Mayberg, "A whole brain fmri atlas generated via spatially constrained spectral clustering," *Human Brain Mapping*, vol. 33, no. 8, pp. 1914–1928, 2012.

[53] X. Shen, F. Tokoglu, X. Papademetris, and R. Constable, "Groupwise whole-brain parcellation from resting-state fmri data for network node identification," *NeuroImage*, vol. 82, p. 403–415., 2013.

[54] N. S. W. G. B. K. C. J. V. A. L. T. M. F. S. B. Power JD, Cohen AL and P. SE., "Functional network organization of the human brain," *Neuron*, vol. 72, no. 4, pp. 665–78, 2011.

[55] B. T. Yeo, F. Krienen, J. Sepulcre, M. Sabuncu, D. Lashkari, M. Hollinshead, J. Roffman, J. Smoller, L. Zollei, J. Polimeni, B. Fischl, H. Liu, and R. Buckner, "The organization of the human cerebral cortex estimated by functional correlation," *Journal of neurophysiology*, vol. 106, no. 3, pp. 1125–65, 2011.

[56] X. Shen, F. Tokoglu, X. Papademetris, and R. Constable, "Groupwise whole-brain parcellation from resting-state fmri data for network node identification," *NeuroImage*, vol. 82, pp. 403–415, 2013.

[57] S. Arslan and D. Rueckert, "Multi-level parcellation of the cerebral cortex using resting-state fmri," in *International Conference on Medical Image Computing and Computer-Assisted Intervention-MICCAI 2015*, vol. 9351, 2015.

[58] Q. Lin, M. D. Rosenberg, K. Yoo, T. W. Hsu, T. P. O'Connell, and M. M. Chun, "Resting-state functional connectivity predicts cognitive impairment related to alzheimer's disease," *Frontiers in aging neuroscience*, vol. 10, p. 94, 2018.

[59] O. Esteban, C. J. Markiewicz, R. W. Blair, C. A. Moodie, A. I. Isik, A. Erramuzpe, J. D. Kent, M. Goncalves, E. DuPre, M. Snyder *et al.*, "fmriprep: a robust preprocessing pipeline for functional mri," *Nature methods*, vol. 16, no. 1, pp. 111–116, 2019.

[60] L. di Qin, Z. Wang, Y. wen Sun, J. qing Wan, S. shan Su, Y. Zhou, and J. rong Xu, "A preliminary study of alterations in default network connectivity in post-traumatic stress disorder patients following recent trauma," *Brain Research*, vol. 1484, pp. 50–56, 2012.

[61] M. D. Rosenberg, E. S. Finn, D. Scheinost, X. Papademetris, X. Shen, R. T. Constable, and M. M. Chun, "A neuromarker of sustained attention from whole-brain functional connectivity," *Nature neuroscience*, vol. 19, no. 1, pp. 165–171, 2016.

[62] B. A. Seitzman, A. Z. Snyder, E. C. Leuthardt, and J. S. Shimony, "The state of resting state networks," *Topics in magnetic resonance imaging: TMRI*, vol. 28, no. 4, p. 189, 2019.

[63] B. H. Vieira, C. Rondinoni, and C. E. G. Salmon, "Evidence of regional associations between age-related inter-individual differences in resting-state functional connectivity and cortical thinning revealed through a multi-level analysis," *NeuroImage*, vol. 211, p. 116662, 2020.

[64] C. Zhou, X. Tang, W. You, X. Wang, X. Zhang, X. Zhang, and M. Yu, "Altered patterns of the fractional amplitude of low-frequency fluctuation and functional connectivity between deficit and non-deficit schizophrenia," *Frontiers in Psychiatry*, vol. 10, p. 680, 2019.

[65] J. S. Damoiseaux, S. A. Rombouts, F. Barkhof, P. Scheltens, C. J. Stam, S. M. Smith, and C. F. Beckmann, "Consistent resting-state networks across healthy subjects," *Proceedings of the national academy of sciences*, vol. 103, no. 37, pp. 13 848–13 853, 2006.

[66] A. De La Fuente, S. Xia, C. Branch, and X. Li, "A review of attention-deficit/hyperactivity disorder from the perspective of brain networks," *Frontiers in human neuroscience*, vol. 7, p. 192, 2013.

[67] R. H. Pruim, C. F. Beckmann, M. Oldehinkel, J. Oosterlaan, D. Heslenfeld, C. A. Hartman, P. J. Hoekstra, S. V. Faraone, B. Franke, J. K. Buitelaar *et al.*, "An integrated analysis of neural network correlates of categorical and dimensional models of attention-deficit/hyperactivity disorder," *Biological Psychiatry: Cognitive Neuroscience and Neuroimaging*, vol. 4, no. 5, pp. 472–483, 2019.

[68] J. Choi, B. Jeong, S. W. Lee, and H.-J. Go, "Aberrant development of functional connectivity among resting state-related functional networks in medication-naive adhd children," *PLoS One*, vol. 8, no. 12, p. e83516, 2013.

[69] A. dos Santos Siqueira, C. E. Biazoli Junior, W. E. Comfort, L. A. Rohde, J. R. Sato *et al.*, "Abnormal functional resting-state networks in adhd: graph theory and pattern recognition analysis of fmri data," *BioMed research international*, vol. 2014, 2014.

[70] D. Provencher, A. Bizeau, G. Gilbert, Y. Bérubé-Lauzière, and K. Whittingstall,

"Structural impacts on the timing and amplitude of the negative bold response," *Magnetic Resonance Imaging*, vol. 45, pp. 34–42, 2018.

[71] C. F. Beckmann, M. DeLuca, J. T. Devlin, and S. M. Smith, "Investigations into resting-state connectivity using independent component analysis," *Philosophical Transactions of the Royal Society B: Biological Sciences*, vol. 360, no. 1457, pp. 1001–1013, 2005.

[72] M. Oliveri, G. Koch, and C. Caltagirone, "Spatial–temporal interactions in the human brain," *Experimental Brain Research*, vol. 195, pp. 489–497, 2009.

[73] R. T. Thibault, M. Lifshitz, and A. Raz, "The climate of neurofeedback: scientific rigour and the perils of ideology," *Brain*, vol. 141, no. 2, pp. e11–e11, 2018.

[74] S. Yu, N. Zheng, Y. Ma, H. Wu, and B. Chen, "A novel brain decoding method: A correlation network framework for revealing brain connections," *IEEE Transactions on Cognitive and Developmental Systems*, vol. 11, no. 1, pp. 95–106, 2018.

[75] R. W. Cox, A. Jesmanowicz, and J. S. Hyde, "Real-time functional magnetic resonance imaging," *Magnetic resonance in medicine*, vol. 33, no. 2, pp. 230–236, 1995.

[76] N. K. Logothetis, "The underpinnings of the bold functional magnetic resonance imaging signal," *Journal of Neuroscience*, vol. 23, no. 10, pp. 3963–3971, 2003.

[77] K. J. Friston, A. Mechelli, R. Turner, and C. J. Price, "Nonlinear responses in fmri: the balloon model, volterra kernels, and other hemodynamics," *NeuroImage*, vol. 12, no. 4, pp. 466–477, 2000.

[78] R. B. Buxton, E. C. Wong, and L. R. Frank, "Dynamics of blood flow and oxygenation changes during brain activation: the balloon model," *Magnetic resonance in medicine*, vol. 39, no. 6, pp. 855–864, 1998.

[79] R. B. Buxton, K. Uludağ, D. J. Dubowitz, and T. T. Liu, "Modeling the hemodynamic response to brain activation," *Neuroimage*, vol. 23, pp. S220–S233, 2004.

[80] M. L. Stanley, M. N. Moussa, B. M. Paolini, R. G. Lyday, J. H. Burdette, and P. J. Laurienti, "Defining nodes in complex brain networks," *Frontiers in computational neuroscience*, vol. 7, p. 169, 2013.

[81] R. Salvador, J. Suckling, M. R. Coleman, J. D. Pickard, D. Menon, and E. Bullmore, "Neurophysiological architecture of functional magnetic resonance images of human brain," *Cerebral cortex*, vol. 15, no. 9, pp. 1332–1342, 2005.

[82] S. Achard, R. Salvador, B. Whitcher, J. Suckling, and E. Bullmore, "A resilient, low-frequency, small-world human brain functional network with highly connected association cortical hubs," *Journal of Neuroscience*, vol. 26, no. 1, pp. 63–72, 2006.

[83] K. Supekar, M. Musen, and V. Menon, "Development of large-scale functional brain networks in children," *PLoS biology*, vol. 7, no. 7, p. e1000157, 2009.

[84] K. Supekar, V. Menon, D. Rubin, M. Musen, and M. D. Greicius, "Network analysis of intrinsic functional brain connectivity in alzheimer's disease," *PLoS computational biology*, vol. 4, no. 6, p. e1000100, 2008.

[85] J. V. Hull, L. B. Dokovna, Z. J. Jacokes, C. M. Torgerson, A. Irimia, and J. D. Van Horn, "Resting-state functional connectivity in autism spectrum disorders: a review," *Frontiers in psychiatry*, vol. 7, p. 205, 2017.

[86] J. Hua, N. I. Blair, A. Paez, A. Choe, A. D. Barber, A. Brandt, I. A. L. Lim, F. Xu, V. Kamath, J. J. Pekar *et al.*, "Altered functional connectivity between sub-regions in the thalamus and cortex in schizophrenia patients measured by resting state bold fmri at 7t," *Schizophrenia research*, vol. 206, pp. 370–377, 2019.

[87] M. D. Greicius, B. Krasnow, A. L. Reiss, and V. Menon, "Functional connectivity in the resting brain: a network analysis of the default mode hypothesis," *Proceedings of the national academy of sciences*, vol. 100, no. 1, pp. 253–258, 2003.

[88] W. R. Shirer, S. Ryali, E. Rykhlevskaia, V. Menon, and M. D. Greicius, "Decoding subject-driven cognitive states with whole-brain connectivity patterns," *Cerebral cortex*, vol. 22, no. 1, pp. 158–165, 2012.

[89] F. X. Castellanos and E. Proal, "Large-scale brain systems in adhd: beyond the prefrontal–striatal model," *Trends in cognitive sciences*, vol. 16, no. 1, pp. 17–26, 2012.

[90] E. A. Allen, E. Damaraju, S. M. Plis, E. B. Erhardt, T. Eichele, and V. D. Calhoun, "Tracking whole-brain connectivity dynamics in the resting state," *Cerebral cortex*, vol. 24, no. 3, pp. 663–676, 2014.

[91] Y. Du, G. D. Pearlson, Q. Yu, H. He, D. Lin, J. Sui, L. Wu, and V. D. Calhoun, "Interaction among subsystems within default mode network diminished in schizophrenia patients: a dynamic connectivity approach," *Schizophrenia research*, vol. 170, no. 1, pp. 55–65, 2016.

[92] N. Leonardi, J. Richiardi, M. Gschwind, S. Simioni, J.-M. Annoni, M. Schluep, P. Vuilleumier, and D. Van De Ville, "Principal components of functional connectivity: a new approach to study dynamic brain connectivity during rest," *NeuroImage*, vol. 83, pp. 937–950, 2013.

[93] X. Li, D. Zhu, X. Jiang, C. Jin, X. Zhang, L. Guo, J. Zhang, X. Hu, L. Li, and T. Liu, "Dynamic functional connectomics signatures for characterization and differentiation of ptsd patients," *Human brain mapping*, vol. 35, no. 4, pp. 1761–1778, 2014.

[94] R. L. Miller, M. Yaesoubi, J. A. Turner, D. Mathalon, A. Preda, G. Pearlson, T. Adali, and V. D. Calhoun, "Higher dimensional meta-state analysis reveals reduced resting fmri connectivity dynamism in schizophrenia patients," *PloS one*, vol. 11, no. 3, p. e0149849, 2016.

[95] N. C. Dvornek, P. Ventola, K. A. Pelphrey, and J. S. Duncan, "Identifying autism from resting-state fmri using long short-term memory networks," in *Machine Learning in Medical Imaging: 8th International Workshop, MLMI 2017, Held in Conjunction with MICCAI 2017, Quebec City, QC, Canada, September 10, 2017, Proceedings 8*. Springer, 2017, pp. 362–370.

[96] G. E. Hinton, S. Osindero, and Y.-W. Teh, "A fast learning algorithm for deep belief nets," *Neural computation*, vol. 18, no. 7, pp. 1527–1554, 2006.

[97] W. Yan, H. Zhang, J. Sui, and D. Shen, "Deep chronnectome learning via full bidirectional long short-term memory networks for mci diagnosis," in *Medical Image Computing and Computer Assisted Intervention–MICCAI 2018: 21st International*

Conference, Granada, Spain, September 16-20, 2018, Proceedings, Part III 11, 2018, pp. 249–257.

[98] L.-L. Zeng, H. Wang, P. Hu, B. Yang, W. Pu, H. Shen, X. Chen, Z. Liu, H. Yin, Q. Tan *et al.*, "Multi-site diagnostic classification of schizophrenia using discriminant deep learning with functional connectivity mri," *EBioMedicine*, vol. 30, pp. 74–85, 2018.

[99] N. C. Dvornek, P. Ventola, and J. S. Duncan, "Combining phenotypic and resting-state fmri data for autism classification with recurrent neural networks," in *2018 IEEE 15th International Symposium on Biomedical Imaging (ISBI 2018)*. IEEE, 2018, pp. 725–728.

[100] D. Durstewitz, G. Koppe, and A. Meyer-Lindenberg, "Deep neural networks in psychiatry," *Molecular psychiatry*, vol. 24, no. 11, pp. 1583–1598, 2019.

[101] C. Davatzikos, A. Sotiras, Y. Fan, M. Habes, G. Erus, S. Rathore, S. Bakas, R. Chitalia, A. Gastounioti, and D. Kontos, "Precision diagnostics based on machine learning-derived imaging signatures," *Magnetic resonance imaging*, vol. 64, pp. 49–61, 2019.

[102] R. Hecht-Nielsen, "Theory of the backpropagation neural network," in *Neural networks for perception*. Elsevier, 1992, pp. 65–93.

[103] M. Dalto, J. Matuško, and M. Vašak, "Deep neural networks for ultra-short-term wind forecasting," in *2015 IEEE international conference on industrial technology (ICIT)*. IEEE, 2015, pp. 1657–1663.

[104] G. E. Hinton, "Training products of experts by minimizing contrastive divergence," *Neural computation*, vol. 14, no. 8, pp. 1771–1800, 2002.

[105] S. Plis, D. Hjelm, R. Salakhutdinov, E. Allen, H. Bockholt, J. Long, H. Johnson, J. Paulsen, J. Turner, and V. Calhoun, "Deep learning for neuroimaging: a validation study. front neurosci 8: 229," 2014.

[106] D. Kuang and L. He, "Classification on adhd with deep learning," in *2014 International Conference on Cloud Computing and Big Data*. IEEE, 2014, pp. 27–32.

[107] I. Goodfellow, J. Pouget-Abadie, M. Mirza, B. Xu, D. Warde-Farley, S. Ozair, A. Courville, and Y. Bengio, "Generative adversarial nets," *Advances in neural information processing systems*, vol. 27, 2014.

[108] P. Grnarova, K. Y. Levy, A. Lucchi, N. Perraudin, I. Goodfellow, T. Hofmann, and A. Krause, "A domain agnostic measure for monitoring and evaluating gans," *Advances in Neural Information Processing Systems*, vol. 32, 2019.

[109] A. Creswell, T. White, V. Dumoulin, K. Arulkumaran, B. Sengupta, and A. A. Bharath, "Generative adversarial networks: An overview," *IEEE signal processing magazine*, vol. 35, no. 1, pp. 53–65, 2018.

[110] Y. Guo, Y. Liu, A. Oerlemans, S. Lao, S. Wu, and M. S. Lew, "Deep learning for visual understanding: A review," *Neurocomputing*, vol. 187, pp. 27–48, 2016.

[111] Y. Hong, U. Hwang, J. Yoo, and S. Yoon, "How generative adversarial networks and their variants work: An overview," *ACM Computing Surveys (CSUR)*, vol. 52, no. 1, pp. 1–43, 2019.

[112] T. Salimans, I. Goodfellow, W. Zaremba, V. Cheung, A. Radford, and X. Chen, "Improved techniques for training gans," *Advances in neural information processing systems*, vol. 29, 2016.

[113] J. Wu, C. Zhang, T. Xue, B. Freeman, and J. Tenenbaum, "Learning a probabilistic latent space of object shapes via 3d generative-adversarial modeling," *Advances in neural information processing systems*, vol. 29, 2016.

[114] Y. Hiasa, Y. Otake, M. Takao, T. Matsuoka, K. Takashima, A. Carass, J. L. Prince, N. Sugano, and Y. Sato, "Cross-modality image synthesis from unpaired data using cyclegan: Effects of gradient consistency loss and training data size," in *Simulation and Synthesis in Medical Imaging: Third International Workshop, SASHIMI 2018, Held in Conjunction with MICCAI 2018, Granada, Spain, September 16, 2018, Proceedings 3*. Springer, 2018, pp. 31–41.

[115] Z. Zhang, X. Zhou, S. Zhao, and X. Zhang, "Semantic prior guided face inpainting," in *Proceedings of the ACM Multimedia Asia*, 2019, pp. 1–6.

[116] A. Radford, L. Metz, and S. Chintala, "Unsupervised representation learning with deep convolutional generative adversarial networks," *arXiv preprint arXiv:1511.06434*, 2015.

[117] M. Arjovsky, S. Chintala, and L. Bottou, "Wasserstein generative adversarial networks," in *International conference on machine learning*. PMLR, 2017, pp. 214–223.

[118] Y. Jiang, S. Chang, and Z. Wang, "Transgan: Two pure transformers can make one strong gan, and that can scale up," *Advances in Neural Information Processing Systems*, vol. 34, pp. 14 745–14 758, 2021.

[119] X. Mao, Q. Li, H. Xie, R. Y. Lau, Z. Wang, and S. Paul Smolley, "Least squares generative adversarial networks," in *Proceedings of the IEEE International Conference on computer vision*, 2017, pp. 2794–2802.

[120] M. Mirza and S. Osindero, "Conditional generative adversarial nets," *arXiv preprint arXiv:1411.1784*, 2014.

[121] X. Yi, E. Walia, and P. Babyn, "Generative adversarial network in medical imaging: A review," *Medical image analysis*, vol. 58, p. 101552, 2019.

[122] V. Sorin, Y. Barash, E. Konen, and E. Klang, "Creating artificial images for radiology applications using generative adversarial networks (gans)–a systematic review," *Academic radiology*, vol. 27, no. 8, pp. 1175–1185, 2020.

[123] C. Qu, Y. Zou, Q. Dai, Y. Ma, J. He, Q. Liu, W. Kuang, Z. Jia, T. Chen, and Q. Gong, "Advancing diagnostic performance and clinical applicability of deep learning-driven generative adversarial networks for alzheimer's disease," *Psychoradiology*, vol. 1, no. 4, pp. 225–248, 2021.

[124] M. E. Laino, P. Cancian, L. S. Politi, M. G. Della Porta, L. Saba, and V. Savevski, "Generative adversarial networks in brain imaging: A narrative review," *Journal of Imaging*, vol. 8, no. 4, p. 83, 2022.

[125] Y. LeCun, Y. Bengio, and G. Hinton, "Deep learning," *nature*, vol. 521, no. 7553, pp. 436–444, 2015.

[126] Y. LeCun, L. Bottou, Y. Bengio, and P. Haffner, "Gradient-based learning applied to document recognition," *Proceedings of the IEEE*, vol. 86, no. 11, pp. 2278–2324, 1998.

[127] A. Krizhevsky, I. Sutskever, and G. Hinton, "Imagenet classification with deep convolutional neural networks," *Advances in neural information processing systems*, vol. 25, 2012.

[128] A. G. Howard, M. Zhu, B. Chen, D. Kalenichenko, W. Wang, T. Weyand, M. Andreetto, and H. Adam, "Mobilenets: Efficient convolutional neural networks for mobile vision applications," *arXiv preprint arXiv:1704.04861*, 2017.

[129] M. D. Zeiler and R. Fergus, "Visualizing and understanding convolutional networks," in *Computer Vision–ECCV 2014: 13th European Conference, Zurich, Switzerland, September 6-12, 2014, Proceedings, Part I 13*. Springer, 2014, pp. 818–833.

[130] M. Tan, "rethinking model scaling for convolutional neural networks. arxiv. 2019 doi: 10.48550," *arXiv*, 2019.

[131] C. Szegedy, V. Vanhoucke, S. Ioffe, J. Shlens, and Z. Wojna, "Rethinking the inception architecture for computer vision," in *Proceedings of the IEEE conference on computer vision and pattern recognition*, 2016, pp. 2818–2826.

[132] K. He, X. Zhang, S. Ren, and J. Sun, "Deep residual learning for image recognition," in *Proceedings of the IEEE conference on computer vision and pattern recognition*, 2016, pp. 770–778.

[133] C. Szegedy, W. Liu, Y. Jia, P. Sermanet, S. Reed, D. Anguelov, D. Erhan, V. Vanhoucke, and A. Rabinovich, "Going deeper with convolutions," in *Proceedings of the IEEE conference on computer vision and pattern recognition*, 2015, pp. 1–9.

[134] K. Simonyan and A. Zisserman, "Very deep convolutional networks for large-scale image recognition," *arXiv preprint arXiv:1409.1556*, 2014.

[135] P. Nguyen, T. Tran, N. Wickramasinghe, and S. Venkatesh, "\mathtt {Deepr} :

a convolutional net for medical records," *IEEE journal of biomedical and health informatics*, vol. 21, no. 1, pp. 22–30, 2016.

[136] L. Zhang, M. Wang, M. Liu, and D. Zhang, "A survey on deep learning for neuroimaging-based brain disorder analysis," *Frontiers in neuroscience*, vol. 14, p. 779, 2020.

[137] O. Firat, E. Aksan, I. Oztekin, and F. T. Yarman Vural, "Learning deep temporal representations for fmri brain decoding," in *Machine Learning Meets Medical Imaging: First International Workshop, MLMMI 2015, Held in Conjunction with ICML 2015, Lille, France, July 11, 2015, Revised Selected Papers 1.* Springer, 2015, pp. 25–34.

[138] J. Dolz, I. B. Ayed, J. Yuan, and C. Desrosiers, "Hyperdense-net: A hyper-densely connected cnn for multi-modal image semantic segmentation," *arXiv preprint arXiv:1710.05956*, 2017.

[139] Y. LeCun, L. Bottou, Y. Bengio, and P. Haffner, "Gradient-based learning applied to document recognition," *Proceedings of the IEEE*, vol. 86, no. 11, pp. 2278–2324, 1998.

[140] F. Chollet, "Xception: Deep learning with depthwise separable convolutions," in *Proceedings of the IEEE conference on computer vision and pattern recognition*, 2017, pp. 1251–1258.

[141] G. Huang, Z. Liu, L. Van Der Maaten, and K. Q. Weinberger, "Densely connected convolutional networks," in *Proceedings of the IEEE conference on computer vision and pattern recognition*, 2017, pp. 4700–4708.

[142] J. Bernal, K. Kushibar, D. S. Asfaw, S. Valverde, A. Oliver, R. Martí, and X. Lladó, "Deep convolutional neural networks for brain image analysis on magnetic resonance imaging: a review," *Artificial intelligence in medicine*, vol. 95, pp. 64–81, 2019.

[143] M.-A. Sato, "Online model selection based on the variational bayes," *Neural computation*, vol. 13, no. 7, pp. 1649–1681, 2001.

[144] M. Agrawal and T. Thierauf, "The satisfiability problem for probabilistic ordered branching programs, eccc tr97-060 (1997)."

[145] H. Li, T. D. Satterthwaite, and Y. Fan, "Brain age prediction based on resting-state functional connectivity patterns using convolutional neural networks," in *2018 ieee 15th international symposium on biomedical imaging (isbi 2018)*, 2018, pp. 101–104.

[146] S. Sarraf and G. Tofighi, "Classification of alzheimer's disease using fmri data and deep learning convolutional neural networks," *arXiv preprint arXiv:1603.08631*, 2016.

[147] Y. Zhao, Q. Dong, S. Zhang, W. Zhang, H. Chen, X. Jiang, L. Guo, X. Hu, J. Han, and T. Liu, "Automatic recognition of fmri-derived functional networks using 3-d convolutional neural networks," *IEEE Transactions on Biomedical Engineering*, vol. 65, no. 9, pp. 1975–1984, 2017.

[148] L. Zou, J. Zheng, C. Miao, M. J. Mckeown, and Z. J. Wang, "3d cnn based automatic diagnosis of attention deficit hyperactivity disorder using functional and structural mri," *Ieee Access*, vol. 5, pp. 23 626–23 636, 2017.

[149] T. M. Mitchell, S. V. Shinkareva, A. Carlson, K.-M. Chang, V. L. Malave, R. A. Mason, and M. A. Just, "Predicting human brain activity associated with the meanings of nouns," *science*, vol. 320, no. 5880, pp. 1191–1195, 2008.

[150] P. Agrawal, D. Stansbury, J. Malik, and J. L. Gallant, "Pixels to voxels: modeling visual representation in the human brain," *arXiv preprint arXiv:1407.5104*, 2014.

[151] U. Güçlü and M. A. van Gerven, "Deep neural networks reveal a gradient in the complexity of neural representations across the ventral stream," *Journal of Neuroscience*, vol. 35, no. 27, pp. 10 005–10 014, 2015.

[152] B. A. Richards, T. P. Lillicrap, P. Beaudoin, Y. Bengio, R. Bogacz, A. Christensen, C. Clopath, R. P. Costa, A. de Berker, S. Ganguli *et al.*, "A deep learning framework for neuroscience," *Nature neuroscience*, vol. 22, no. 11, pp. 1761–1770, 2019.

[153] X. Wang, X. Liang, Y. Zhou, Y. Wang, J. Cui, H. Wang, Y. Li, B. A. Nguchu, and

B. Qiu, "Task state decoding and mapping of individual four-dimensional fmri time series using deep neural network," *arXiv preprint arXiv:1801.09858*, 2018.

[154] V. Cherukuri, T. Guo, S. J. Schiff, and V. Monga, "Deep mr brain image super-resolution using spatio-structural priors," *IEEE Transactions on Image Processing*, vol. 29, pp. 1368–1383, 2020.

[155] H. Vu, H.-C. Kim, M. Jung, and J.-H. Lee, "fmri volume classification using a 3d convolutional neural network robust to shifted and scaled neuronal activations," *NeuroImage*, vol. 223, p. 117328, 2020.

[156] M. Talo, O. Yildirim, U. B. Baloglu, G. Aydin, and U. R. Acharya, "Convolutional neural networks for multi-class brain disease detection using mri images," *Computerized Medical Imaging and Graphics*, vol. 78, p. 101673, 2019.

[157] Z. Mao, Y. Su, G. Xu, X. Wang, Y. Huang, W. Yue, L. Sun, and N. Xiong, "Spatio-temporal deep learning method for adhd fmri classification," *Information Sciences*, vol. 499, pp. 1–11, 2019.

[158] H. Wang, Y. Shen, S. Wang, T. Xiao, L. Deng, X. Wang, and X. Zhao, "Ensemble of 3d densely connected convolutional network for diagnosis of mild cognitive impairment and alzheimer's disease," *Neurocomputing*, vol. 333, pp. 145–156, 2019.

[159] F. Eitel, E. Soehler, J. Bellmann-Strobl, A. U. Brandt, K. Ruprecht, R. M. Giess, J. Kuchling, S. Asseyer, M. Weygandt, J.-D. Haynes *et al.*, "Uncovering convolutional neural network decisions for diagnosing multiple sclerosis on conventional mri using layer-wise relevance propagation," *NeuroImage: Clinical*, vol. 24, p. 102003, 2019.

[160] C. J. Wang, C. A. Hamm, L. J. Savic, M. Ferrante, I. Schobert, T. Schlachter, M. Lin, J. C. Weinreb, J. S. Duncan, J. Chapiro *et al.*, "Deep learning for liver tumor diagnosis part ii: convolutional neural network interpretation using radiologic imaging features," *European radiology*, vol. 29, pp. 3348–3357, 2019.

[161] A. M. Rauschecker, T. J. Gleason, P. Nedelec, M. T. Duong, D. A. Weiss, E. Calabrese, J. B. Colby, L. P. Sugrue, J. D. Rudie, and C. P. Hess, "Interinstitutional

portability of a deep learning brain mri lesion segmentation algorithm," *Radiology: Artificial Intelligence*, vol. 4, no. 1, p. e200152, 2021.

[162] C. Meng, K. Sun, S. Guan, Q. Wang, R. Zong, and L. Liu, "Multiscale dense convolutional neural network for dsa cerebrovascular segmentation," *Neurocomputing*, vol. 373, pp. 123–134, 2020.

[163] H. Ko, H. Chung, H. Lee, and J. Lee, "Feasible study on intracranial hemorrhage detection and classification using a cnn-lstm network," in *2020 42nd Annual International Conference of the IEEE Engineering in Medicine & Biology Society (EMBC)*, 2020, pp. 1290–1293.

[164] C.-R. Phang, F. Noman, H. Hussain, C.-M. Ting, and H. Ombao, "A multi-domain connectome convolutional neural network for identifying schizophrenia from eeg connectivity patterns," *IEEE journal of biomedical and health informatics*, vol. 24, no. 5, pp. 1333–1343, 2019.

[165] S.-C. Park, J. H. Cha, S. Lee, W. Jang, C. S. Lee, and J. K. Lee, "Deep learning-based deep brain stimulation targeting and clinical applications," *Frontiers in neuroscience*, vol. 13, p. 1128, 2019.

[166] L. Dubreuil-Vall, G. Ruffini, and J. A. Camprodon, "Deep learning convolutional neural networks discriminate adult adhd from healthy individuals on the basis of event-related spectral eeg," *Frontiers in neuroscience*, vol. 14, p. 251, 2020.

[167] F. Guilherme, W. Marina, F. C. Raphael, P. Ramon, and R. Anderson, "Alzheimer's disease detection through whole-brain 3d-cnn mri," *Frontiers in bioengineering and biotechnology*, vol. 2020, 2020.

[168] M. Dyrba, M. Hanzig, S. Altenstein, S. Bader, T. Ballarini, F. Brosseron, K. Buerger, D. Cantré, P. Dechent, L. Dobisch *et al.*, "Improving 3d convolutional neural network comprehensibility via interactive visualization of relevance maps: evaluation in alzheimer's disease," *Alzheimer's research & therapy*, vol. 13, pp. 1–18, 2021.

[169] F. Özyurt, E. Sert, E. Avci, and E. Dogantekin, "Brain tumor detection based on convolutional neural network with neutrosophic expert maximum fuzzy sure entropy," *Measurement*, vol. 147, p. 106830, 2019.

[170] Y. Wang, L. Zhang, P. Xia, P. Wang, X. Chen, L. Du, Z. Fang, and M. Du, "Eeg-based emotion recognition using a 2d cnn with different kernels," *Bioengineering*, vol. 9, no. 6, p. 231, 2022.

[171] J. A. Livezey and J. I. Glaser, "Deep learning approaches for neural decoding: from cnns to lstms and spikes to fmri," *arXiv preprint arXiv:2005.09687*, 2020.

[172] W. Huang, H. Yan, C. Wang, X. Yang, J. Li, Z. Zuo, J. Zhang, and H. Chen, "Deep natural image reconstruction from human brain activity based on conditional progressively growing generative adversarial networks," *Neuroscience bulletin*, vol. 37, pp. 369–379, 2021.

[173] U. Güçlü and M. A. Van Gerven, "Modeling the dynamics of human brain activity with recurrent neural networks," *Frontiers in computational neuroscience*, vol. 11, p. 7, 2017.

[174] S. Hochreiter and J. Schmidhuber, "Long short-term memory," *Neural computation*, vol. 9, no. 8, pp. 1735–1780, 1997.

[175] S. Hochreiter, Y. Bengio, P. Frasconi, J. Schmidhuber *et al.*, "Gradient flow in recurrent nets: the difficulty of learning long-term dependencies," 2001.

[176] A. Graves and J. Schmidhuber, "Framewise phoneme classification with bidirectional lstm and other neural network architectures," *Neural networks*, vol. 18, no. 5-6, pp. 602–610, 2005.

[177] H.-C. Yi, Z.-H. You, X. Zhou, L. Cheng, X. Li, T.-H. Jiang, and Z.-H. Chen, "Acp-dl: a deep learning long short-term memory model to predict anticancer peptides using high-efficiency feature representation," *Molecular Therapy-Nucleic Acids*, vol. 17, pp. 1–9, 2019.

[178] R. S. Andersen, A. Peimankar, and S. Puthusserypady, "A deep learning approach

for real-time detection of atrial fibrillation," *Expert Systems with Applications*, vol. 115, pp. 465–473, 2019.

[179] F. A. Gers and J. Schmidhuber, "Recurrent nets that time and count," in *Proceedings of the IEEE-INNS-ENNS International Joint Conference on Neural Networks. IJCNN 2000. Neural Computing: New Challenges and Perspectives for the New Millennium*, vol. 3, 2000, pp. 189–194.

[180] M. Z. Uddin, "A wearable sensor-based activity prediction system to facilitate edge computing in smart healthcare system," *Journal of Parallel and Distributed Computing*, vol. 123, pp. 46–53, 2019.

[181] Q. Hou, J. Wang, R. Bai, S. Zhou, and Y. Gong, "Face alignment recurrent network," *Pattern Recognition*, vol. 74, pp. 448–458, 2018.

[182] Y. Yu, X. Si, C. Hu, and J. Zhang, "A review of recurrent neural networks: Lstm cells and network architectures," *Neural computation*, vol. 31, no. 7, pp. 1235–1270, 2019.

[183] S. Alhagry, A. A. Fahmy, and R. A. El-Khoribi, "Emotion recognition based on eeg using lstm recurrent neural network," *International Journal of Advanced Computer Science and Applications*, vol. 8, no. 10, 2017.

[184] A. Supratak, H. Dong, C. Wu, and Y. Guo, "Deepsleepnet: A model for automatic sleep stage scoring based on raw single-channel eeg," *IEEE Transactions on Neural Systems and Rehabilitation Engineering*, vol. 25, no. 11, pp. 1998–2008, 2017.

[185] T. Zhang, W. Zheng, Z. Cui, Y. Zong, and Y. Li, "Spatial–temporal recurrent neural network for emotion recognition," *IEEE transactions on cybernetics*, vol. 49, no. 3, pp. 839–847, 2018.

[186] V. Shah, M. Golmohammadi, S. Ziyabari, E. Von Weltin, I. Obeid, and J. Picone, "Optimizing channel selection for seizure detection," in *2017 IEEE signal processing in medicine and biology symposium (SPMB)*. IEEE, 2017, pp. 1–5.

[187] X. Zhang, L. Yao, Q. Z. Sheng, S. S. Kanhere, T. Gu, and D. Zhang, "Converting your thoughts to texts: Enabling brain typing via deep feature learning of eeg

signals," in *2018 IEEE international conference on pervasive computing and communications (PerCom)*. IEEE, 2018, pp. 1–10.

[188] X. Zhang, L. Yao, S. S. Kanhere, Y. Liu, T. Gu, and K. Chen, "Mindid: Person identification from brain waves through attention-based recurrent neural network," *Proceedings of the ACM on Interactive, Mobile, Wearable and Ubiquitous Technologies*, vol. 2, no. 3, pp. 1–23, 2018.

[189] J. A. Correa and I. Patras, "A multi-task cascaded network for prediction of affect, personality, mood and social context using eeg signals," in *2018 13th IEEE International Conference on Automatic Face & Gesture Recognition (FG 2018)*. IEEE, 2018, pp. 373–380.

[190] P. Sirpal, A. Kassab, P. Pouliot, D. K. Nguyen, and F. Lesage, "fnirs improves seizure detection in multimodal eeg-fnirs recordings," *Journal of Biomedical Optics*, vol. 24, no. 5, pp. 051 408–051 408, 2019.

[191] Q. Zhao, C. Li, J. Xu, and H. Jin, "Fnirs based brain-computer interface to determine whether motion task to achieve the ultimate goal," in *2019 IEEE 4th International Conference on Advanced Robotics and Mechatronics (ICARM)*. IEEE, 2019, pp. 136–140.

[192] L. Xu, Y. Liu, J. Yu, X. Li, X. Yu, H. Cheng, and J. Li, "Characterizing autism spectrum disorder by deep learning spontaneous brain activity from functional near-infrared spectroscopy," *Journal of neuroscience methods*, vol. 331, p. 108538, 2020.

[193] U. Asgher, K. Khalil, M. J. Khan, R. Ahmad, S. I. Butt, Y. Ayaz, N. Naseer, and S. Nazir, "Enhanced accuracy for multiclass mental workload detection using long short-term memory for brain–computer interface," *Frontiers in Neuroscience*, vol. 14, 2020.

[194] S.-H. Yoo, H. Santosa, C.-S. Kim, and K.-S. Hong, "Decoding multiple sound-categories in the auditory cortex by neural networks: an fnirs study," *Frontiers in Human Neuroscience*, vol. 15, p. 636191, 2021.

[195] R. Fernandez Rojas, J. Romero, J. Lopez-Aparicio, and K.-L. Ou, "Pain assessment based on fnirs using bidirectional lstms," *arXiv e-prints*, pp. arXiv–2012, 2020.

[196] A. F. Wolters, S. C. van de Weijer, A. F. Leentjens, A. A. Duits, H. I. Jacobs, and M. L. Kuijf, "Resting-state fmri in parkinson's disease patients with cognitive impairment: a meta-analysis," *Parkinsonism & related disorders*, vol. 62, pp. 16–27, 2019.

[197] H. C. Baggio and C. Junqué, "Functional mri in parkinson's disease cognitive impairment," *International review of neurobiology*, vol. 144, pp. 29–58, 2019.

[198] P. A. Bandettini, E. C. Wong, R. S. Hinks, R. S. Tikofsky, and J. S. Hyde, "Time course epi of human brain function during task activation," *Magnetic resonance in medicine*, vol. 25, no. 2, pp. 390–397, 1992.

[199] K. K. Kwong, J. W. Belliveau, D. A. Chesler, I. E. Goldberg, R. M. Weisskoff, B. P. Poncelet, D. N. Kennedy, B. E. Hoppel, M. S. Cohen, and R. Turner, "Dynamic magnetic resonance imaging of human brain activity during primary sensory stimulation." *Proceedings of the National Academy of Sciences*, vol. 89, no. 12, pp. 5675–5679, 1992.

[200] D. Attwell and C. Iadecola, "The neural basis of functional brain imaging signals," *Trends in neurosciences*, vol. 25, no. 12, pp. 621–625, 2002.

[201] G. M. Boynton, S. A. Engel, G. H. Glover, and D. J. Heeger, "Linear systems analysis of functional magnetic resonance imaging in human v1," *Journal of Neuroscience*, vol. 16, no. 13, pp. 4207–4221, 1996.

[202] N. K. Logothetis, "Neurovascular uncoupling: much ado about nothing," *Frontiers in neuroenergetics*, vol. 2, p. 1691, 2010.

[203] M. L. Schölvinck, A. Maier, F. Q. Ye, J. H. Duyn, and D. A. Leopold, "Neural basis of global resting-state fmri activity," *Proceedings of the National Academy of Sciences*, vol. 107, no. 22, pp. 10 238–10 243, 2010.

[204] H. Qian, "Medical image edge detection algorithm based on improved canny operator," *Software Guide*, vol. 18, no. 02, pp. 45–48, 2019.

[205] D. Karras and G. Mertzios, "New pde-based methods for image enhancement using

som and bayesian inference in various discretization schemes," *Measurement Science and Technology*, vol. 20, no. 10, p. 104012, 2009.

[206] P. M. Shankar, S. N. Gupta, and H. M. Gupta, "Applications of coherent optics and holography in biomedical engineering," *IEEE Transactions on Biomedical Engineering*, vol. BME-29, no. 1, pp. 8–15, 1982.

[207] Y. Cao, "Application of canny edge detection algorithm based on gaussian filter in medical images [j]," *Chinese Journal of Endemic Disease Control*, vol. 34, no. 05, pp. 54–55, 2019.

[208] Z. Xu, X. Ji, M. Wang, and X. Sun, "Edge detection algorithm of medical image based on canny operator," in *Journal of Physics: Conference Series*, vol. 1955, no. 1. IOP Publishing, 2021, p. 012080.

[209] M. D. Fox and M. E. Raichle, "Spontaneous fluctuations in brain activity observed with functional magnetic resonance imaging," *Nature reviews neuroscience*, vol. 8, no. 9, pp. 700–711, 2007.

[210] S. M. Smith, P. T. Fox, K. L. Miller, D. C. Glahn, P. M. Fox, C. E. Mackay, N. Filippini, K. E. Watkins, R. Toro, A. R. Laird *et al.*, "Correspondence of the brain's functional architecture during activation and rest," *Proceedings of the national academy of sciences*, vol. 106, no. 31, pp. 13 040–13 045, 2009.

[211] K. Smith, "fmri 2.0: functional magnetic resonance imaging is growing from showy adolescence into a workhorse of brain imaging," *Nature*, vol. 484, no. 7392, pp. 24–27, 2012.

[212] F. X. Castellanos and Y. Aoki, "Intrinsic functional connectivity in attention-deficit/hyperactivity disorder: a science in development," *Biological psychiatry: cognitive neuroscience and neuroimaging*, vol. 1, no. 3, pp. 253–261, 2016.

[213] F. X. Castellanos, D. S. Margulies, C. Kelly, L. Q. Uddin, M. Ghaffari, A. Kirsch, D. Shaw, Z. Shehzad, A. Di Martino, B. Biswal *et al.*, "Cingulate-precuneus interactions: a new locus of dysfunction in adult attention-deficit/hyperactivity disorder," *Biological psychiatry*, vol. 63, no. 3, pp. 332–337, 2008.

[214] L. Q. Uddin, A. C. Kelly, B. B. Biswal, D. S. Margulies, Z. Shehzad, D. Shaw, M. Ghaffari, J. Rotrosen, L. A. Adler, F. X. Castellanos *et al.*, "Network homogeneity reveals decreased integrity of default-mode network in adhd," *Journal of neuroscience methods*, vol. 169, no. 1, pp. 249–254, 2008.

[215] A. Aertsen, G. Gerstein, M. Habib, and G. Palm, "Dynamics of neuronal firing correlation: modulation of" effective connectivity"," *Journal of neurophysiology*, vol. 61, no. 5, pp. 900–917, 1989.

[216] J. E. Chen and G. H. Glover, "Functional magnetic resonance imaging methods," *Neuropsychology review*, vol. 25, pp. 289–313, 2015.

[217] C. Hohenfeld, C. J. Werner, and K. Reetz, "Resting-state connectivity in neurodegenerative disorders: Is there potential for an imaging biomarker?" *NeuroImage: Clinical*, vol. 18, pp. 849–870, 2018.

[218] S. Cocozza, G. Pontillo, C. Russo, C. V. Russo, T. Costabile, A. Pepe, E. Tedeschi, R. Lanzillo, V. Brescia Morra, A. Brunetti *et al.*, "Cerebellum and cognition in progressive ms patients: functional changes beyond atrophy?" *Journal of neurology*, vol. 265, pp. 2260–2266, 2018.

[219] B. Basile, M. Castelli, F. Monteleone, U. Nocentini, C. Caltagirone, D. Centonze, M. Cercignani, and M. Bozzali, "Functional connectivity changes within specific networks parallel the clinical evolution of multiple sclerosis," *Multiple Sclerosis Journal*, vol. 20, no. 8, pp. 1050–1057, 2014.

[220] S. D. Roosendaal, H. E. Hulst, H. Vrenken, H. E. Feenstra, J. A. Castelijns, P. J. Pouwels, F. Barkhof, and J. J. Geurts, "Structural and functional hippocampal changes in multiple sclerosis patients with intact memory function," *Radiology*, vol. 255, no. 2, pp. 595–604, 2010.

[221] G. A. Cecchi, A. R. Rao, M. V. Centeno, M. Baliki, A. V. Apkarian, and D. R. Chialvo, "Identifying directed links in large scale functional networks: application to brain fmri," *BMC Cell Biology*, vol. 8, no. 1, pp. 1–10, 2007.

[222] W. H. Lee and S. Frangou, "Linking functional connectivity and dynamic properties of resting-state networks," *Scientific reports*, vol. 7, no. 1, p. 16610, 2017.

[223] C. F. Beckmann and S. M. Smith, "Tensorial extensions of independent component analysis for multisubject fmri analysis," *Neuroimage*, vol. 25, no. 1, pp. 294–311, 2005.

[224] A. S. Lukic, M. N. Wernick, L. K. Hansen, J. Anderson, and S. C. Strother, "A spatially robust ica algorithm for multiple fmri data sets," in *Proceedings IEEE International Symposium on Biomedical Imaging*. IEEE, 2002, pp. 839–842.

[225] R. A. Harshman and M. E. Lundy, "Parafac: Parallel factor analysis," *Computational Statistics & Data Analysis*, vol. 18, no. 1, pp. 39–72, 1994.

[226] B. SJ, "Default-mode brain dysfunction in mental disorders: a systematic review," *Neurosci Biobehav Rev*, vol. 33, pp. 279–296, 2009.

[227] J. J. Bradstreet, S. Smith, M. Baral, and D. A. Rossignol, "Biomarker-guided interventions of clinically relevant conditions associated with autism spectrum disorders and attention deficit hyperactivity disorder," *Altern Med Rev*, vol. 15, no. 1, pp. 15–32, 2010.

[228] J. Posner, C. Park, and Z. Wang, "Connecting the dots: a review of resting connectivity mri studies in attention-deficit/hyperactivity disorder," *Neuropsychology review*, vol. 24, pp. 3–15, 2014.

[229] X. Cao, Q. Cao, X. Long, L. Sun, M. Sui, C. Zhu, X. Zuo, Y. Zang, and Y. Wang, "Abnormal resting-state functional connectivity patterns of the putamen in medication-naive children with attention deficit hyperactivity disorder," *Brain research*, vol. 1303, pp. 195–206, 2009.

[230] Y. Liu, H. Qu, X. Chang, K. Nguyen, J. Qu, L. Tian, J. T. Glessner, P. M. A. Sleiman, and H. H. Hakonarson, "Deep learning prediction of attention-deficit hyperactivity disorder in african americans by copy number variation," *Experimental Biology and Medicine*, vol. 246, pp. 2317 – 2323, 2021.

[231] K. Worsley, P. Jezzard, P. Matthews, and S. Smith, "Functional mri: an introduction to methods," 2001.

[232] M. P. van den Heuvel, C. J. Stam, M. Boersma, and H. H. Pol, "Small-world and scale-free organization of voxel-based resting-state functional connectivity in the human brain," *Neuroimage*, vol. 43, no. 3, pp. 528–539, 2008.

[233] M. Muehlhan, R. Miller, J. Strehle, M. N. Smolka, and N. Alexander, "Fkbp5 methylation predicts functional network architecture of the rostral anterior cingulate cortex," *Brain Structure and Function*, vol. 225, pp. 33–43, 2020.

[234] S. Whitfield-Gabrieli, S. Ghosh, A. Nieto-Castanon, Z. Saygin, O. Doehrmann, X. Chai, G. Reynolds, S. Hofmann, M. Pollack, and J. Gabrieli, "Brain connectomics predict response to treatment in social anxiety disorder," *Molecular psychiatry*, vol. 21, no. 5, pp. 680–685, 2016.

[235] C. Davatzikos, K. Ruparel, Y. Fan, D. Shen, M. Acharyya, J. W. Loughead, R. C. Gur, and D. D. Langleben, "Classifying spatial patterns of brain activity with machine learning methods: application to lie detection," *Neuroimage*, vol. 28, no. 3, pp. 663–668, 2005.

[236] M. B. Aberg and J. Wessberg, "An evolutionary approach to the identification of informative voxel clusters for brain state discrimination," *IEEE Journal of selected topics in signal processing*, vol. 2, no. 6, pp. 919–928, 2008.

[237] T. Nakao, J. Radua, K. Rubia, and D. Mataix-Cols, "Gray matter volume abnormalities in adhd: voxel-based meta-analysis exploring the effects of age and stimulant medication," *American Journal of Psychiatry*, vol. 168, no. 11, pp. 1154–1163, 2011.

[238] R. Beare, J. Chen, C. Adamson, T. Silk, D. Thompson, J. Yang, V. Anderson, M. Seal, and A. Wood, "Brain extraction using the watershed transform from markers," *Frontiers in neuroinformatics*, vol. 7, p. 32, 12 2013.

[239] R. H. B. Benedict, M. P. Amato, J. DeLuca, and J. J. G. Geurts, "Cognitive impairment in multiple sclerosis: clinical management, mri, and therapeutic avenues," *The Lancet. Neurology*, vol. 19, no. 10, pp. 860–871, 2020.

[240] A. Birenbaum and H. Greenspan, "Multi-view longitudinal cnn for multiple sclerosis lesion segmentation," *Engineering Applications of Artificial Intelligence*, vol. 65, no. C, pp. 111–118, 2017.

[241] P. Chhatbar and P. Kara, "Improved blood velocity measurements with a hybrid image filtering and iterative radon transform algorithm," *Frontiers in Neuroscience*, vol. 7, p. 106, 2013.

[242] H. Cho, G. Matthews, and O. Harel, "Confidence intervals for the area under the receiver operating characteristic curve in the presence of ignorable missing data," *International Statistical Review*, vol. 87, no. 1, pp. 152–177, 04 2018.

[243] F. Chollet, "Xception: Deep learning with depthwise separable convolutions," *CoRR*, vol. abs/1610.02357, 2016. [Online]. Available: http://arxiv.org/abs/1610.02357

[244] D. Oliva, E. Cuevas, G. Pajares, D. Zaldivar, and V. Osuna, "A multilevel thresholding algorithm using electromagnetism optimization," *Neurocomputing*, vol. 139, pp. 357–381, 2014.

[245] C. Rorden, T. Hanayik, D. R. Glen, R. Newman-Norlund, C. Drake, J. Fridriksson, and P. A. Taylor, "Improving 3d edge detection for visual inspection of mri coregistration and alignment," *Journal of Neuroscience Methods*, vol. 406, p. 110112, 2024.

[246] R. A. AS and S. Gopalan, "Comparative analysis of eight direction sobel edge detection algorithm for brain tumor mri images," *Procedia Computer Science*, vol. 201, pp. 487–494, 2022.

[247] S. Yunhong, Y. Shilei, Z. Xiaojing, and Y. Jinhua, "Edge detection algorithm of mri medical image based on artificial neural network," *Procedia Computer Science*, vol. 208, pp. 136–144, 2022.

[248] C. Shorten and T. Khoshgoftaar, "A survey on image data augmentation for deep learning," *Journal of Big Data*, vol. 6, no. 1, pp. 1–48, 2019.